2-P

THE EFFECT OF TEMPERATURE AND FIBER ORIENTATION ON THE STRENGTH AND DEFORMATION CHARACTERISTICS OF FIBER COMPOSITES

by

Fathi Aref Ibrahim Darwish

October, 1969

SU-DMS-70-T-7

Department of MATERIALS SCIENCE
STANFORD UNIVERSITY

THE EFFECT OF TEMPERATURE AND FIBER ORIENTATION ON THE STRENGTH AND DEFORMATION CHARACTERISTICS OF FIBER COMPOSITES

Fathi Aref Ibrahim Darwish

Stanford University

October 1969

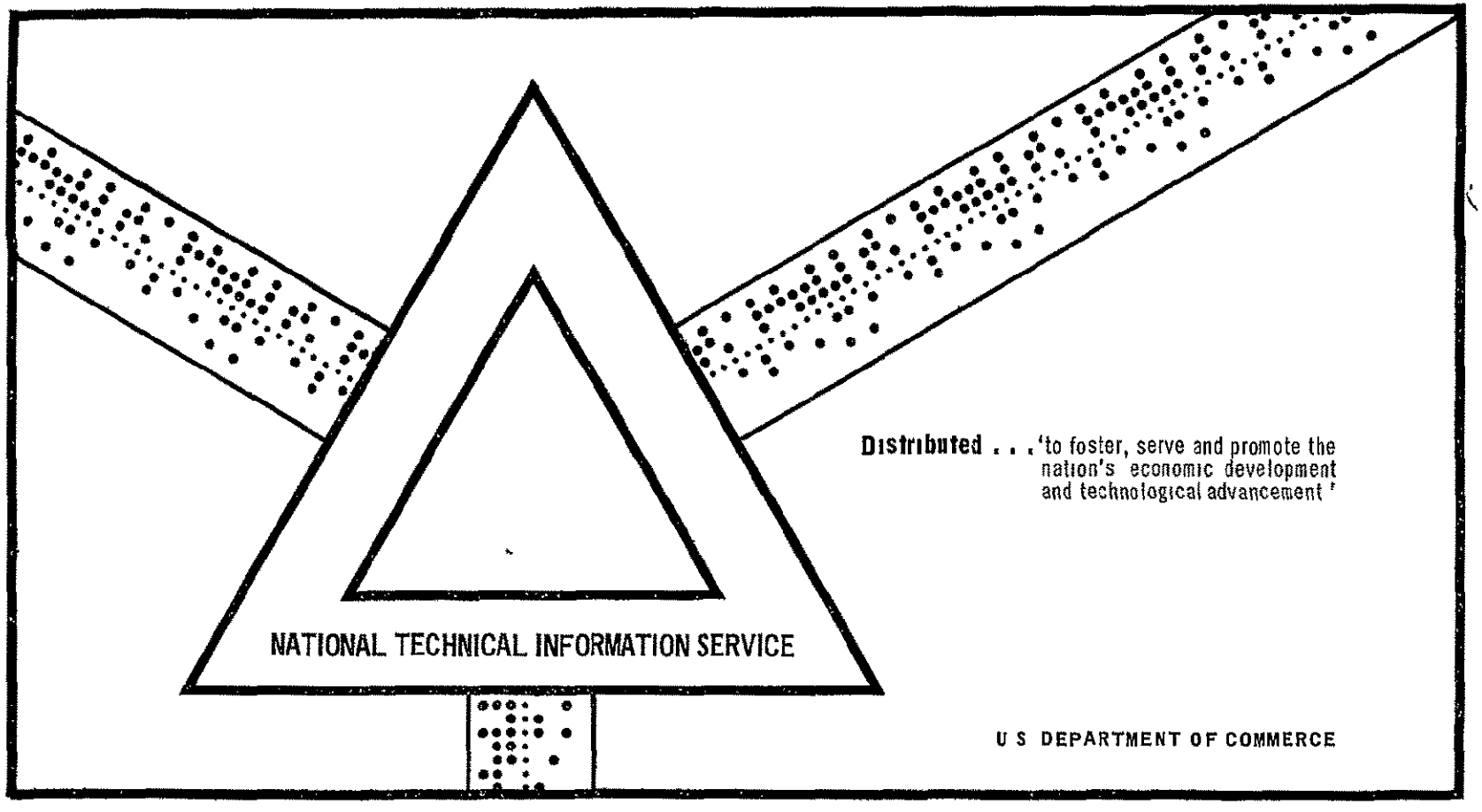

THE EFFECT OF TEMPERATURE AND FIBER ORIENTATION ON THE STRENGTH AND DEFORMATION CHARACTERISTICS OF FIBER COMPOSITES

by

Fathi Aref Ibrahim Darwish

Department of Materials Science

Stanford University

Stanford, California

October, 1969

Technical Report #8

Prepared for the

National Aeronautics and Space Administration

Under NASA Contract NSG-622

ABSTRACT

The effect of temperature and fiber orientation on the strength and deformation characteristics of the unidirectionally solidified Al-Al_3Ni eutectic alloy has been investigated by means of tension and slow-bend testing The tensile behavior of the composite in both the longitudinal (parallel to fiber axis) and transverse (perpendicular to fiber axis) direction has been evaluated in the temperature range -196°C→200°C It was found that a drop in temperature from 200°C down to -196°C causes the composite strength to increase by as much as 100%

Although the density of cracked fibers, when the composite is loaded parallel to fiber axis, is shown to increase under increasing applied stress, premature fiber failure does not lead to instability and the composite strength is primarily determined by the average fiber strength Taking plasticity of the matrix into account by linearizing its stress-strain curve, the longitudinal strength of the composite was predicted from the individual properties of its components

Dislocation etch-pitting studies of deformed Charpy-V specimens have revealed that the fiber orientation with respect to the specimen axis has a marked effect on the distribution of plastic deformation in the vicinity of the notch The development of the plastic zone on the surface of specimens having their fibers parallel to the notch leading edge was characterized by hinge formation, a behavior which is similar to that of a homogeneous material such as steel For the case where the fibers are parallel to the specimen axis, the extension of the plastic zone in the plane of the notch was found to be

limited as compared to the previous case However, the zone extended considerably in the lateral direction The important parameters which determine the extension of the zone were investigated

The plastic bend angle at the moment of fracture initiation was determined and correlated with the local plastic strains which were measured using microhardness values Root strain at failure was, therefore, determined as a function of temperature and then compared with the tensile ductility of the material with the fiber orientation in question The transverse strains, determined for specimens with different fiber orientations, clearly demonstrated the anisotropic plastic behavior of the composite and this had an effect on the mode of crack initiation

Criteria for crack initiation were introduced and discussed, and the impact energy values were related to the initiation and propagation energy terms.

ACKNOWLEDGMENTS

The author wishes to express his sincere appreciation and gratitude to·

Professor A S Tetelman, his thesis advisor, for his constant encouragement and invaluable guidance throughout the course of this study,

Professor J. C. Shyne and Professor O. D. Sherby, for their interest and time in reading the manuscript,

Dr T R Wilshaw, for his enlightening discussions which stimulated development of concepts necessary for this investigation,

Dr M. J. Salkind, with whom the author enjoyed occasional but very helpful discussions,

His conferrers in the Fracture Laboratory, especially Dr. D. O Harris, who performed the acoustic emission analysis at LRL, Livermore, and from whom the author has learned a great deal of various aspects in the field of fracture mechanics,

His friends Dr A Kamel and Mr. S. Athel, for their help in writing the computer programs necessary for performing the calculations involved in this investigation,

Grace Bartholomew, for typing the manuscript,

Mr. Perfecto Mary, for preparing the drawings,

The United Aircraft Research Laboratories, for supplying the material used in this study,

The National Aeronautics and Space Administration, for supporting this investigation under Contract NASA-NSG-622.

Special gratitude is reserved for his parents. It is their constant self sacrifice and priceless guidance that made his education possible.

The financial support of the Center for Materials Research at Stanford University is appreciated.

TABLE OF CONTENTS

TABLE OF CONTENTS

TABLE OF CONTENTS

LIST OF ILLUSTRATIONS

LIST OF ILLUSTRATIONS

LIST OF ILLUSTRATIONS

LIST OF ILLUSTRATIONS

LIST OF ILLUSTRATIONS

CHAPTER I

INTRODUCTION

Two phase composite materials may occur in one of three forms, continuous (interlocked) phases, a discontinuous phase embedded in a continuous matrix phase or two discontinuous phases Most materials of engineering importance belong in the second of these categories. This includes steels, dispersion strengthened alloys, cermets, concrete, most high temperature creep-resistant alloys and a number of special composites such as bonded fiberglass rocket cases.

The high modulus, hardness, yield strength and melting point and low chemical reactivity and density of many nonmetallic solids make them attractive for certain engineering applications However, a problem associated with using these materials in bulk form is that they possess minimal tensile ductility and failure almost invariably begins at a surface flaw or scratch.[1] One way of overcoming this serious problem is to disperse these strong brittle solids in a softer matrix material. The matrix would therefore protect the hard phase particles from surface damage and bind them together With adequate inter-particle spacing, cracks can not be transmitted through the matrix from one particle to its neighbor.

The idea behind a composite material is therefore one of putting together dissimilar materials to achieve a new material whose properties are different in scale and/or kind from any of its constituents. The goal is to take advantage of the superior properties of each component. For example with proper design and fabrication a composite superior in its toughness to any of its individual elements can be produced (e.g., fiber glass).

Two types of composite materials can be produced depending upon the shape of the hard phase particles Equiaxed second phase particles distributed in a softer matrix give rise to the structure known as an aggregate. When the hard phase is nonmetallic and the matrix is metallic, the aggregate is called a cermet On the other hand, if the second phase is aligned in the form of long thin fibers, the structure is known as a fiber composite. It is the second category that will be dealt with in this work.

In a fiber composite, the fibers could be continuous or discontinuous along their axis, but they are usually discontinuous in a plane normal to their axis (contiguous fibers would provide an easy path for crack propagation and hence lower the toughness of the material). The growing interest in fiber composites came as a result of several events.

(1) The successful development of glass fiber reinforced plastics in the early 1940's.[2]

(2) Discovery of the extraordinarily high strength properties of whiskers.[3,4] Herring and Galt showed that tiny filamentary particles could sustain stresses approaching-theoretical limits [3]

(3) In recent years, it has been demonstrated that fibers shorter than the gauge length of a specimen can reinforce a matrix in a similar manner to that of continuous fibers [5] Jech, Weber and Schwope[6] have shown that the properties of fiber reinforced composites are essentially the same for continuous and discontinuous fibers Formerly it was believed that fibers have to scan the whole length of the specimen if the matrix is to be reinforced. Manufacturing of long fibers is associated with many technical problems, since it is difficult to properly handle

long fibers without causing them to break to shorter lengths and without having them damaged through mechanical contacts

Composite materials possess properties that make them attractive for engineering applications. In general such properties can be summarized as follows.

(1) High strength to weight ratio

(2) High stiffness to weight ratio

(3) Strength retention at high service temperatures.

In conventionally processed materials near their melting point, the stress level in the plastic zone is so small that the fracture toughness G_{Ic} is low even though the fracture displacements are large [1]

$$G_{Ic} = 2\sigma V^*$$

where

σ = stress level in the plastic zone at the moment of failure

V^* = fracture displacement

In fiber composites, although temperature has an effect of lowering the stress levels, this effect does not become important until the melting point is almost reached (fibers, which carry the bulk of the applied load, generally retain a great deal of their strength even at temperatures close to the composite melting point), and consequently many fiber composites possess superior properties at elevated temperatures compared with conventionally processed materials To justify their relatively high cost, fiber composites would be most beneficially used in high temperature service applications At temperatures above 650°C a composite containing a 50 volume % sapphire whiskers is potentially much stronger than many super alloys [4]

(4) Another attractive application of fiber composites is the flexibility with which one can produce certain composites that are notch insensitive Fiber glass is an example of this Electroformed copper reinforced with tungsten wires[7] is another example Weak interfaces ahead of a notch or an advancing crack in such materials will debond under the effect of the transverse stress developed Following the methods of classical elasticity and assuming a state of plane stress, Cook and Gordon[8] found that the maximum value of the transverse stress, for an elliptical notch of prescribed root radius, occurred a little distance (about one root radius) ahead of the notch The most likely mode of failure would then be by splitting parallel to the fibers ahead of the notch, the notch subsequently would get blunted by running into the secondary crack

Because of these attractive properties, there has been a wide spread interest in applying these materials to aerospace projects and elsewhere

1 1 Limitations of Fiber Composites

From the viewpoint of practical composites, several problems are apparent

(1) The individual constituents of the composite must be chosen such that there is little or no solubility or other reaction between the matrix and the fiber, which should wet each other Chemical reactions between the matrix and the reinforcing phase results in a degradation of the reinforcing phase and therefore reduction in strength of the composite[9] Another form of fiber composite instability is characterized by spheroidization and/or agglomeration of the reinforcing phase. This results in little or no

change in the composite or amount of each phase present It does however result in morphological change which profoundly affects the strengthening mechanism [10]

(2) Manufacturing large supply of high strength fibers with favorable aspect ratios, proper handling of the fibers during fabrication to avoid damage, insuring suitable orientation and dispersion, and assuring full bonding between fibers and matrix are all steps that should be closely watched in the course of manufacturing a fiber composite Misconducting any of these processes could well lead to a defective composite.

(3) A drawback of fiber composites in fatigue is that the fiber-matrix interface represents a large amount of internal surface which may generate cracks, and any imperfections are emphasized during cyclic loading [11] However, incorporation of high modulus fibers into lower modulus metals can provide a significant improvement on the fatigue life of the matrix[11] provided that the composite exhibits well bonded low energy interfaces and superior microstructural perfection

1 2 Controlled Freezing of Eutectic Alloys

One method of manufacturing fiber composites is by artificially incorporating the whiskers (produced in different ways) into a suitable matrix using a suitable technique This method has the limitations discussed above

Another method for producing fiber composites is by the controlled solidification of eutectic alloys When one examines the literature on eutectic solidification, one is confronted by an almost endless variety of microstructures. However, some of the microstructures of different systems are basically similar A system outlined by Chadwick[12] provides a satisfactory categorization of the eutectic solidification

(1) Continuous microstructure

(2) Discontinuous microstructure where one of the phases of the alloy is dispersed in the other phase as discrete particles.

(3) Spiral structures, an example is the Mg-Zn eutectic alloy.

Fiber composites produced by controlled solidification of the eutectics belong to the first category. Careful regulation of the direction of heat flow during the solidification of the eutectic alloys could result in the growth of the second phase in a regular form such as rods or platelets aligned in a matrix of the other phase [13-16] This is accomplished by unidirectionally solidifying the eutectic melts A Planar liquid-solid interface is maintained and a thermal gradient is established in the liquid ahead of the advancing interface during the solidification process. The phases then grow perpendicular to the planar interface so that they are aligned throughout the ingot The ingot is withdrawn from the heat source (induction heating coil) either horizontally or vertically. However, the best results are obtained vertically because the effects of convention currents in the liquid are minimized [17]

The fact that the fibrous phase grown in a unidirectionally solidified eutectic is a true whisker and exhibits high strength was first demonstrated by Lemkey and Kraft.[18] Individual Cr whiskers extracted from the Cu-Cr eutectic alloy were mechanically tested and found to exhibit a linear stress-strain behavior to failure. The extracted whiskers were also shown to possess strength values as high as 1,000,000 p s i at room temperature

1 2-1 Advantages of Unidirectionally Solidified Composites

(1) No separate processes are needed for manufacturing of the fibers

(2) Handling problems of the fibers are eliminated thus avoiding damage to them especially those in the micron size range, which are sensitive to the smallest amount of mechanical contacts with one another and with instruments High strength fibers are produced, aligned parallel to the growth direction and well-bonded to the matrix all in one step

(3) The unit cells of each phase assume an orientation such that the interface between them is parallel to atomic planes of low index and nearly equal atomic density. The preferred crystallographic relationships which exhibit good epitaxy are present because of the low interfacial energy associated with close atomic matching [19] A good interfacial bond, therefore, exists between the fibers and matrix thus enhancing satisfactory transfer of the applied load and improving the fatigue behavior over that of a conventionally produced fiber composite

(4) Finally, such composites have excellent thermal stability [10,11]

1 2-2 Limitations of Unidirectionally Solidified Composites

(1) Volume fraction of the second phase is fixed by the eutectic composition Small deviations from the composition given by the eutectic are possible although very limited [20] However, this is compensated for by the very many eutectic reactions existing in nature

(2) The purity of the materials used must be high enough to retain a planar solid-liquid interface during solidification Impurities

in the materials will break down the planar interface to a cellular one

(3) Only most simple geometric shapes, such as rods or plates can be produced using the technique of unidirectional solidification

1 3 Mechanism of Fiber Reinforcement

There are many detailed reviews[21-23] of both the experimental and theoretical aspects of the problem of reinforcing matrices which are usually soft and ductile with fibers of much higher strength and rigidity This section will briefly deal with the principles, mechanisms and factors governing reinforcement Rather than reproducing a lengthy survey of the area, it is meant to summarize the theories pertinent to this work and to furnish a background on which further analysis and more detailed studies would be presented Ultimate tensile strength of a fiber composite is generally determined by the following factors·

(1) Stress-strain relationships of the individual elements of the composite

(2) Volume fraction of fibers V_f

(3) Service temperature

(4) Fiber morphology in particular the length to diameter ratio (aspect ratio L/d)

1 3-1 Case of Continuous Fibers

As the fibers are continuous (span the whole length of the specimen), the stress, when the specimen is loaded, will be constant over the entire length of the fiber The principal function of the matrix in

this case is to bind the fibers together. Assuming equality of strain in fibers and matrix and equating externally applied stress at composite failure σ_c to the stress carried by the individual constituents, we get

$$\sigma_c = V_f \sigma_{fb} + (1 - V_f) \sigma_m' \tag{1.1}$$

where

σ_{fb} = fiber breaking stress

σ_m' = stress borne by the matrix at fiber failure

In writing equation (1 1) it is assumed that fibers are all aligned parallel to the tensile axis and that all have the same strength

Usually most composites are made with a matrix that is soft and ductile with the result that almost invariably the yield stress of the matrix will be reached at or before failure. If the matrix rate of strain hardening is zero, the stress in the matrix at failure would be equal to its yield strength σ_m^y and the equation for the composite ultimate strength would therefore be

$$\sigma_c = V_f \sigma_{fb} + (1 - V_f) \sigma_m^y \tag{1.2}$$

If volume fraction of fibers is low, they will be highly stressed even at relatively moderate loading since they carry the bulk of the load When the weakest fiber breaks, the stress that was carried by it would be transferred to the remaining fibers and the weakest among them will break and so on. Eventually all fibers will break and only the matrix would be carrying the complete load The ultimate strength will thus be

$$\sigma_c = (1 - V_f) \sigma_m^u$$

where

σ_m^u = matrix ultimate strength.

A serrated stress-elongation curve was observed (Fig. 1 1) in a composite with 0 08 volume fraction of fibers [24] The peak denotes the position of fiber failure, the downward part being the transfer of load to the other fibers and the upward part being the recovery of the strength of the composite after redistribution [24] The critical volume fraction below which this happens, V_{crit}, is given by

$$V_{crit}\ \sigma_{fb} + (1 - V_{crit})\ \sigma_m^y = (1 - V_{crit})\ \sigma_m^u$$

Therefore,

$$V_{crit} = \frac{\Delta\sigma}{\sigma_{fb} + \Delta\sigma} \qquad (1\ 3)$$

where

$\Delta\sigma = \sigma_m^u - \sigma_m^y$ = strain hardening in matrix

In introducing fibers into the matrix the concept is to improve the strength of the matrix, giving the inequality

$$\sigma_c > \sigma_m^u .$$

The minimum value of V_f required to satisfy this inequality is given by

$$V_{min}\ \sigma_{fb} + (1 - V_{min})\ \sigma_m^y = \sigma_m^u$$

That is,

$$V_{min} = \frac{\Delta\sigma}{\sigma_{fb} - \sigma_m^y} \qquad (1\ 4)$$

Variation of the ultimate strength of a composite with the volume fraction of its brittle fibers is shown schematically in Fig. 1 2.

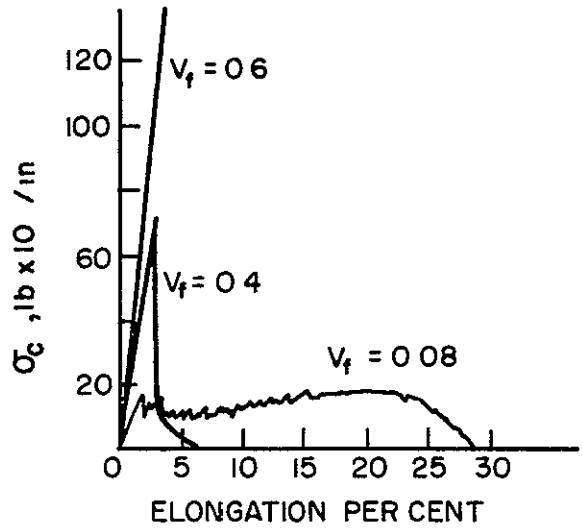

Figure 1 1 THE EFFECT OF FIBER VOLUME ON THE APPEARANCE OF THE COMPOSITE STRESS-STRAIN CURVE[24]

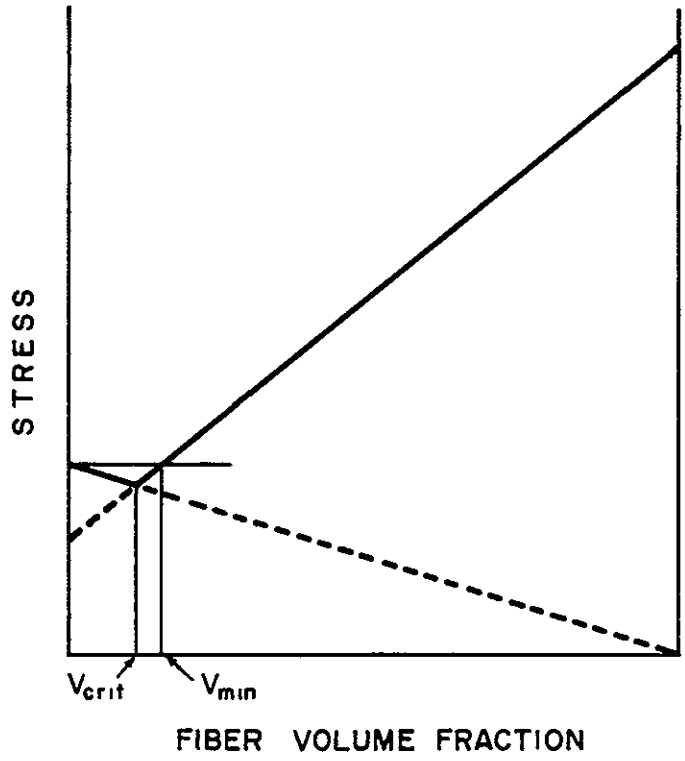

Figure 1 2 THE VARIATION OF THE ULTIMATE STRENGTH OF A COMPOSITE WITH THE VOLUME FRACTION OF ITS BRITTLE FIBERS

1 3-2 Case of Discontinuous Fibers

In order to evaluate the strength of a composite in which the fibers are discontinuous, the axial stress distribution in the fibers should be known The fibers do not span the specimen length and load is transferred to them by the matrix Difference in elastic moduli between the fibers and matrix would set up shear stresses along the interface when the composite is loaded These shear stresses are, in fact, the means by which the fibers are loaded.

The rule of mixtures assumes that each of the two constituents of a composite behaves as if the other is not present and hence the load supported by the composite at its failure would be equal to the load supported by the fibers added to the load carried by the matrix. Since, in the case of discontinuous fibers, the fiber stress σ_f is not constant all along the fiber length, σ_{fb} in equation (1 2) is replaced by the average stress carried by the fiber $\bar{\sigma}_{fb}$ This can be found only if the axial stress distribution in the fiber is known

Axial Stress Distribution in Discontinuous Fibers. Many theories have been introduced to find the stress distribution in discontinuous fibers embedded in a matrix Most of the theories treat the case of an elastic fiber in an elastic matrix. A common assumption to these theories is the existence of a perfect bond between the fiber and matrix

The first of these theories was introduced by Cox[25] in 1952 Assuming that the interfacial shear stress (between fiber and matrix) τ_J is proportional to the difference between the displacement in direction of the fiber a distance x from one end and the displacement of the matrix

at the same point if the fibers were absent, Cox obtained the following expression for the fiber stress σ_f corresponding to an applied stress σ.

$$\sigma_f = \frac{E_f - E_m}{E_m} \sigma \left[1 - \frac{\cosh \beta(L/2 - x)}{\cosh \beta L/2}\right] \qquad (1\ 5)$$

where

E = modulus of elasticity

f,m = subscripts implying fiber and matrix, respectively

L = fiber length

and β is a constant that is related to matrix shear modulus G_m, mean diameter of the fiber d, mean interfiber spacing and difference in elastic moduli of fiber and matrix

It is evident from equation (1.5) that the greatest strengthening occurs when the matrix has a lower modulus than the filament Plastic flow in the matrix, in effect, reduces E_m and therefore results in effective loading of the fibers

A simple and general relationship between the axial stress in fiber σ_f and the interfacial shear stress τ_j exists Considering the equilibrium of an element of the fiber dz in the axial direction z (Fig 1 3) one obtains

$$(\sigma_f + d\sigma_f) \frac{\pi d^2}{4} - \sigma_f \frac{\pi d^2}{4} = -(\pi d)\tau_j \, dz$$

That is,

$$\frac{d\sigma_f}{dx} = -\frac{d\sigma_f}{dz} = \frac{4\tau_j}{d} \quad . \qquad (1\ 6)$$

Equation (1 6) indicates that the gradient of the axial stress in fiber is proportional to the interfacial shear stress. τ_j (x) can thus be obtained by differentiating equation (1 5)

A second theory for predicting the stress distribution along a discontinuous fiber was introduced by Dow[26] in 1963 Two assumptions were made

(1) A perfect bond exists between the fiber and matrix

(2) Straight lines before deformation remain straight after deformation.

The interfacial shear stress τ_j predicted by the theory is given by

$$\tau_j = \frac{\lambda}{4}\left[\frac{P_{eff}\, E_f}{A_f\, E_f + A_m\, E_m}\right]\frac{\sinh \frac{\lambda z}{d}}{\cosh \frac{\lambda \ell}{d}} \tag{1.7}$$

where

$$\lambda = 2\left[\frac{2\sqrt{2}\left(\frac{G_f}{E_f}\right)\left[1 + \frac{A_f}{A_m}\left(\frac{E_f}{E_m}\right)\right]}{(\sqrt{2} - 1) + \left(\frac{G_f}{G_m}\right)\sqrt{\frac{A_m}{A_f} + 2 - \sqrt{2}}}\right]^{1/2} \tag{1.8}$$

$2\ell = L$ = fiber length

The load differential between fiber and matrix P_{eff} is given by

$$P_{eff} = P_m - P_f \frac{A_m\, E_m}{A_f\, E_f} \tag{1 9}$$

where

A = cross sectional area

P = applied load

G = shear modulus

f,m = subscripts implying fiber and matrix, respectively

An important point to be emphasized is that the preceding theories for predicting stress distributions neglect the effect of adhesion across the end face of the fiber.

The distribution of tensile and shear stresses along a fiber as predicted by the above theories is shown schematically in Fig 1.4. It is noted that the axial fiber stress has its lowest value at fiber end and rapidly increases to its maximum before it levels off On the other hand the shear stress τ_j is maximum at fiber end and decreases rapidly with x Shear stress concentration at fiber end was experimentally observed by a number of investigators.[27-29] Photoelastic studies performed by Schuster and Scala[27] on high strength αAl_2O_3 whiskers embedded in birefringent plastic as a matrix, indicated that matrix reinforcement occurred over a short distance from fiber end and that significant stress concentrations were created in regions immediately surrounding the fiber tips The stress distribution at whisker-matrix interface as obtained by Schuster and Scala together with that theoretically calculated from Dow's analysis are shown in Fig 1.5.

It is clear that for many composites the matrix shear stresses will exceed the elastic limit of the material τ_Y For this case (an elastic fiber in a plastic matrix), the shear stresses may be assumed constant and equal to τ_Y along the fiber-matrix interface. Equation (1.6) is then integrated simply to yield[1,30]

$$\sigma_f = \frac{4\,\tau_Y\,x}{d} \quad .$$

The minimum length a fiber should have for the stress σ_f to achieve a value equal to its breaking stress σ_{fb} at its center is given by

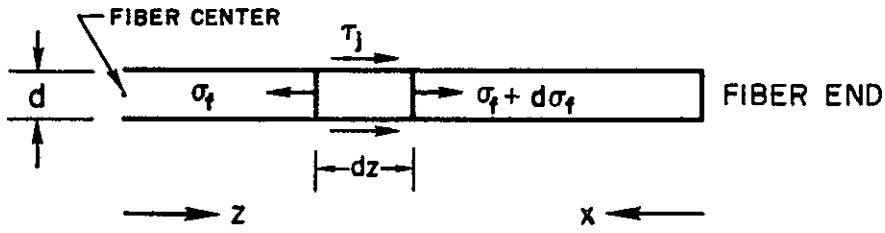

Figure 1.3 THE RELATIONSHIP BETWEEN AXIAL AND SHEAR STRESSES ALONG A FIBER

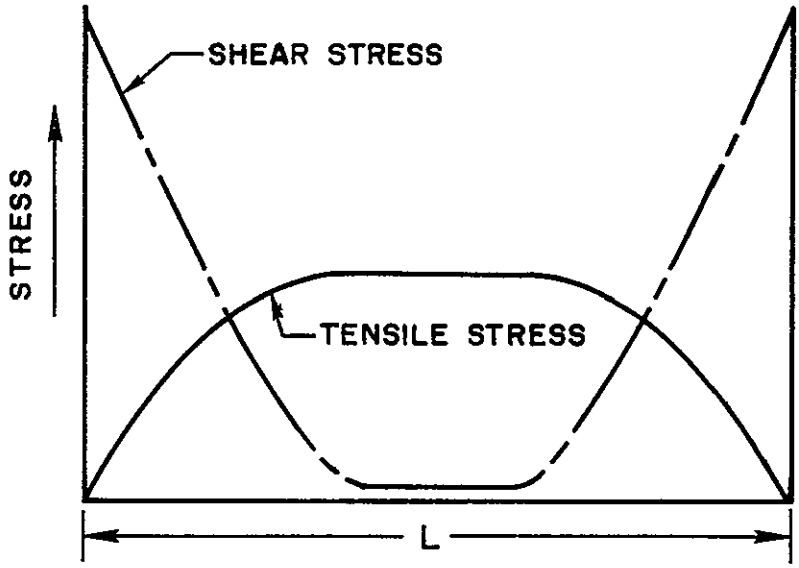

Figure 1.4 A SCHEMATIC DIAGRAM OF THE AXIAL AND SHEAR STRESS DISTRIBUTION ALONG A FIBER

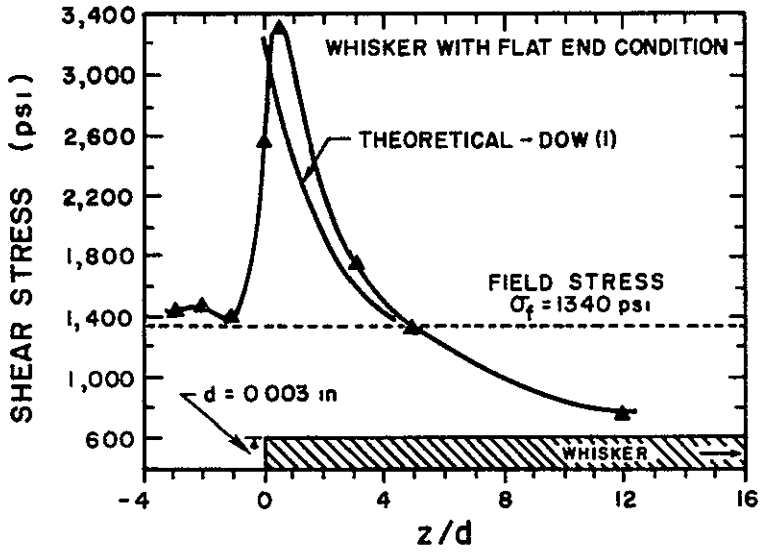

Figure 1 5 THE STRESS DISTRIBUTION AT WHISKER-MATRIX INTERFACE[27]

δ was evaluated as

$$\frac{\delta}{d} = \frac{1}{2}\left[\frac{(1 - V_f)^{1/2}}{V_f^{1/2}} \left(\frac{E_f}{G_m}\right)\right]^{1/2} \cosh^{-1}\left[\frac{1 + (1 - \phi)^2}{2(1 - \phi)}\right]$$

where

$2\ell = L$ = fiber length

ϕ = fiber efficiency.

If the fibers are assumed to have a strength distribution function of the Weibull[33] type

$$g(\sigma) = L\ \alpha\ \beta\ \sigma^{\beta-1}\ e^{-L\ \alpha\ \sigma^{\beta}}\ , \qquad (1.10)$$

the final expression for σ_c as given by Rosen[32] will be

$$\sigma_c = V_f\ (\alpha\ \delta\ \beta\ e)^{-1/\beta}$$

The constants α and β which characterize the distribution function $g(\sigma)$, can be evaluated by using experimental strength-length data for the particular fibers under consideration The mean fiber strength $\bar{\sigma}_{fb}$ is given by

$$\bar{\sigma}_{fb} = \int_0^{\infty} \sigma_f g(\sigma_f)\ d\sigma_f\ ,$$

and for $g(\sigma_f)$ given by equation (1.10), $\bar{\sigma}_{fb}$ is evaluated to be[32]

$$\bar{\sigma}_{fb} = (L\ \alpha)^{-1/\beta} \Gamma[1 + (1/\beta)] \qquad (1.11)$$

α and β can be defined, if the experimental $\bar{\sigma}_{fb}$ - L relationship is known.

$$\frac{L_c}{d} = \frac{\sigma_{fb}}{2\tau_Y}$$

where (L_c/d) is the critical plastic aspect ratio.

Fibers with length $L < L_c$ will not break, while those with $L > L_c$ will have a constant axial stress that is equal to σ_{fb} over a distance $(L-L_c)$ The average stress in the fiber at failure is thus calculated to be

$$\bar{\sigma}_{fb} = \sigma_{fb}\left[1 - \frac{L_c}{2L}\right]$$

and therefore,

$$\sigma_c = \sigma_{fb}\left[1 - \frac{L_c}{2L}\right]V_f + \sigma_m' (1-V_f) .$$

1.4 Statistical Approach to Evaluating Composite Strength

Fibers generally show a spread in strengths about the mean value. There can be a variation in strength due to differences in flaw structure Rosen[31,32] evaluated the strength of a composite in terms of the statistical strength characteristics of its fibers, fiber volume fraction and matrix properties Near a discontinuity (a fiber end or a fiber break) a part of the fiber is not fully loaded. This is the part of the fiber over which the load is transferred Using a shear lag type elastic analysis to find the axial stress distribution in the fiber, and defining the ineffective length δ by

$$\frac{\sigma_f(\ell-\delta)}{\sigma_f(o)\big|_{\ell\to\infty}} = \emptyset ,$$

1.5 Fracture Toughness

The toughness of a fiber composite depends on the fracture mode which in turn is determined by the relative strengths and ductilities of the fibers, matrix and interface between them A detailed account of fracture processes (fracture initiation and crack propagation) in fiber composites is found in Reference 34 For fiber composites containing brittle fibers in a tough matrix, two modes of crack propagation can occur depending on the interface properties.

1 5-1 Brittle Fibers, Strongly Bonded to a Tough Matrix

As the fibers ahead of an advancing crack front break, the remaining bridges of matrix neck down and fracture in a completely ductile manner. Since the work of fracture of brittle fibers is very small, toughness in the composite therefore results from the work done in drawing down the matrix material.

Experiments conducted by Cooper and Kelly[7] on tungsten reinforced copper indicated that most of the energy absorbed in fracturing the composite was used in deforming a relatively localized volume of matrix near the plane of the crack The distance x on either side of the fracture surface over which extensive plastic flow of the matrix occurs, is given by[7,34]

$$x = \frac{d(1 - V_f)}{V_f}$$

The work of fracture per unit area of the composite due to the plastic deformation of the matrix would then be

$$G_c \tilde{=} 2 \times V_m U \tilde{=} \frac{d(1 - V_f)^2}{V_f} \sigma_m^u \varepsilon_m^u$$

where

V_m = matrix volume fraction

U = work done per unit volume in deforming the matrix alone to its UTS

ε_m^u = matrix ultimate strain.

The volume of matrix involved in fracture ($2x\ V_m$) is in direct proportion to the diameter of the fibers, and therefore, for equal volume fractions, tougher composites are obtained with coarser fibers [7]

1.5-2 Composites Containing Weak Inteffaces or Weak Matrices

As previously mentioned, transverse tensile stresses and shear stresses at the advancing crack tip may be able to cause longitudinal splitting. This splitting action can blunt out the advancing crack (when the crack runs into the split) rendering the material essentially insensitive to the propagation of cracks in planes that are perpendicular to the fibers. Splitting is acceptable for composites that are loaded uniaxially, however low off axis loads could produce interface failure and thus nullify any advantages gained from improved longitudinal crack propagation resistance

In composites containing fibers of length $L < L_c$, fiber failure does not occur since the fiber is not long enough for the axial stress to build up to the fiber breaking stress σ_{fb} The composite fails in tension when the fibers are pulled out of the matrix If there is no work hardening in the matrix and the shear stress τ is maintained during

pull out, the work done in pulling N fibers of radius r out to an average distance $L_c/2$ perpendicular to the fracture plane is[34,35]

$$W = N \frac{\pi r \tau}{3} \left(\frac{L_c}{2} \right)^2$$

If N is the number of fibers intersecting a unit area of the fracture plane, then

$$V_f = N \pi r^2 ,$$

and therefore,

$$G_c = \frac{V_f \tau}{3r} \left(\frac{L_c}{2} \right)^2 = \frac{V_f}{24} \frac{d}{\tau} \sigma_{fb}^2$$

1 6 Plan of the Investigation

As mentioned earlier, the strength of a composite is determined by the stress-strain relationship of its individual constituents. Variation in temperature affects the properties of the composite elements and therefore the composite strength. Since the behavior of fiber composites is inherently anisotropic, one should take into account the orientation of the fibers in relation to the direction of loading

One of the purposes of this investigation was to study the composite tensile behavior in the longitudinal and transverse directions (parallel and normal to fiber axis, respectively) as a function of test temperature The material chosen for this purpose is the unidirectionally solidified Al-Al_3 Ni eutectic of the Al-Ni system. Volume fraction of the Al_3Ni fibers in the composite is about 10% which exceeds V_{min} as given by equation (1 4) A range of temperature from -196°C→200°C was selected for the study

Even in the presence of sharp cracks, the Al-Al_3Ni composite was found to fail beyond general yielding. A fracture mechanics approach for expressing K_c (critical stress intensity factor) is valid only when failure occurs below general yield, where the overall elongation is of an elastic order and therefore such an approach could not be taken for evaluating the toughness of the Al-Al_3Ni composite. A simple way, although not very accurate, of evaluating the toughness is by measuring the impact energy values. The impact behavior of V-notched charpy specimens of the Al-Al_3Ni composite was studied by Salkind and George[36] and it was shown to be quite anisotropic. Impact energy values were found to depend on the orientation of the fibers with respect to the loading axis and leading edge of the notch The energy absorbed in impact is related to the extent of slip in the matrix ahead of the notch and later ahead of the advancing crack as deformation proceeds

This investigation was also undertaken in order to study the effect of fiber orientation on the local deformation that occurs in the zone ahead of the notch in charpy specimens. Shape and size of plastic zones developed on the surface of charpy specimens loaded in slow bend were revealed by etch-pitting of dislocations and then correlated with the applied load. This was performed on specimens having their fibers oriented in different ways with respect to the specimen axis

The purpose of this work was also to evaluate the load carrying capacity of charpy bars with different fiber orientations and to study the fracture initiation in such bars as a function of test temperature.

CHAPTER II

MATERIAL AND EXPERIMENTAL PROCEDURES

2.1 Material

Experiments to study the effects mentioned in Chapter I were performed on the unidirectionally solidified Al-Al_3Ni eutectic of the Al-Ni system Composition of the alloy is depicted in Fig. 2.1

The "as-received" ingots* of the unidirectionally solidified material were 3 inches in diameter and 6 inches long. Ingot head and tail were discarded since fibers in them were found to be misaligned and unparallel to the growth direction.

Eutectic ingots having a nominal composition of 6 2% Ni were produced by melting zone refined aluminum and 99 99% Ni in recrystallized alumina crucibles in an argon atmosphere [11,16] The analyses of the starting materials are listed in Table 2.1. Remelting by induction heating and withdrawing the ingot vertically downward at a constant rate would cause solidification to proceed upward at a constant velocity Detailed description of the solidification method and procedure is found in References 11 and 16.

The ingots used in this work were produced at a solidification rate of 2 cm/hour The resulting micro structure consisted of rod like Al_3Ni whiskers embedded in a continuous aluminum matrix having about 0.045% Ni in solid solution

*These ingots were supplied by the United Aircraft Research Laboratories

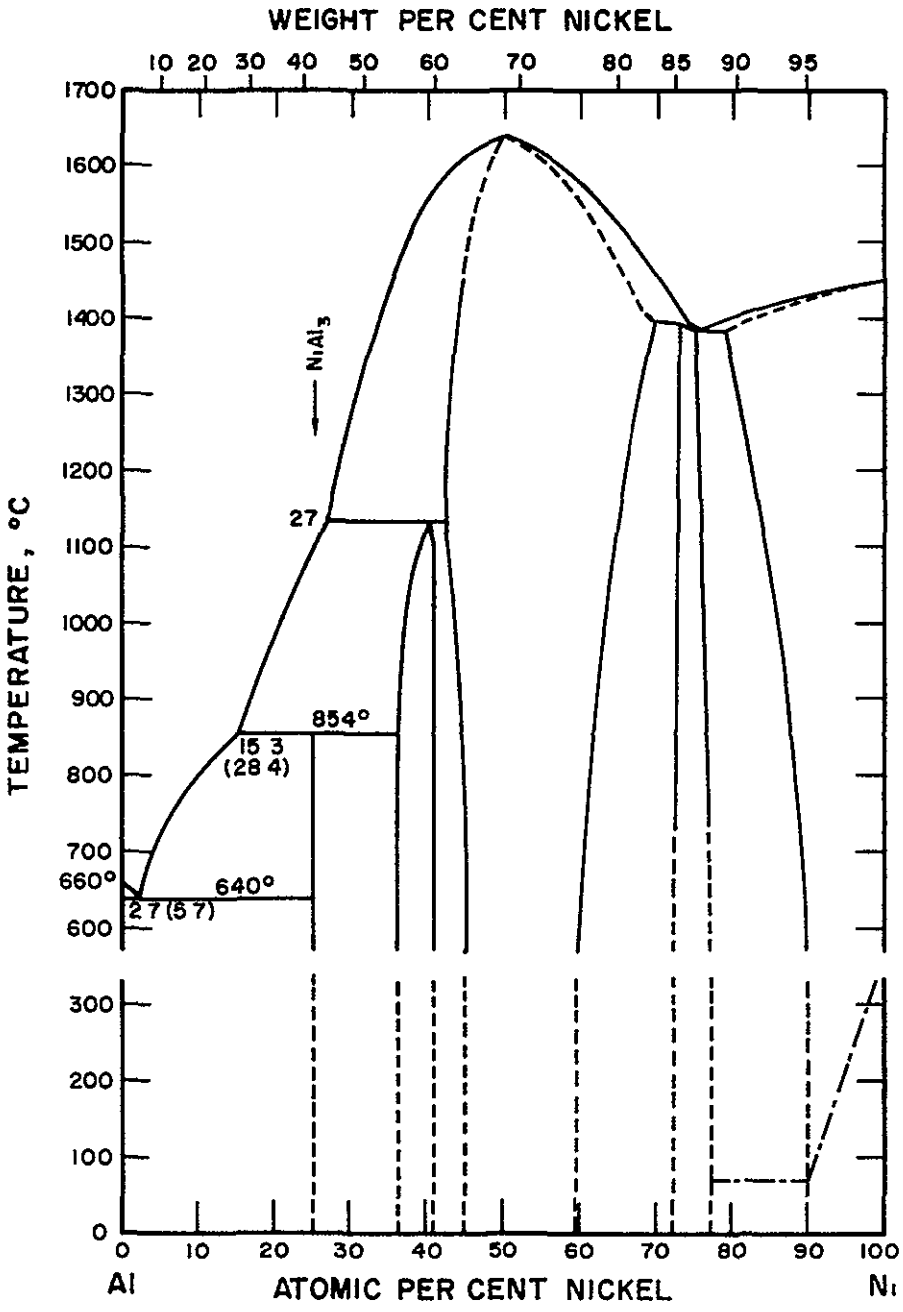

Figure 2 1 THE Al-Ni PHASE DIAGRAM(37)

TABLE 2 1

ANALYSES OF THE STARTING MATERIALS

	Impurity Concentrations in ppm							
	Si	Fe	Cu	Mn	Cr	Co	C	S
Aluminum	2	2 5	1.0	-	-	-	-	-
Nickel	7	2	<10	<10	4	10	40	10

The Al_3Ni phase shape, generally elliptical in cross section, approaches that of a circle at fast solidification rates. A micrograph taken for a cross section of an ingot solidified at 2 cm/hour is shown in Fig 2 2.

Fiber diameter d and interfiber spacing I were determined by averaging a large number of measurements made on micrographs taken for cross sections normal to fiber axis (growth direction) The interfiber spacing I has been taken as the shortest distance in matrix between a fiber and its nearest neighbor The values obtained were 1 425 and 2 microns for the diameter and interfiber spacing, respectively. Interfiber spacing taken as the distance from the center of a fiber to its nearest neighbor's center was determined as a function of the solidification rate by Lemkey, Hertzberg and Ford.[38] Fig 2 3 indicates that the interfiber spacing in ingots solidified at a rate of 2 cm/hour is 3 4 microns. This value is in excellent agreement with that obtained in this work which is (I+d) = 3 425 microns.

2 2 Specimen Preparation

The Charpy V notch specimen was selected for performing the slow bend tests. The specimen is the most widely used fracture test piece and as a result a good deal of information on its deformation is available A specimen is a rectangular prismatic bar, 10 mm x 10 mm x 55 mm with a 2 mm deep V notch in the center of one of the sides. The loading rollers are located in the three slots milled in the specimen as shown in Fig 2.4

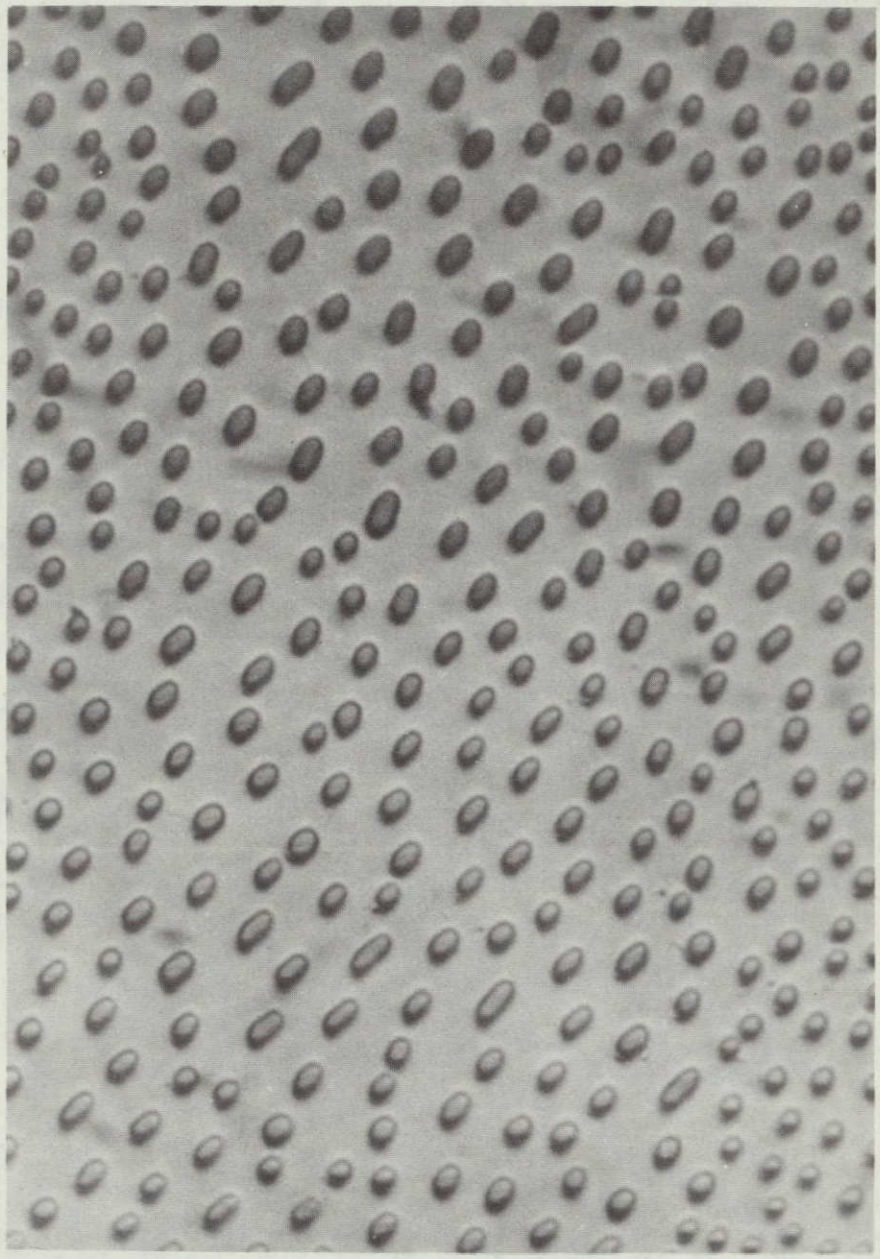

Figure 2.2 A CROSS SECTION THROUGH AN INGOT SOLIDIFIED AT A RATE OF 2 cm/hour, MAGNIFICATION = 2500X.

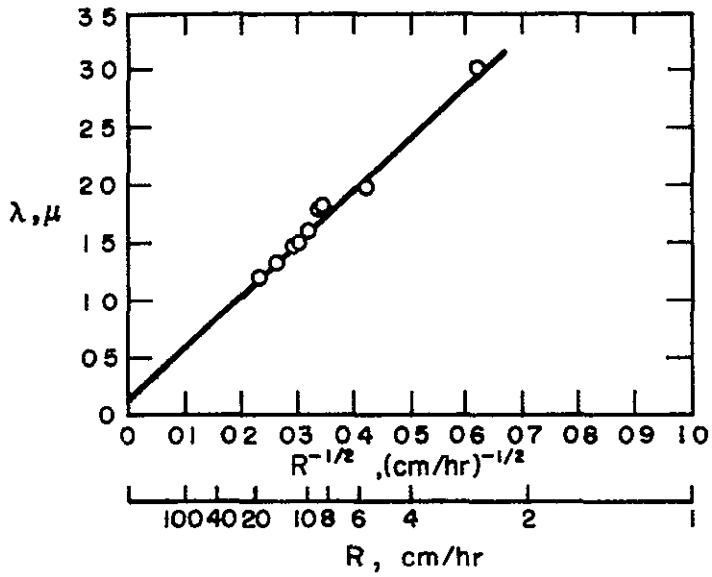

Figure 2 3 PLOT OF INTER-ROD SPACING, λ, VERSUS GROWTH RATE, R[38]

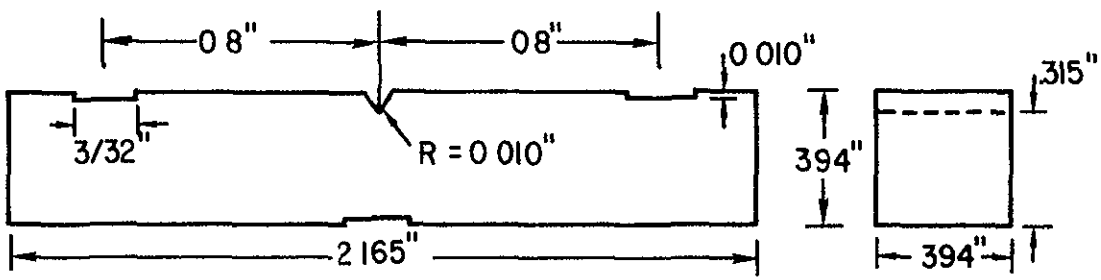

Figure 2.4 THE CHARPY V-NOTCH SPECIMEN

Sheet tensile specimens of the geometry and dimensions shown in Fig. 2 5 were prepared from 0.05" sheets which had been cut from the "as-received" ingot in a manner that would give the desired fiber orientation with respect to the tensile axis. The small holes in the ends of the specimen had very little load carrying capacity and were used rather to assure exact alignment of the specimen in the tensile grips

2.2-1 Specimen Orientation

Three specimen orientations were tested in an effort to study the effect of fiber orientation on the composite properties The specimen types, representative of fiber orientations of 0° and 90° are shown schematically in Fig 2.6. These configurations will be referred to as type A, E and F[36] throughout this work In type A tensile specimens the fibers are aligned parallel to the stress axis, and in type E and F they lie normal to the specimen axis but parallel to the width in one case (type E) and along the thickness in the other (type F). In type E charpy specimens, the fibers are normal to both the loading axis and the leading edge of the notch, whereas in type F they are normal to the stress axis but parallel to the notch leading edge.

In cutting specimens with the type A fiber orientations special care was taken to insure that the specimen axis was parallel to the growth direction (fiber axis). To obtain specimens with the type E and F orientations, the ingots were sliced into discs of thickness larger than 0 394", the specimens were cut and milled and then the notch was machined so as to give the required fiber orientation with respect to the leading edge of the notch

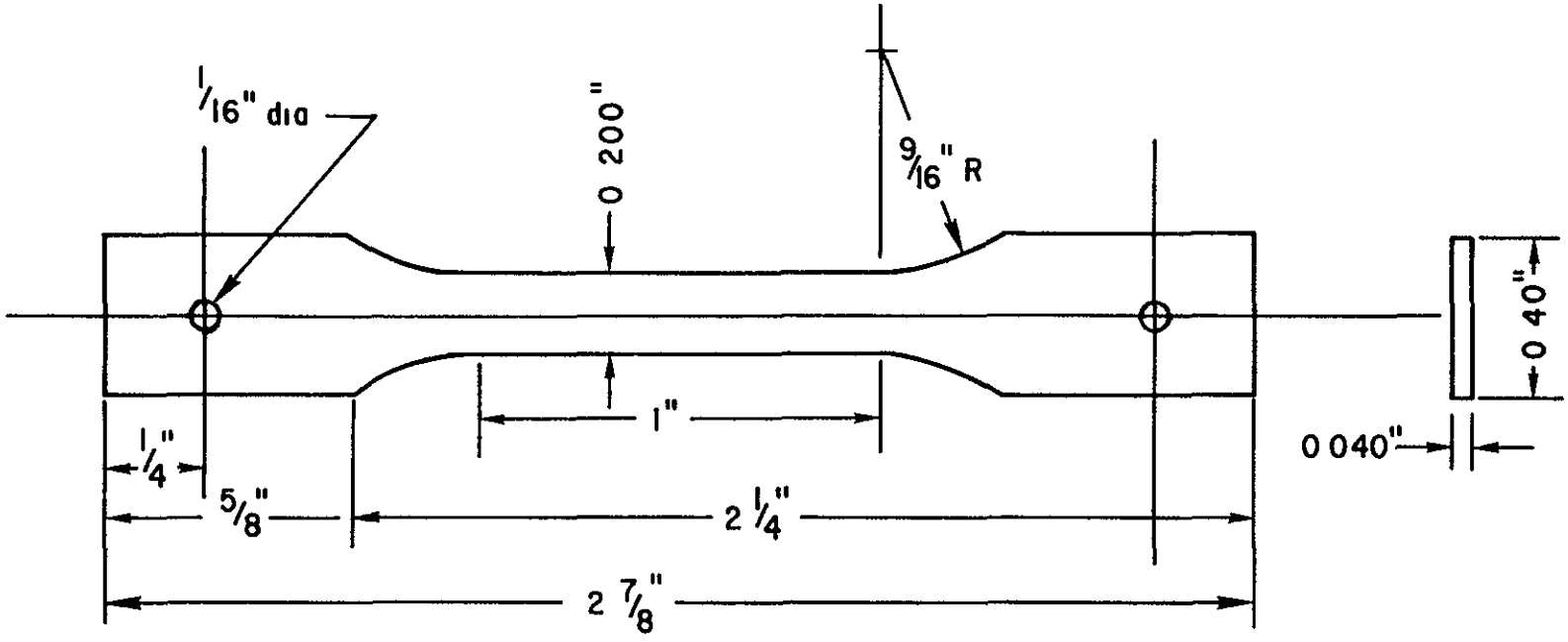

Figure 2.5 SHAPE AND DIMENSIONS OF TEST SPECIMENS

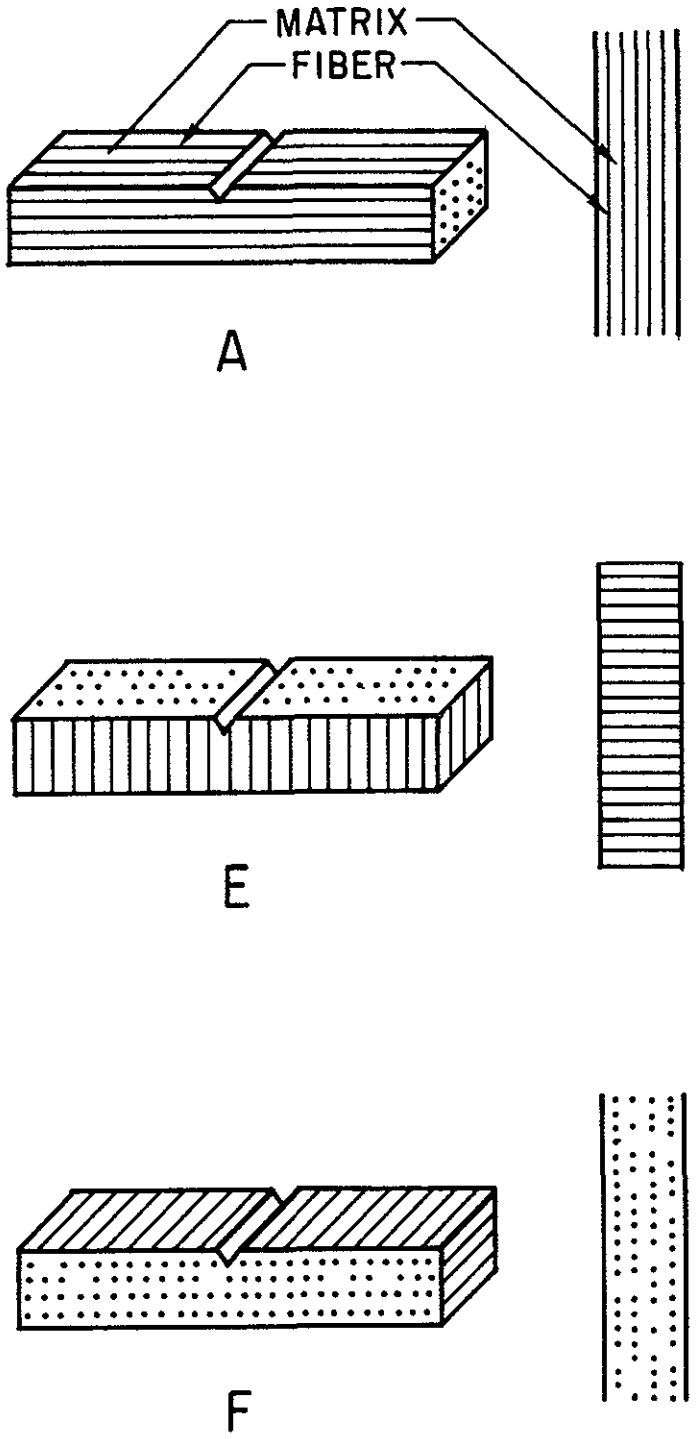

Figure 2 6 ORIENTATION OF CHARPY AND TENSILE SPECIMENS WITH RESPECT TO THE FIBER DIRECTION

The tensile specimens were prepared from slices about 0.05" in thickness. The slices were cut from the ingot either parallel or normal to the ingot axis according to the required orientation of the fibers in relation to the specimen axis The slices were cut into blanks larger than the final dimensions of the test specimen and then each of the surfaces was ground before the piece was finally milled to its final dimensions. Proper care was taken to insure that the centers of the two holes (Fig. 2 5) were on the center line of the specimen. After machining, the specimens were plished through a series of wet silicon carbide papers, this reduced the specimen thickness to about 0.04 inches. All specimens were given a light anneal at 120°C for one hour to remove any cold work and surface stresses

2 3 Mechanical Testing

Tension and slow bend tests were performed in order to study the effect of temperature on the (1) Strength and deformation, (2) Load carrying capacity and (3) Fracture initiation in specimens with various fiber orientations (A, E or F)

2.3-1 Tension Tests

Tests were performed on an Instron testing machine of 10,000 pound capacity A loading rate of 0 2"/min was used.

The grips that held the specimen were designed to apply a pure axial load for a specimen 0 04 inches thick To achieve that, the grip outer ends were provided with spherical bearings that fit into spherical seats attached to the ends of the pull rods By placing pins through the two holes in the specimen and through those in the grips, the

specimen was properly aligned. Flat pieces with sharp teeth machined on one side were placed one over each end of the specimen and fastened tightly to the grips with four bolts To maintain correct alignment, the assembly (specimen and grips) was clamped in a jig while tightening the bolts. No evidence of grip holder slippage was observed at the load levels used in this investigation

Required test temperatures were obtained by immersing the specimen and the entire tensile grips in appropriate liquid bath For obtaining test temperatures in the range -80°C → 25°C, alcohol cooled with liquid nitrogen was used. Isopentane in liquid nitrogen was employed for the -120°C → -80°C range Temperature was controlled and continuously recorded throughout the test on an x-y recorder of a Leeds and Northrup Speedomax controller-recorder, whose input was the voltage from a copper-constantan thermocouple immersed in the liquid bath kept under constant stirring

Test temperatures in the 25°C → 200°C range were obtained by using either a salt bath (for temperatures above 140°C) or Silicone oil. The oil or the salt was contained in a stainless steel container surrounded by the heating coil and separated from the outside container by an insulating material Two chromel-alumel thermocouples were used. One was connected to a temperature controller and the other to a potentiometer for measuring the bath temperature A stainless steel rod was used as a stirrer by connecting it to a motor operated by a variable input.

2.3-2 Slow Bend Tests

Slow bend tests were performed on an Instron testing machine at a cross head speed of 0.2 inches/mmn. The loading rollers were positioned by the slots in the specimen.

For test temperatures below -120°C, the copper-constantan thermocouple was taped to the specimen below the notch root and the specimen together with the entire bend jig were immersed in liquid nitrogen. The dewar that contained the liquid nitrogen was lowered to keep the specimen in the cold nitrogen vapors above the liquid. This allowed the specimen to warm up to the required temperature depending upon the position of the liquid surface with respect to the jig The liquid bath was moved up and down relative to the bend jig using an adjustable hand jack

2.4 Dislocation Etch-Pitting

Deformation patterns on the surface of deformed Charpy specimens were revealed by etch-pitting the dislocations in the plastically deformed zones. A number of etchants for revealing dislocations in Al have been reported [39-41] These etchants depend on the decoration of the dislocations by impurity atoms. Montgomery and Craig[42] developed a technique for revealing dislocations in zone refined aluminum The etchant used does not depend for its action on decorating the dislocations by impurity atoms but rather the dislocations themselves are responsible for the etch pits The technique would therefore have the advantage of revealing fresh glide dislocations as well as screw dislocations. In addition, the technique is insensitive to the orientation of the specimen

surface and therefore reveals dislocations on all glide systems. A deformed region, in the neighborhood of the notch in a deformed type F charpy specimen, as revealed using the technique is shown in Fig. 2 7. The dislocation etch pits are shown at higher magnifications in Fig. 2.8.

Specimens were first hand polished, mechanically polished to a 6 micron diamond finish and then polished for 3 minutes in a chemical polishing solution which had the following composition

60% H_2SO_4, 30% H_3PO_4 and 10% HNO_3

The solution was held at 100°C during the polishing process The specimens were then washed under the tap, rinsed in alcohol, dried in a stream of hot air and then coated with a thin oxide layer by annealing in air at 450°C for one hour and cooling in furnace After deforming the specimens, dislocation etch pits were developed by immersing the specimens in the same polishing solution and holding its temperature at 50°C Formation of hydrogen bubbles indicates that etching has occurred. Montgomery and Craig pointed out that contact of the etching solution with iron would ruinously contaminate the reagent.

It is believed that the etching mechanism is one of preferential attack of the specimen surface by the acid reagent As the specimen is deformed, the oxide layer formed on the surface during annealing breaks down at points where the dislocations intersect the specimen surface (in regions of plastic deformation) A thinner oxide film reforms and therefore penetration of the oxide by the acid in these locations will be faster thus developing the etch pits. It was suggested by Shockley[43] that the high stresses developed in the oxide layer at positions where dislocations intersect the surface are released by diffusion of the oxide film over the aluminum surface thus giving rise to preferential attack by the acid reagent.

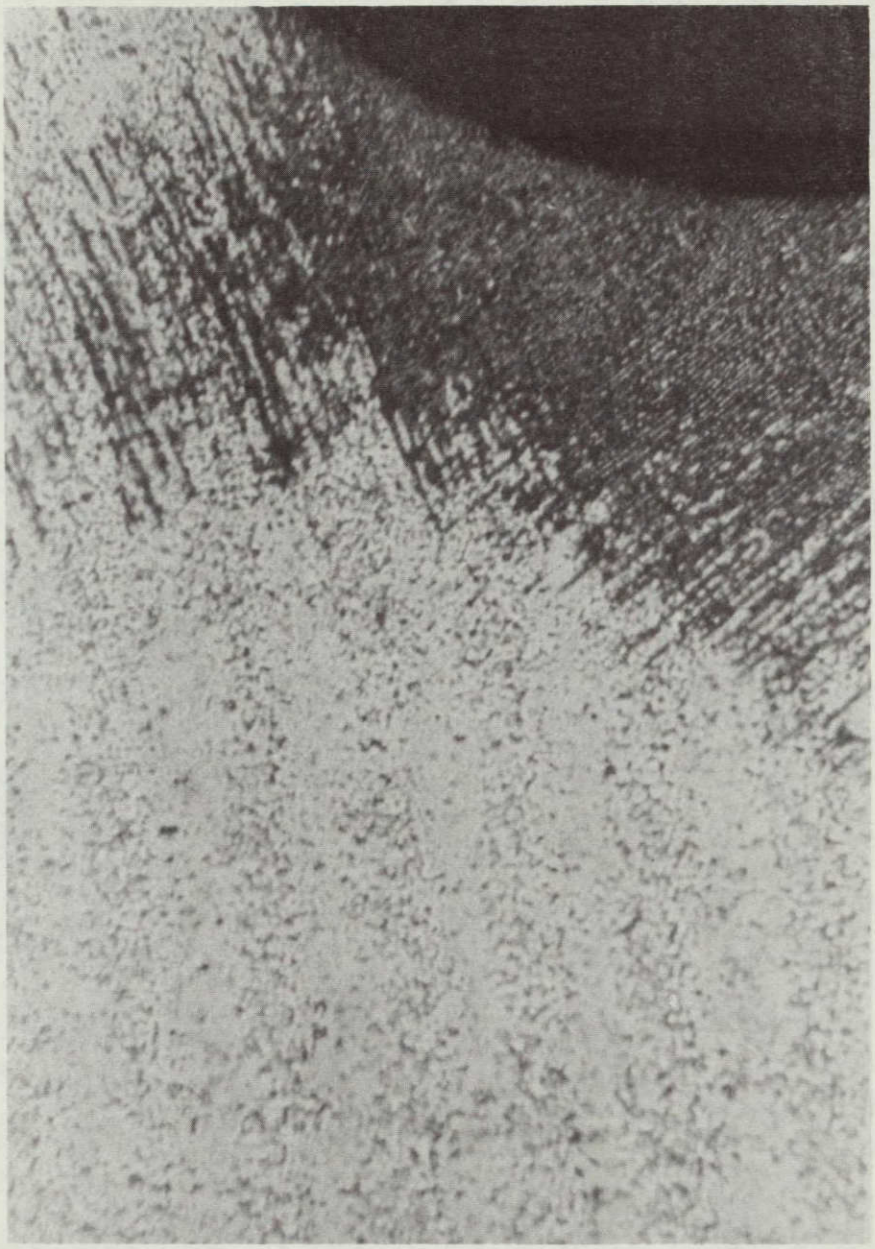

Figure 2.7 A DEFORMED REGION AHEAD OF THE NOTCH IN A TYPE F CHARPY SPECIMEN LOADED TO P = 160 lb., AS REVEALED USING THE ETCHING TECHNIQUE, MAGNIFICATION = 320X.

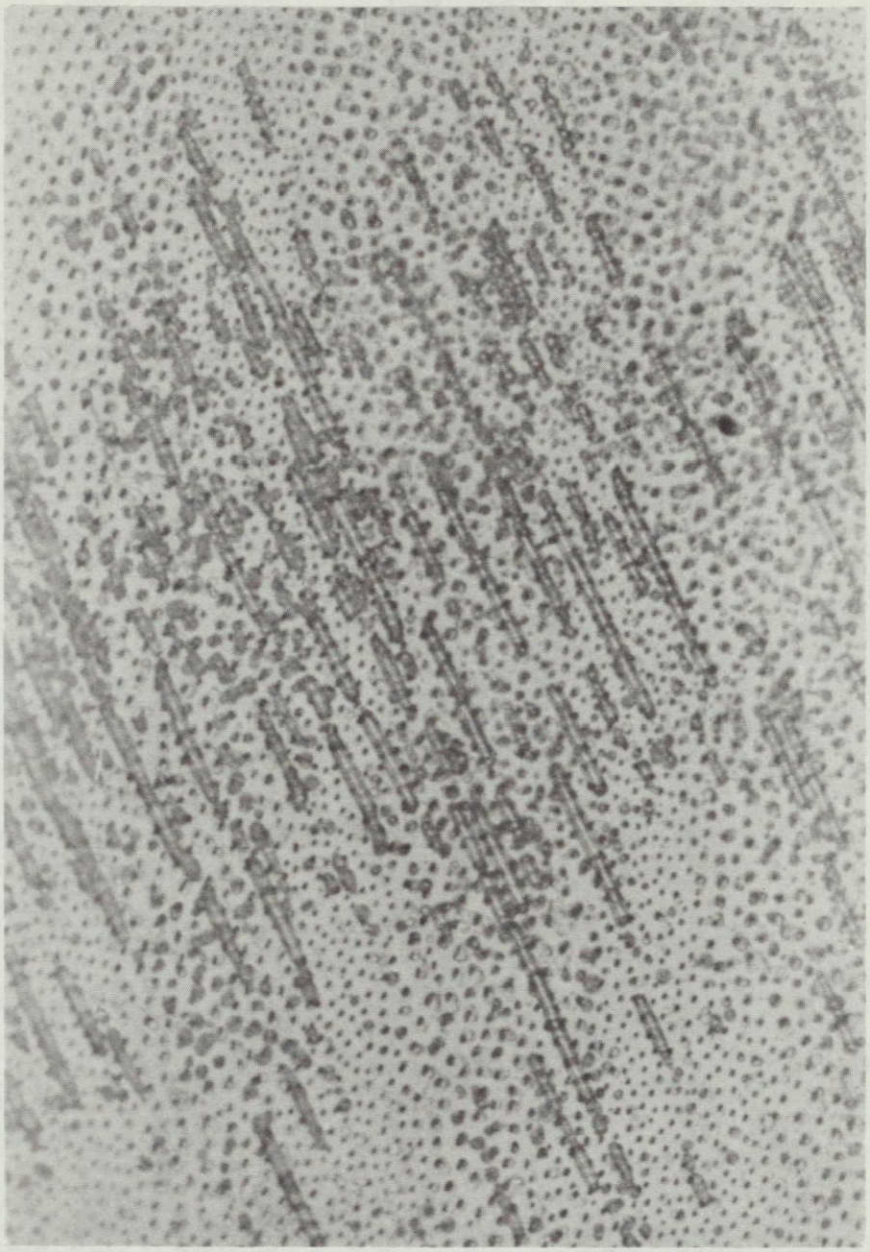

Figure 2.8 DISLOCATION ETCH-PITS IN THE PLASTIC ZONE OF A DEFORMED TYPE F CHARPY SPECIMEN, MAGNIFICATION = 800X.

2.5 Metallography

After mechanically polishing the specimens to a 6 micron diamond finish, they were electropolished in a solution of 60 cc perchloric acid, 590 cc methanol, and 350 cc ethylen glycol monobutyl ether.[10] The solution was contained in a 3-1/2 inch diameter glass beaker which was immersed in an icewater bath to keep the electrolyte at a temperature below 20°C while polishing. The electrolyte was constantly stirred. The cathode was a flat rectangular piece of aluminum and the specimen was made the anode. Electropolishing was performed for about 1-1/2 minutes at a voltage of 20 volts. With the arrangement described, this voltage resulted in a current density of about 1 ampere per square centimeter. This depended largely on the area of the specimen immersed in the electrolyte and on the distance between the two electrodes.

Photomicrographs were taken with a Leitz microscope equipped with 35 mm camera. Some micrographs were taken using a polaroid camera fixed to the microscope. Low magnification photographs were obtained by fixing low magnification lenz to the microscope and using the polaroid camera.

CHAPTER III

THE EFFECT OF TEMPERATURE AND FIBER ORIENTATION ON THE TENSILE PROPERTIES OF THE COMPOSITE

In order to study the composite tensile behavior and its dependence on the orientation of its fibers with respect to the stress axis, sheet tensile specimens of the shape and dimensions shown in Fig. 2.5 were loaded to failure at various test temperatures in the range $-196^{o}C \rightarrow 200^{o}C$. The three fiber orientations adopted for the study are shown in Fig. 2.6. Stress-strain curves were obtained, and ultimate tensile strength and elongation were measured.

Variation in the composite behavior with temperature is due to changes in the properties of its individual constituents. Tensile tests were therefore also performed on a plain matrix material that was unidirectionally solidifed in the same way as was the composite. The composite properties could thus be predicted in terms of the fiber and matrix properties at the various test temperatures.

3.1 Stress-Strain Curves

Stress-strain curves of the composite in the longitudinal (parallel to the fiber axis) and transverse (normal to the fiber axis) directions are shown in Figures 3.1a, 3.1b and 3.1c. Since elongations obtained when the composite is loaded parallel to the fiber axis do not exceed 3.5%, the stresses were computed by dividing the applied load by the cross sectional area of the specimen. The deflection of the cross-head of the testing machine includes the elastic deformation of the machine components such as pull rods and grips which does not permit

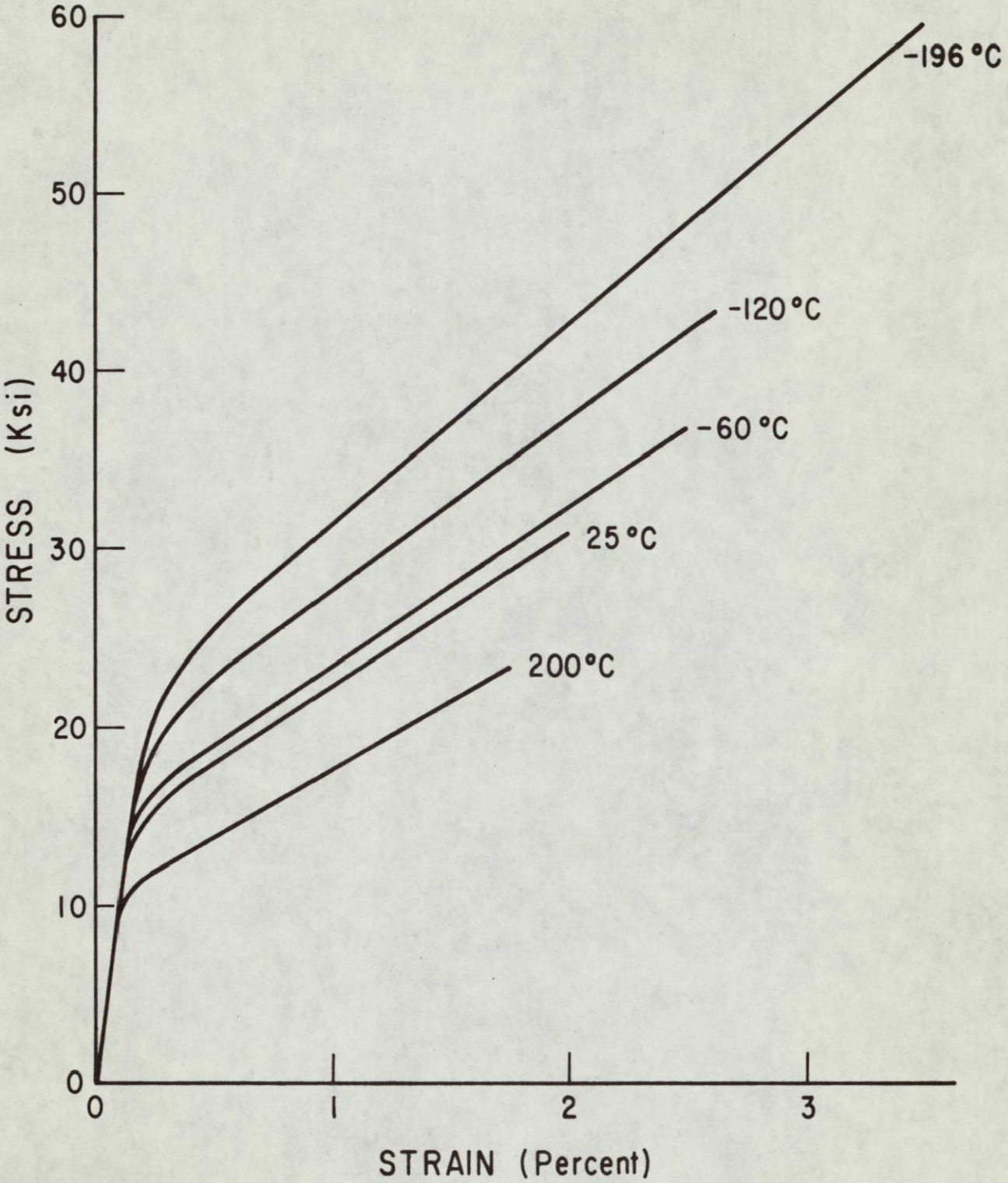

Figure 3.1a THE EFFECT OF TEMPERATURE ON THE STRESS-STRAIN CURVE OF TYPE A SPECIMENS

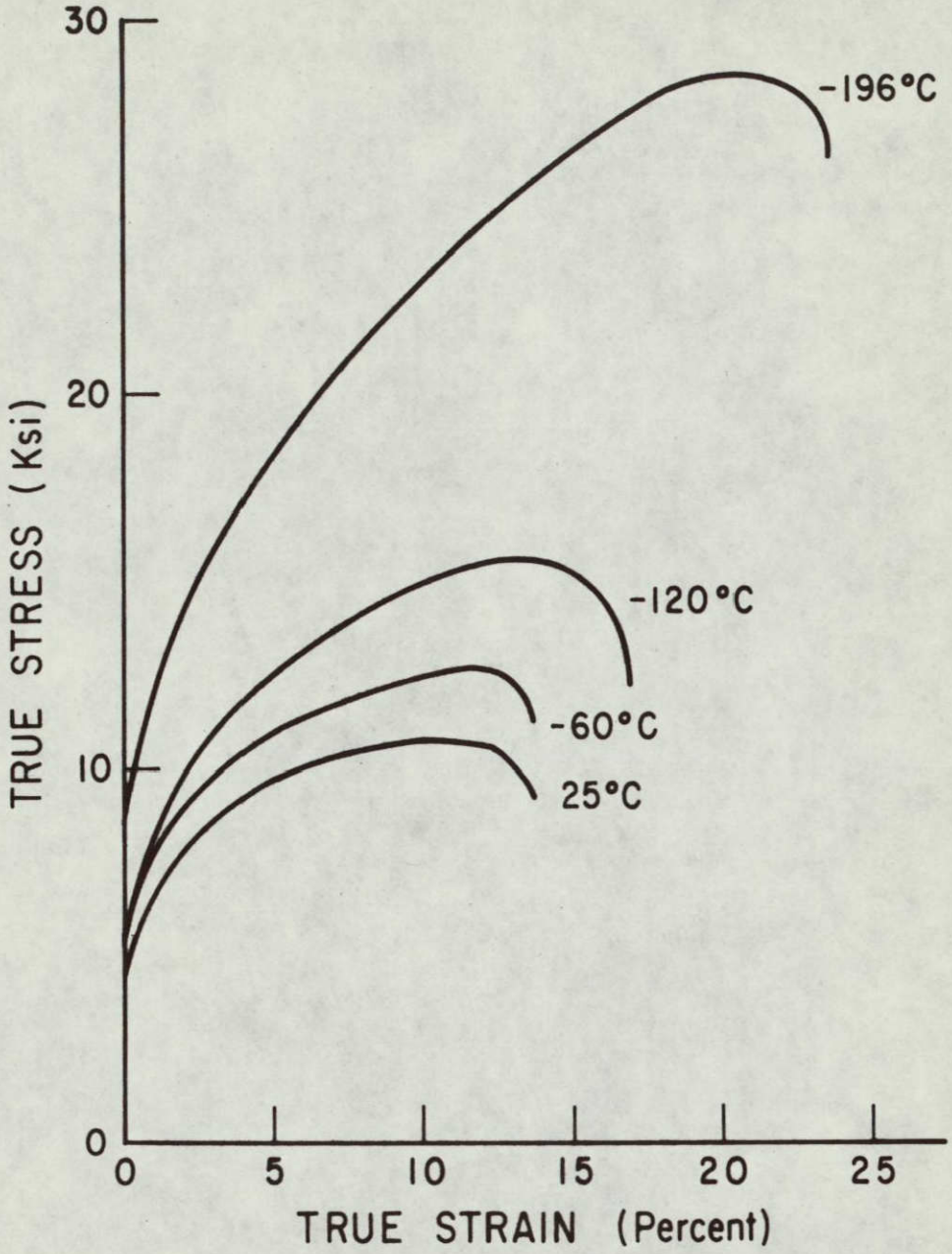

Figure 3.1b THE EFFECT OF TEMPERATURE ON THE STRESS STRAIN CURVE OF TYPE E SPECIMENS

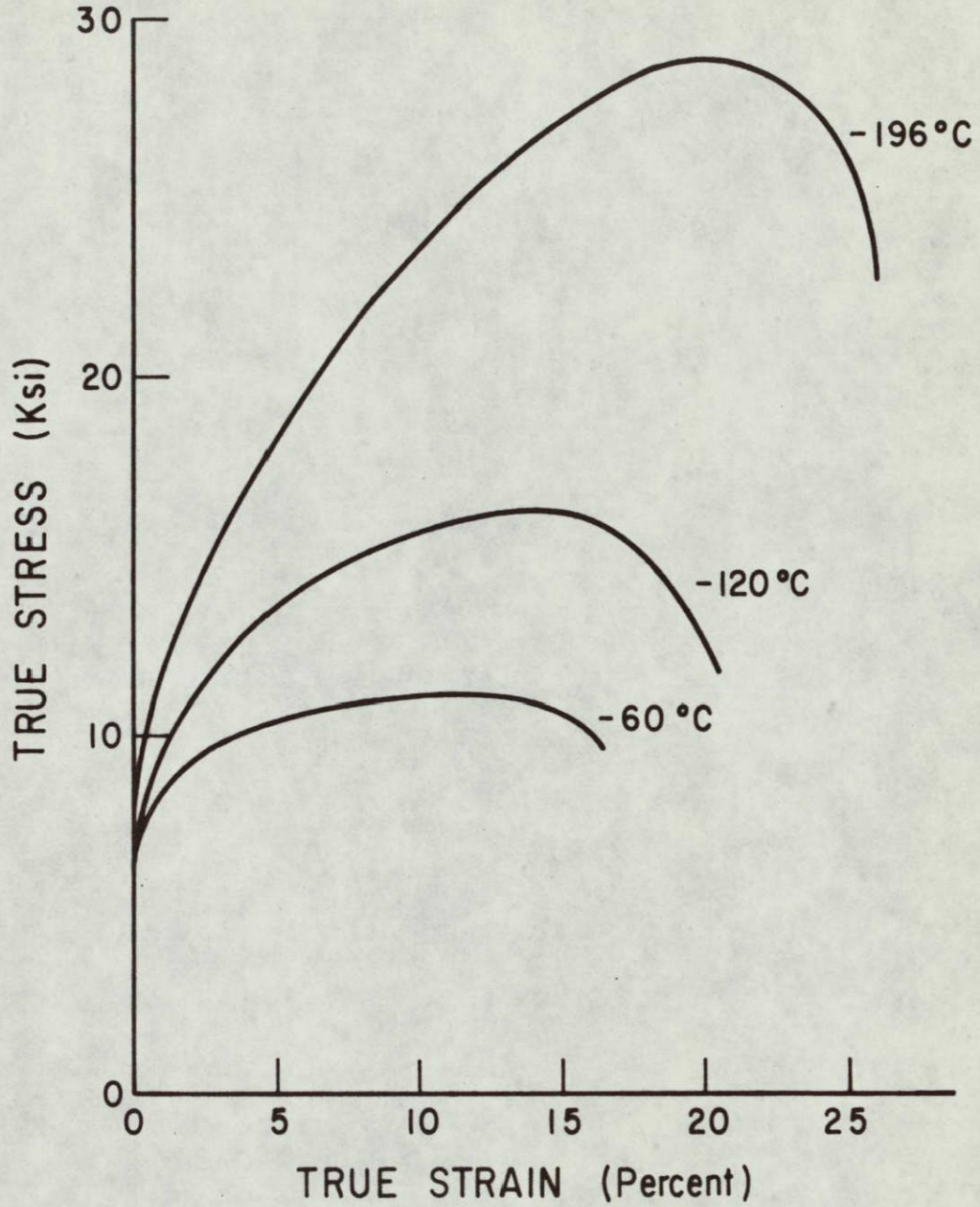

Figure 3.1c THE EFFECT OF TEMPERATURE ON THE STRESS-STRAIN CURVE OF TYPE F SPECIMENS

direct conversion to strain in the specimen. The strain, therefore, was measured using a strain gage and was correlated with the crosshead deflection which was automatically recorded on a strip chart. Because of the large amount of elongation that the material undergoes when loaded in a direction normal to the fibers, the curves shown for the composite in the transverse direction were taken from the cross-head motion of the Instron tensile machine. The cross-head movement recorded on the strip chart provides a sufficiently accurate basis for computing strains in specimens loaded in a direction parallel to fiber axis.

Stress-strain curves of the matrix material were obtained by tensile testing of specimens having geometry and dimensions identical to those of the composite tensile specimens (Fig. 2.5).

Temperature has a large effect on the strain hardening rate of FCC metals. The stress-strain curves shown in Fig. 3.2 are appreciably steeper at low temperatures. At -196°C strain hardening is effective enough to raise the true fracture stress of the matrix from a value of 8,200 p.s.i. at room temperature up to 24,600 p.s.i. On the other hand, at temperatures high enough for thermal recovery to occur during straining, the effective rate of work hardening is much reduced as demonstrated by the curve obtained by testing the material at 200°C. The curves shown in Fig. 3.2 also indicate that the temperature variation of the matrix yield stress is not very great.

3.2 Tensile Behavior of the Specimens Oriented Parallel to the Fiber Axis

The composite exhibits a change in the slope of its stress-strain curve. Prior to the change in the slope, the fibers and the matrix behave elastically since the initial strain is elastic for the

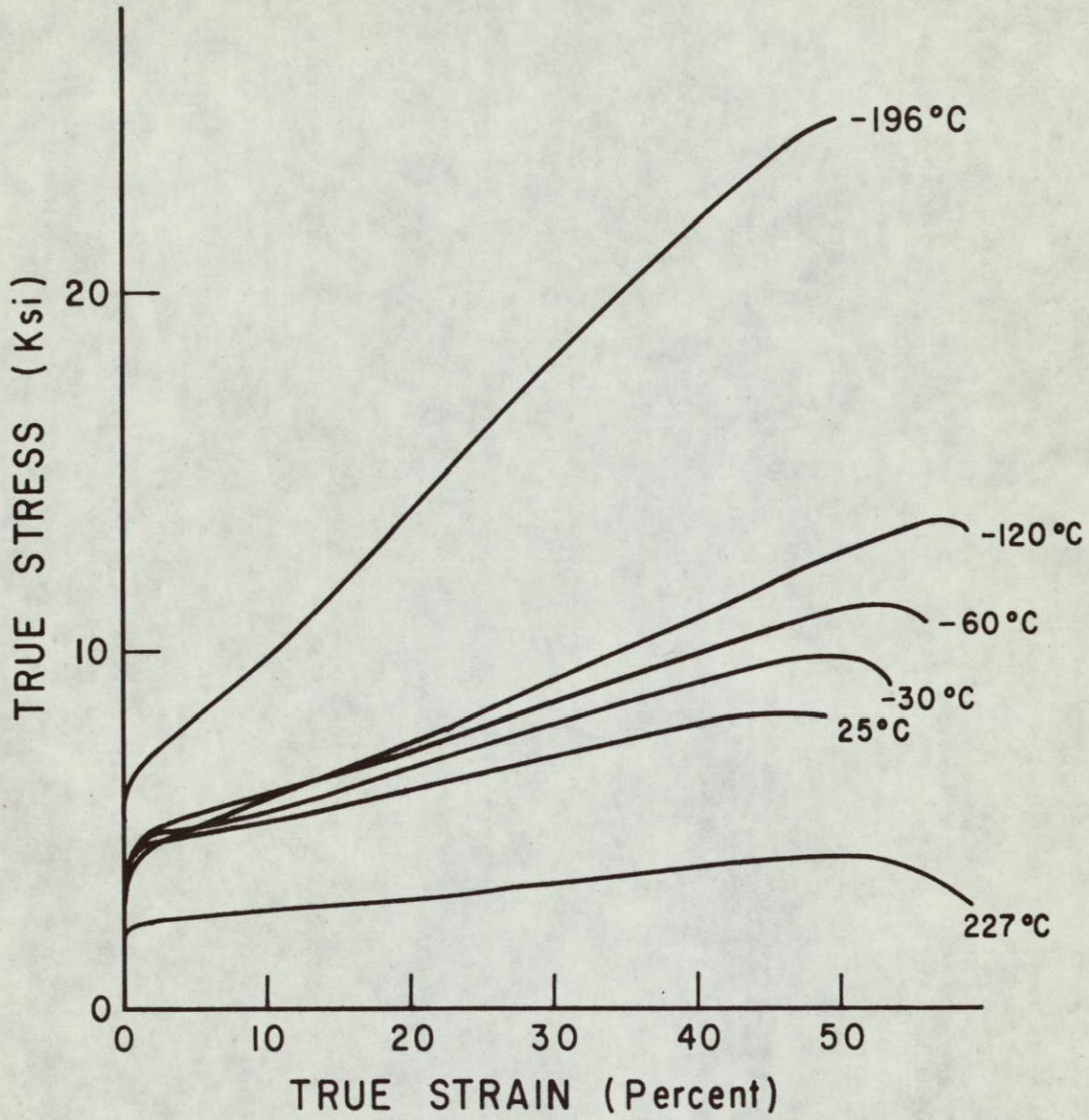

Figure 3.2 THE EFFECT OF TEMPERATURE ON THE MATRIX STRESS-STRAIN CURVE

fibers, the matrix and hence the composite as a whole. If the composite is assumed to obey the concept of combined action, or isostrain behavior, the initial modulus of elasticity can therefore be calculated from the equation[44,45]

$$E_c = V_f E_f + (1 - V_f) E_m$$

The matrix is strained elastically only to about the strain corresponding to the change in the slope of the composite stress-strain curve. Beyond this point it is strained plastically causing the change in the slope of the curve. Since the slope of the stress-strain curve for the matrix in the composite has been reduced from 10×10^6 p.s.i. in the elastic portion of the curve to the work hardening rate $(d\sigma / d\epsilon)_m$ in the plastic portion, the secondary modulus E_c' will be much lower than the initial modulus. Assuming equality of strain, E_c' would be given by[44,45]

$$E_c' = V_f E_f + (1 - V_f)\left(\frac{d\sigma}{d\epsilon}\right)_m \qquad (3.1)$$

The secondary modulus obtained from the composite stress-strain curve was found to be always less than that given by equation (3.1). This difference between the calculated and measured values of the secondary modulus was also reported by Hertzberg, Lemkey and Ford.[44] Equation (3.1) is based on the assumption that the fibers, matrix and composite strain are all equal. However, as will be discussed later, the composite strain can be higher than that of the fibers. Under isostrain conditions the stress supported by the composite σ is given by

$$\sigma = V_f \sigma_f + (1 - V_f) \sigma_m \qquad (3.2)$$

where

$$\sigma \cong E_c' \epsilon_m$$

$$\sigma_f = E_f \epsilon_f$$

$$\sigma_m \cong \left(\frac{d\sigma}{d\epsilon}\right)_m \epsilon_m \quad .$$

Substituting for σ, σ_f and σ_m in equation (3.2) we get

$$E_c' = V_f E_f \left(\frac{\epsilon_f}{\epsilon_m}\right) + (1 - V_f)\left(\frac{d\sigma}{d\epsilon}\right)_m$$

which reduces to equation (3.2) if ϵ_f and ϵ_m are equal. With ϵ_f less than ϵ_m, E_c' will be less than the value calculated from equation (3.2).

The stress-strain curves shown in Fig. 3.1a indicate that both the secondary modulus and the strain at which the slope of the curves changes from the initial to the secondary modulus increases with the decrease in test temperature. This increase in the strain is presumably due to an increase in the stress level required to initiate plastic flow in the matrix as the temperature is lowered, whereas the increase in the slope of the curve in the elastic-plastic region (secondary modulus) is ascribed to the fact that the matrix stress-strain curve is appreciably steeper at lower temperatures.

3.2-1 Mechanism of Fracture

Replicas of the fracture surface of tensile specimens loaded at various test temperatures revealed the existence of elongated dimpled surfaces (Fig. 3.3). These elongated dimples were also reported by Hertzberg *et al.*[44] for specimens tested at room temperature. The dimples

were initiated by failure of the Al_3Ni fibers as they were loaded in tension. Some strain occurred after the fibers failed giving rise to the dimpled surface.

At higher test temperatures the crack tends to propagate at an angle to the stress axis and the dimples would be elongated in the direction of crack propagation, whereas for fracture planes perpendicular to the stress axis, which is the case at lower test temperatures, the dimples assume more of an equiaxed appearance (Fig. 3.4). It appears that the tendency of the crack to divert its direction as it propagates increases with increase in temperature as a result of the matrix becoming weaker and softer as the temperature is raised.

3.2-2 Strain at Failure

The total elongation displayed by the composite at failure ϵ_c was found to vary with the test temperature. Although ϵ_c did not exceed a few percent (2 → 3%), the variation in its magnitude with the test temperature was found to be relatively large. Figure 3.5 indicates that ϵ_c decreases monotonically dropping from a value of 3.5% at -196°C down to 1.75% at 200°C.

Hertzberg, Lemkey and Ford[44] extracted Al_3Ni fibers from the aluminum matrix using a 3 pct aqueous HCl^3 solution. They tested several fibers in tension employing a technique developed by Lemkey and Kraft.[18] The results obtained proved that the fibers exhibited elastic behavior all the way to their failure point, which occurred by cleavage. Plastic flow in the matrix results in effective loading of the fibers and they would therefore support the greater portion of the load. When the fibers fail, the composite would do likewise and the total elongation

Figure 3.3 AN ELECTRON MICROSCOPE PHOTOGRAPH FOR THE FRACTURE SURFACE OF A TYPE A TENSILE SPECIMEN TESTED AT 25°C, MAGNIFICATION = 10,000X.

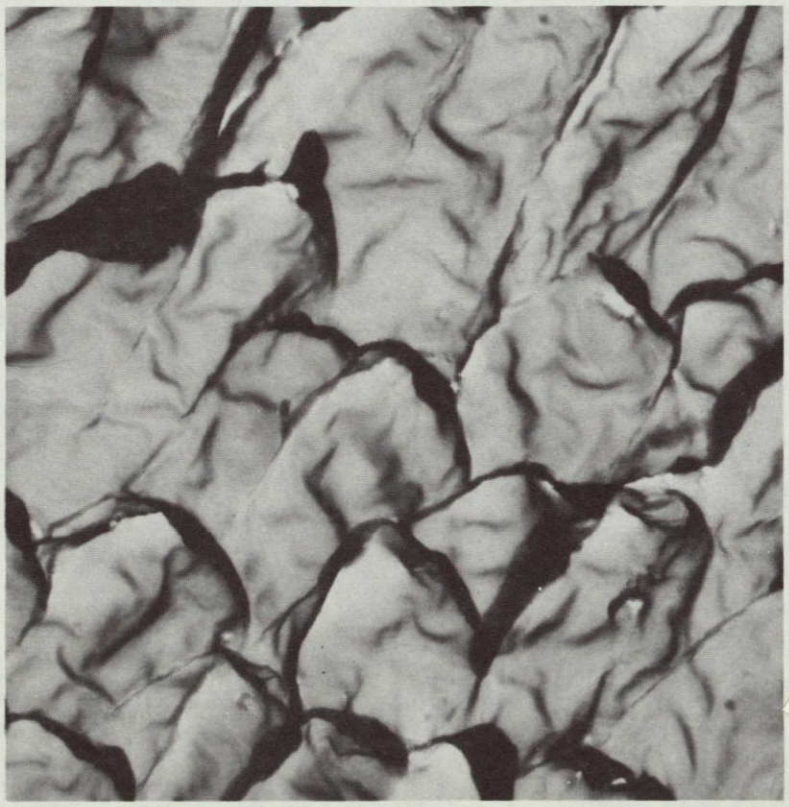

Figure 3.4 AN ELECTRON MICROSCOPE PHOTOGRAPH FOR THE FRACTURE SURFACE OF A TYPE A TENSILE SPECIMEN TESTED AT -196°C, MAGNIFICATION = 10,000X.

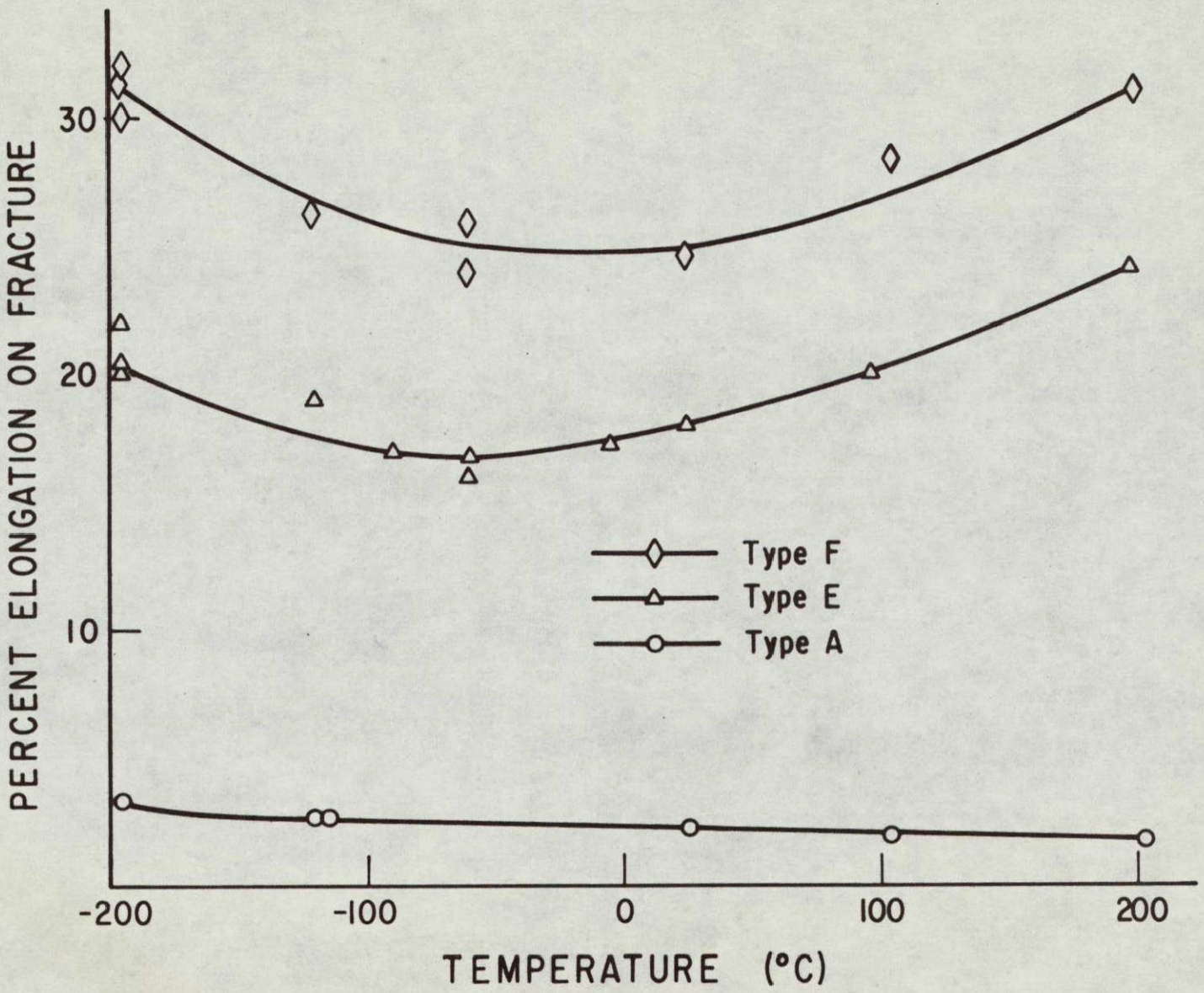

Figure 3.5 THE EFFECT OF TEMPERATURE ON THE FAILURE STRAIN OF THE TENSILE SPECIMENS

exhibited by the latter would be determined mainly by the fiber failure strain ϵ_{fb}. Individual fibers obtained by acid dissolution of the matrix[44] exhibited an average failure strain of about 1.8% at room temperature as compared to 2% for that of the composite at the same temperature. Since no change in the failure mechanism was observed over the temperature range in question, the decrease in the composite failure strain with the increase in temperature was therefore ascribed to a decrease in ϵ_{fb} as the temperature was raised.

Since the behavior of the Al_3Ni fibers is elastic all the way to failure, the variation in σ_{fb} with temperature will be similar to that of ϵ_{fb}, which means that σ_{fb} decreases as the temperature is raised. This is in agreement with the experimental observation that the strength of almost all intermetallic compounds decreases with increase in test temperature.

In isostrain mode of loading, matrix, fiber and composite strain are all equal and for a composite with V_f greater than V_{min}, the composite failure strain would be equal to the elastic failure strain of the fibers. However, the concept of equality of strain is not valid in later regions of deformation where the aluminum matrix starts to behave plastically. The composite strain can be higher than the fiber strain. This is caused by premature fiber failure giving rise to matrix-fiber strain inequality. The strain inequality is dependent upon the number and size of voids formed by premature fracture of the Al_3Ni fibers. This means that at a given temperature the strain inequality should increase with increasing applied stress since more fibers are expected to crack and the already formed voids will grow larger at higher stress.

3.2-3 Premature Fiber Fracture

A number of specimens were loaded to various fractions of the maximum stress at different test temperatures. Cracked fiber counts were made on the specimen surfaces that were polished and electropolished as described previously. Polishing would preclude fibers that might have been exposed on the free surface of the specimen during straining. The appearance of a cracked fiber is shown in Fig. 3.6. Counts were made by scanning the surface in slightly overlapping passes in the transverse direction at a magnification of 1000. The specimen was held on the microscope stage with the tensile axis aligned normal to the direction of scan. A problem arises in counting cracked fibers, in that not all fibers are perfectly parallel to the polished specimen surface and consequently some cracks will not be seen.

The number of cracked fibers expressed as the number per unit area is shown in Fig. 3.7a as a function of the applied stress σ at various test temperatures. It is noted that under increasing applied stress, the density of cracked fibers increases.

Figure 3.7a indicates that the rate at which premature fiber cracking proceeds does not increase with the increase in applied stress and that cracked fibers represent only a small fraction of the total fiber population even at stresses as high as 0.9 σ_c; for example the number of cracked fibers at a stress level of 0.9 σ_c in a specimen tested at room temperature represents only 1/2% of fiber population. These observations indicate that premature cracking does not set up a chain reaction that could lead to failure on a large scale in the remaining fibers. Premature fiber fracture does not, therefore, lead to

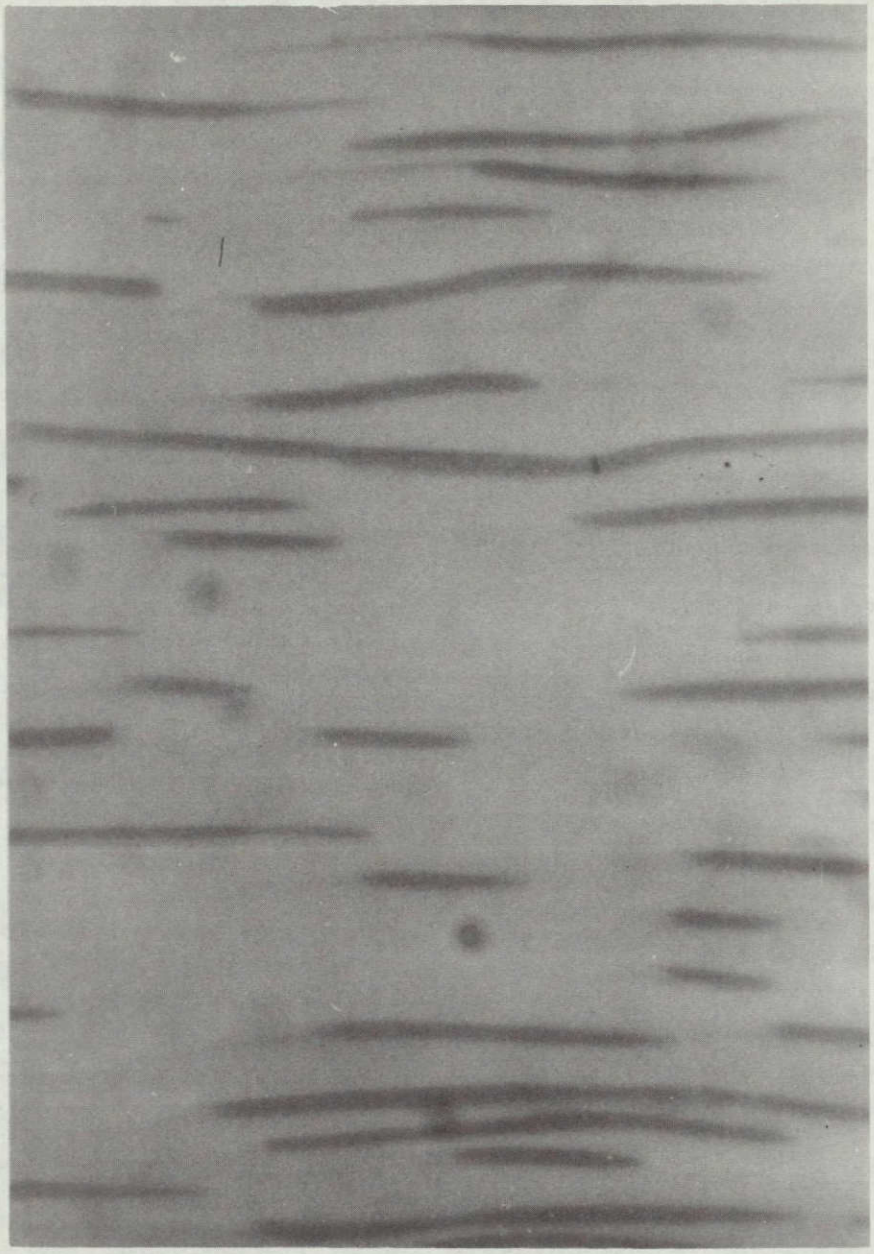

Figure 3.6 A PREMATURELY CRACKED FIBER, MAGNIFICATION = 2500X.

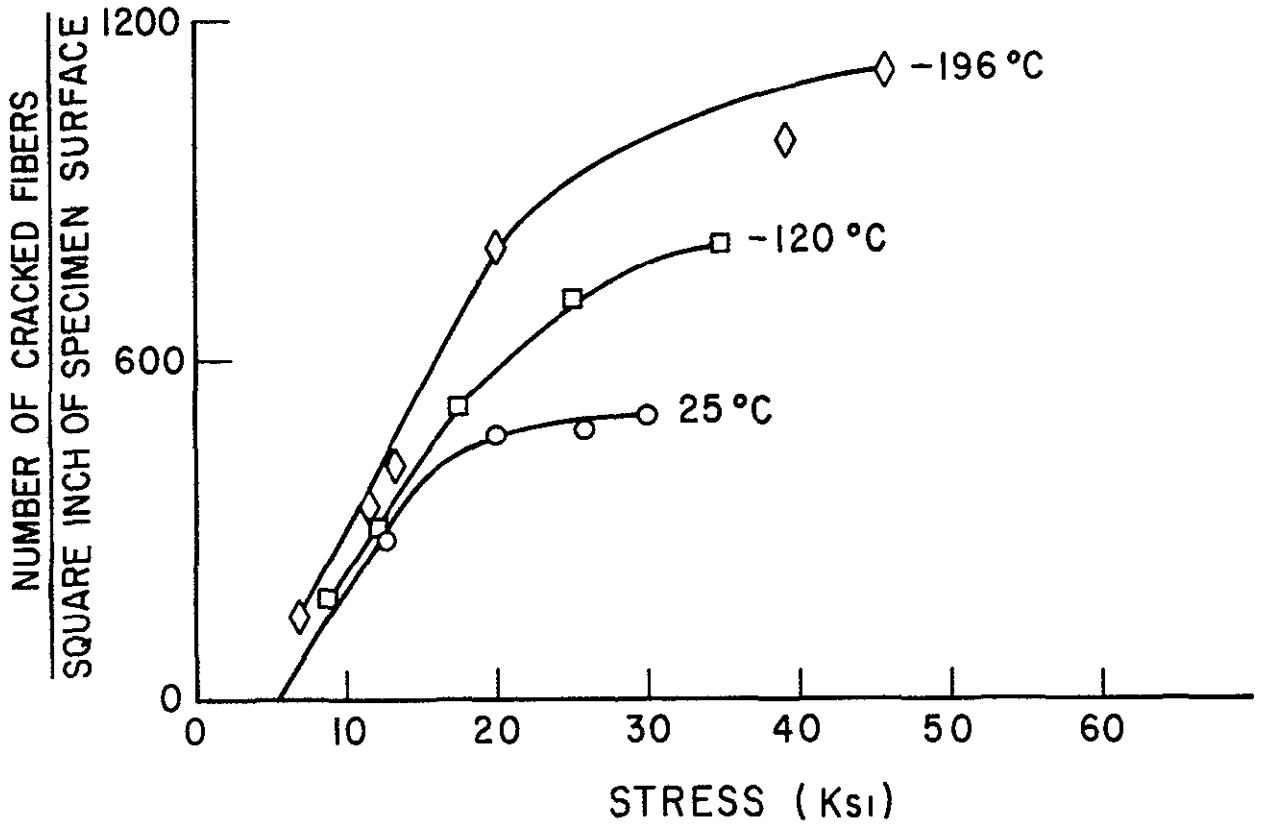

Figure 3 7a THE VARIATION OF THE NUMBER OF CRACKED FIBERS WITH THE APPLIED STRESS

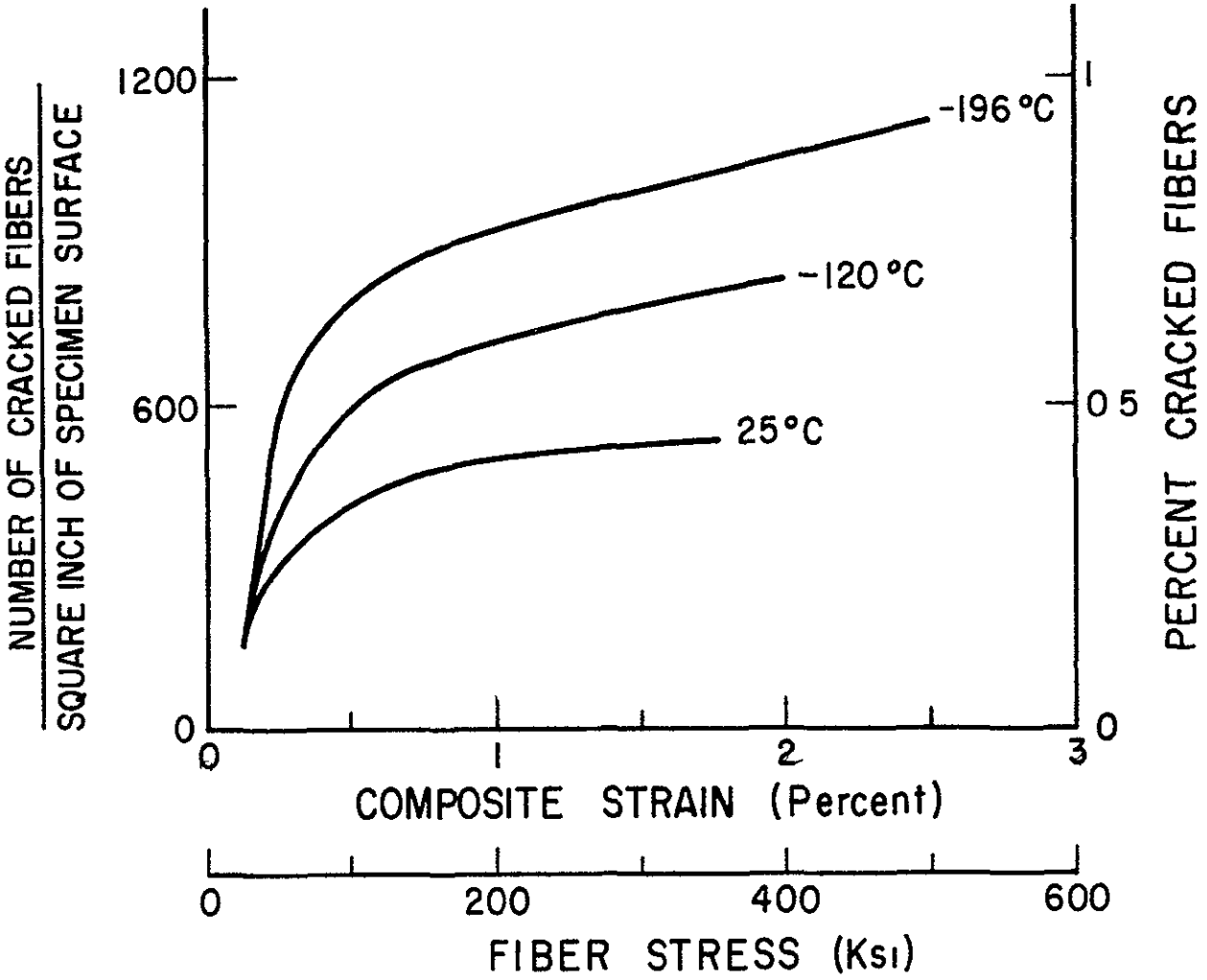

Figure 3.7b THE VARIATION OF THE NUMBER OF CRACKED FIBERS WITH THE COMPOSITE STRAIN

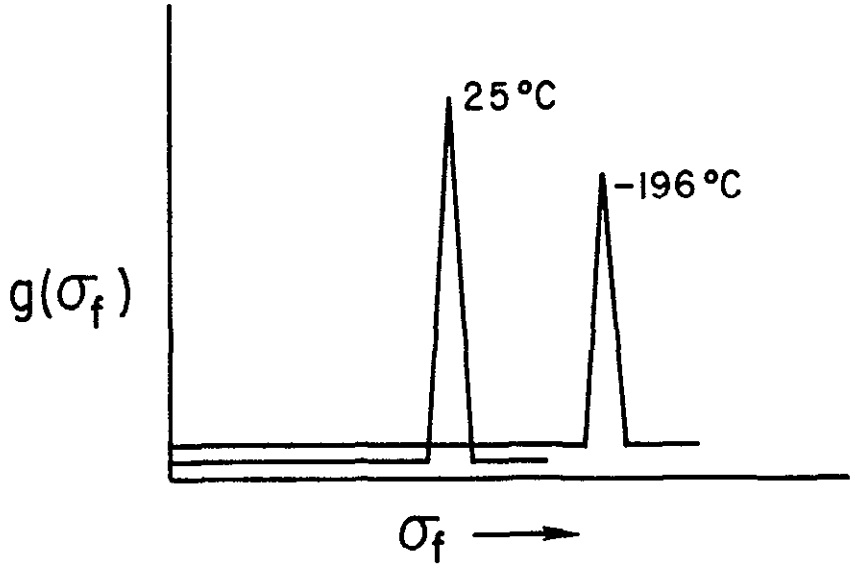

Figure 3.7c SCHEMATIC REPRESENTATION OF FIBER STRENGTH DISTRIBUTION FUNCTION AS OBTAINED FROM COUNTING OF CRACKED FIBERS

instability, and the composite strength is determined primarily by the average fiber strength

For the same applied stress the number of cracked fibers was found to be larger for specimens loaded at lower temperatures For example the percentage of cracked fibers in a cross section of a specimen loaded to 30 Ksi increased from about 1/2% at room temperature to about 1% at -196°C Although the number of prematurely cracked fibers increases as the temperature is lowered, the number of fracture sites is still not enough to incite a ductile failure mechanism in the material (growth and coalescence of voids) Since premature cracking does not lead to instability (number of cracked fibers does not increase rapidly with increase in applied stress), the greater number of fibers would remain intact and carry the bulk of the load, thus inhibiting ductile failure of the material.

Knowing the stress-strain relationship of the composite (Fig 3 1a), the number of prematurely cracked fibers can be plotted as a function of the composite strain to give the curve shown in Fig 3 7b If one assumes that the fiber strain is equal to that of the composite (isostrain), the relationship shown in Fig 3 7b would also represent the variation of the number of prematurely cracked fibers with the fiber strain ϵ_f, or the fiber stress σ_f (σ_f is related to ϵ_f by the elastic modulus E_f)

In the statistical approach discussed in Chapter I, it is assumed that the fibers are characterized by a distribution function of the Weibull type The fraction of cracked fibers at a fiber stress σ_f is related to the cumulative distribution function $G(\sigma_f)$ That is,

$$G(\sigma_f) = \int_0^{\sigma_f} g(\sigma_f) d\sigma_f$$

For $g(\sigma_f)$ given by equation (1 10), $G(\sigma_f)$ would be

$$G(\sigma_f, \alpha, \beta) = 1 - e^{-L\alpha\sigma_f^{\beta}}$$

Substituting for $L\alpha$ from equation (1.11), the above equation reduces to

$$G(\sigma_f, \alpha, \beta) = 1 - e^{-\left(\frac{\sigma_f}{\bar{\sigma}_{fb}}\right)^{\beta} \Gamma\left(1+\frac{1}{\beta}\right)} \qquad \beta > 1 \qquad (3\ 3)$$

Equation (3 3) indicates that the fraction of cracked fibers increases rapidly with the increase in fiber stress σ_f, thus becoming a considerable fraction of the fiber population as σ_f increases A change in α and β with temperature leads to a change in fraction of cracked fibers, for example a smaller value of β at lower temperatures could lead to more cracks even though $\bar{\sigma}_{fb}$ is larger at lower temperatures [equation (3 3)]

The implications of equation (3 3) are not in agreement with the experimental observations (Fig 3.7) and it thus follows that the Al_3Ni fibers can not be characterized by a strength distribution function of the type given by equation (1 10)

For simplicity, it is assumed that the variation in the fraction of cracked fibers with the fiber stress σ_f (Fig 3 7b) is given by

$$G(\sigma_f) = \begin{cases} c_1 \sigma_f & 0 < \sigma_f < (\sigma_f)_o \\ c_2 \sigma_f + d_2 & (\sigma_f)_o < \sigma_f \end{cases}$$

where $(\sigma_f)_o$ is the stress at which the curves, shown in Fig. 3.7b, change slope, and c_1, c_2 and d_2 are constants

It follows that

$$G(\sigma_f) = \begin{cases} c_1\sigma_f = \int_o^{\sigma_f} g(\sigma_f)d\sigma_f & o < \sigma_f < (\sigma_f)_o \\ \\ c_2\sigma_f + d_2 = c_1(\sigma_f)_o + \int_{(\sigma_f)_o}^{\sigma_f} g(\sigma_f)d\sigma_f(\sigma_f)_o < \sigma_f \end{cases}$$

which yields

$$g(\sigma_f) = \begin{cases} c_1 & o < \sigma_f < (\sigma_f)_o \\ \\ c_2 & (\sigma_f)_o < \sigma_f \end{cases}$$

A schematic representation of $g(\sigma_f)$ as obtained above is shown in Fig. 3 7c At -196°C, c_1 and c_2 have the values 10^{-2} and 10^{-3}, respectively, and at 25°C, they are about 2 5 x 10^{-3} and 10^{-4}, where σ_f is in k s i The reason for the tensile specimens showing more premature cracked fibers at -196°C is not understood

Acoustic Emission Analysis When a material is subjected to loads it emits low level sound, a phenomenon known as acoustic emission These sounds are associated with permanent deformation processes such as twinning, slip, microcrack formation, etc.[46-48]

Acoustic emission from specimens loaded in tension was counted and recorded as a function of the applied stress and strain The sound emitted by the loaded specimens was picked up by a sensing transducer, passed on to a set of amplifiers and then over to counters

to detect the number of acoustic emission pulses detected by the transducer One counter was set to measure incoming counts per second, another was set to measure the total number of incoming counts as the test proceeded In one of the tests, the high frequency output of the amplifier was converted into frequency within the audible range and the sound appeared to correspond to individual fibers as they broke. It thus appears that the emission is mainly due to fibers as they crack in the course of loading the specimen The relationship between the acoustic emission rate $\dot{N}$ (number of counts detected per second) and stress and strain is shown in Figures 3 8 and 3 9 Figures 3 9 and 3 10 show the variation in the total acoustic emission N with the stress and strain in the specimen The relationship between N and σ qualitatively agrees with the number of cracked fibers determined as a function of applied stress for a specimen loaded at room temperature (Fig 3 7a) Whereas cracked fibers were counted only on the specimen surface, acoustic emission corresponded to fibers cracking within the bulk of the specimen as well

N, as plotted in Fig 3 10, represents the total acoustic emission as a function of composite or fiber strain (assuming isostrain conditions) Since ϵ_f is related to σ_f by the fiber elastic modulus E_f, the curve shown in Fig 3 10 would also represent the relationship between N and σ_f The acoustic emission from a fiber is related to the elastic energy released as the fiber breaks The emission accompanying the failure of a fiber at a certain stress level is expected to be more than the emission from a fiber failing at a lower stress This explains the higher values of N observed at higher strains (Fig 3 9)

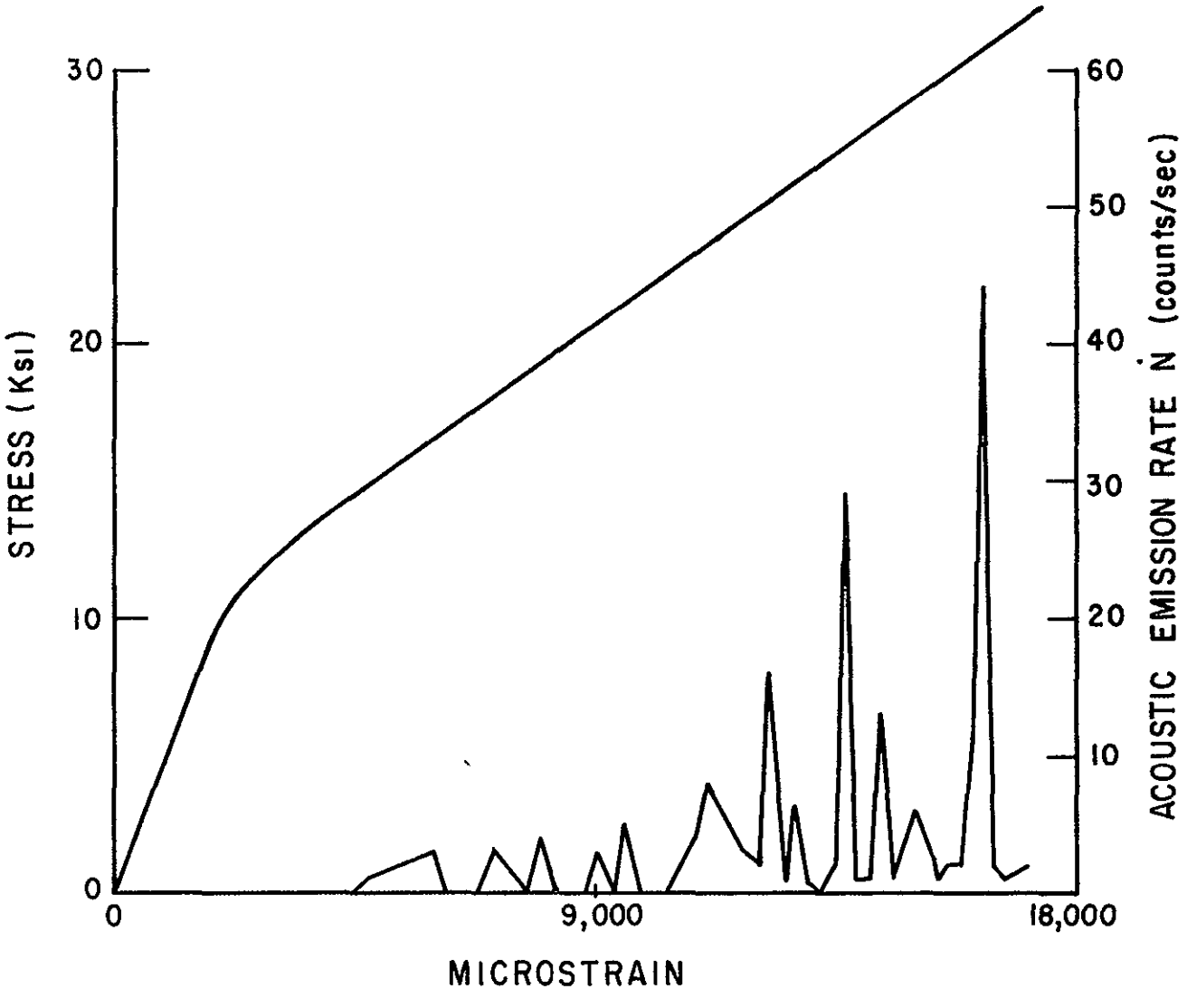

Figure 3 8 STRESS AND ACOUSTIC EMISSION RATE AS FUNCTIONS OF STRAIN

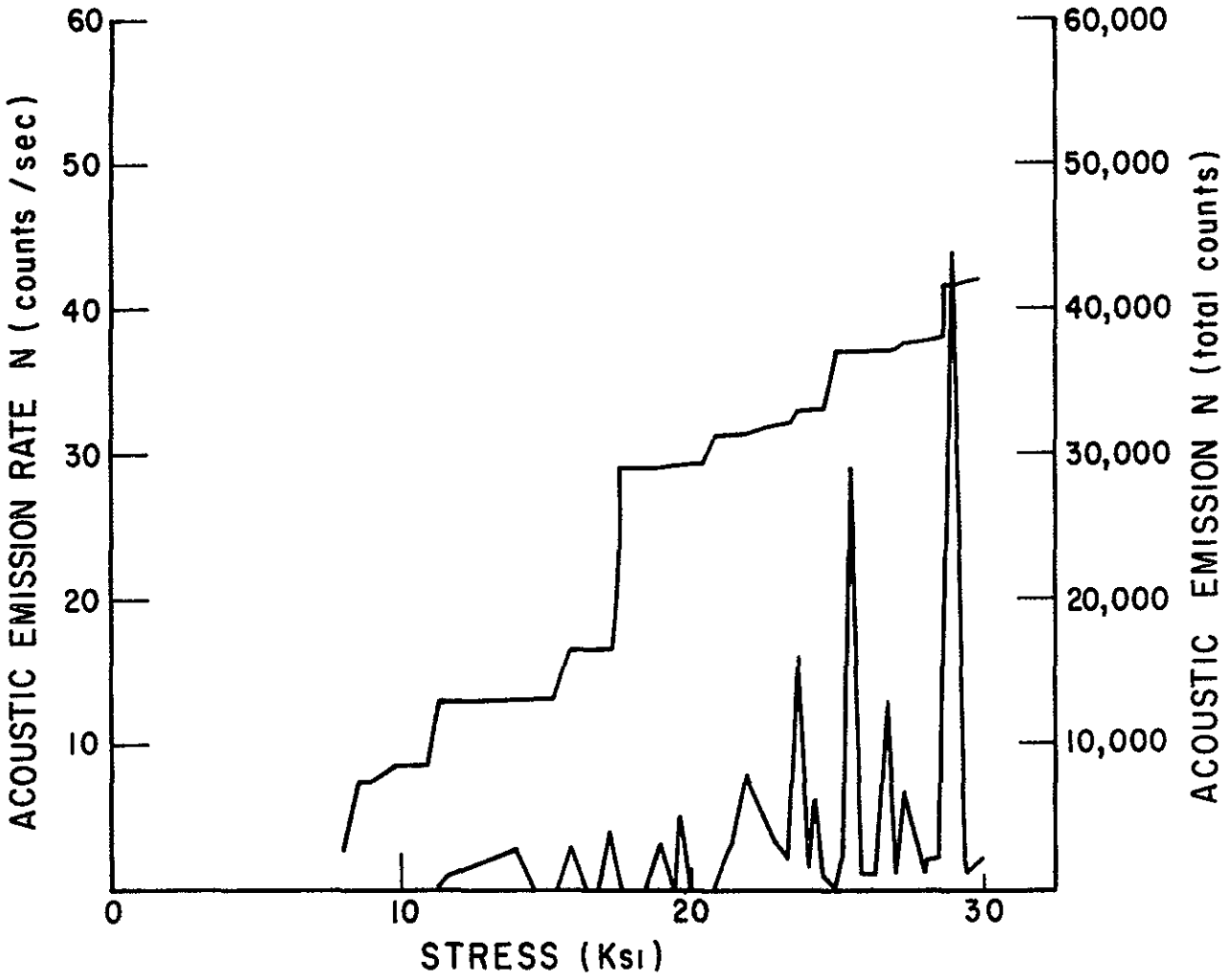

Figure 3 9 ACOUSTIC EMISSION RATE AND TOTAL ACOUSTIC EMISSION AS FUNCTIONS OF STRESS

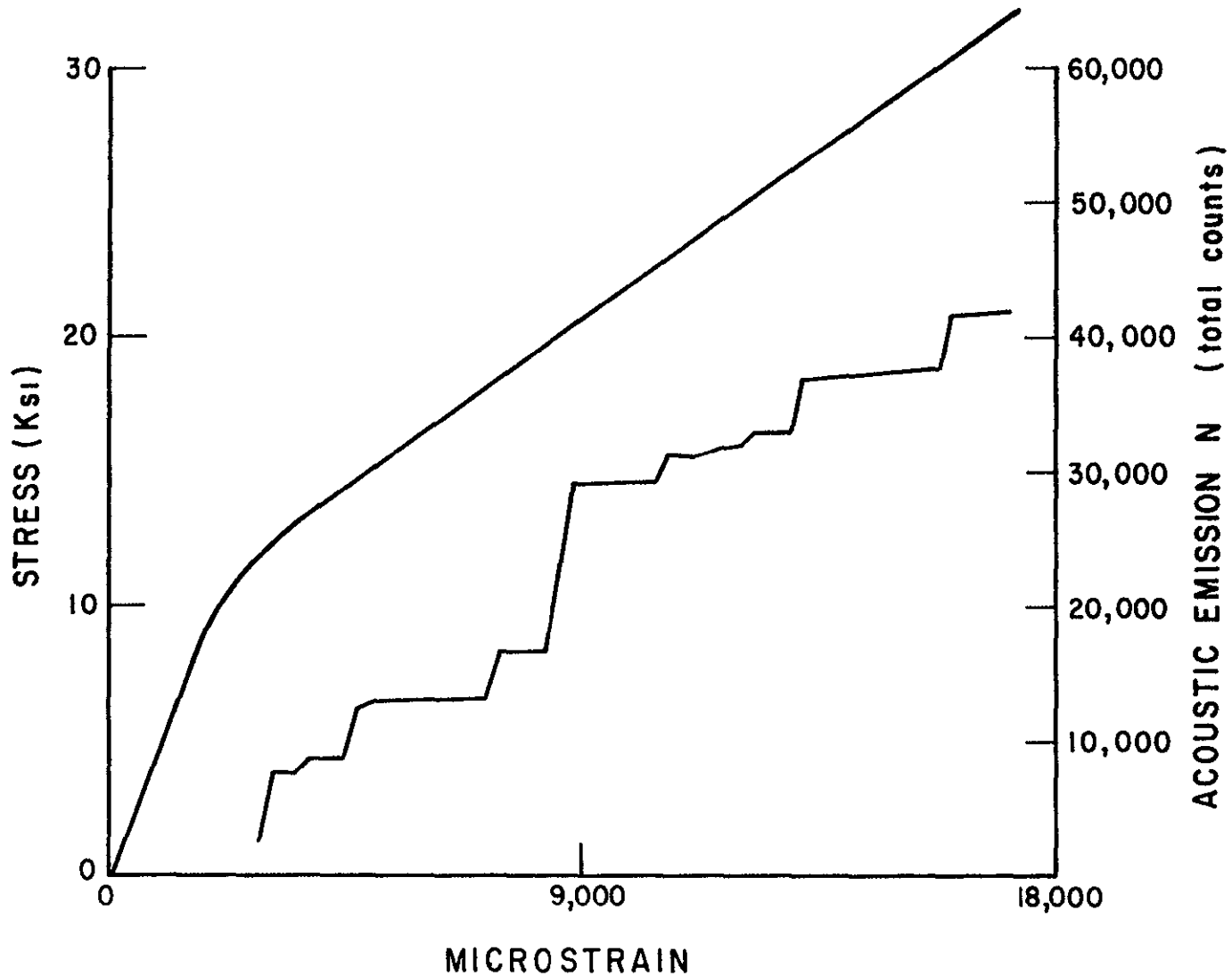

Figure 3.10 TOTAL ACOUSTIC EMISSION AS A FUNCTION OF STRAIN

3 2-4 Fiber Strength

The difference between the composite and fiber strains at failure ($\epsilon_c - \epsilon_{fb}$) is related to the number of fracture sites (produced by premature fiber failure) This number was shown to be larger for specimens tested at lower temperatures However, the cracks develop into pores and these grow with increasing stress at a faster rate at higher temperatures The difference between ϵ_c and ϵ_{fb} could thus be assumed to be the same at the various test temperatures.

Tensile test conducted on fibers extracted from the composite by acid dissolution of the matrix, revealed that they possess tensile strength levels of 300,000-400,000 p.s i at room temperature [44,49] If a value of 350,000 p s.i is taken as an average for fiber strength at room temperature, the failure strain of the fibers would therefore be 1 75% as compared to 2% which is the average total elongation displayed by the composite at failure The relationship between ϵ_c and temperature can thus be modified to give the variation of ϵ_{fb} with temperature, and since σ_{fb} is related to ϵ_{fb} through the fibers modulus of elasticity E_f, the dependence of σ_{fb} on temperature is calculated to give the curve shown in Fig 3 11

3 3 Composite Tensile Strength

Variation of the composite ultimate strength with temperature has been obtained experimentally and is shown in Fig 3 12 It is noted that the composite strength decreases monotonically with the test temperature The decrease in strength with temperature was also reported by Salkind et al [50] in the range 25°C → 500°C The curve in Fig 3 12

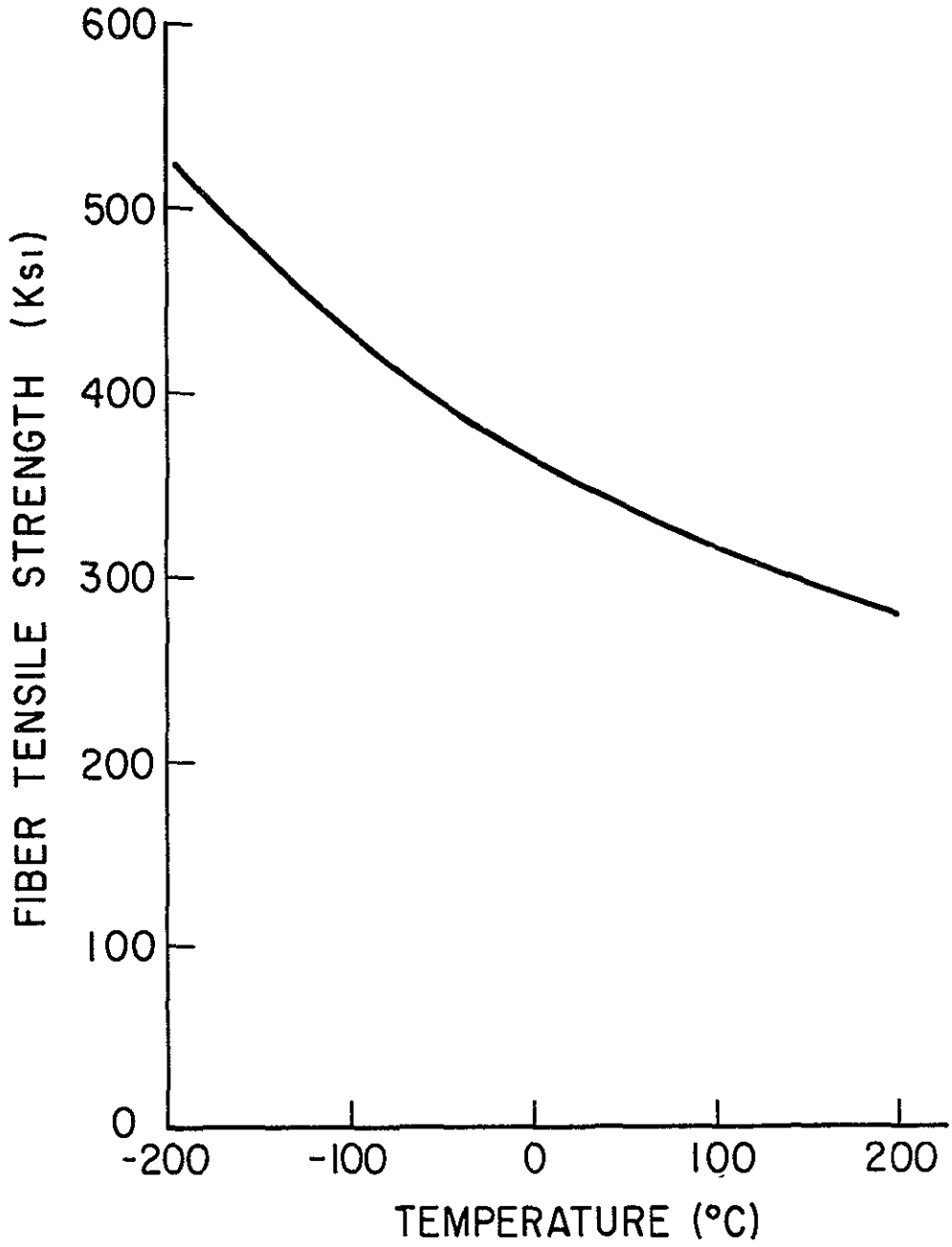

Figure 3.11 THE VARIATION OF FIBER STRENGTH WITH TEMPERATURE

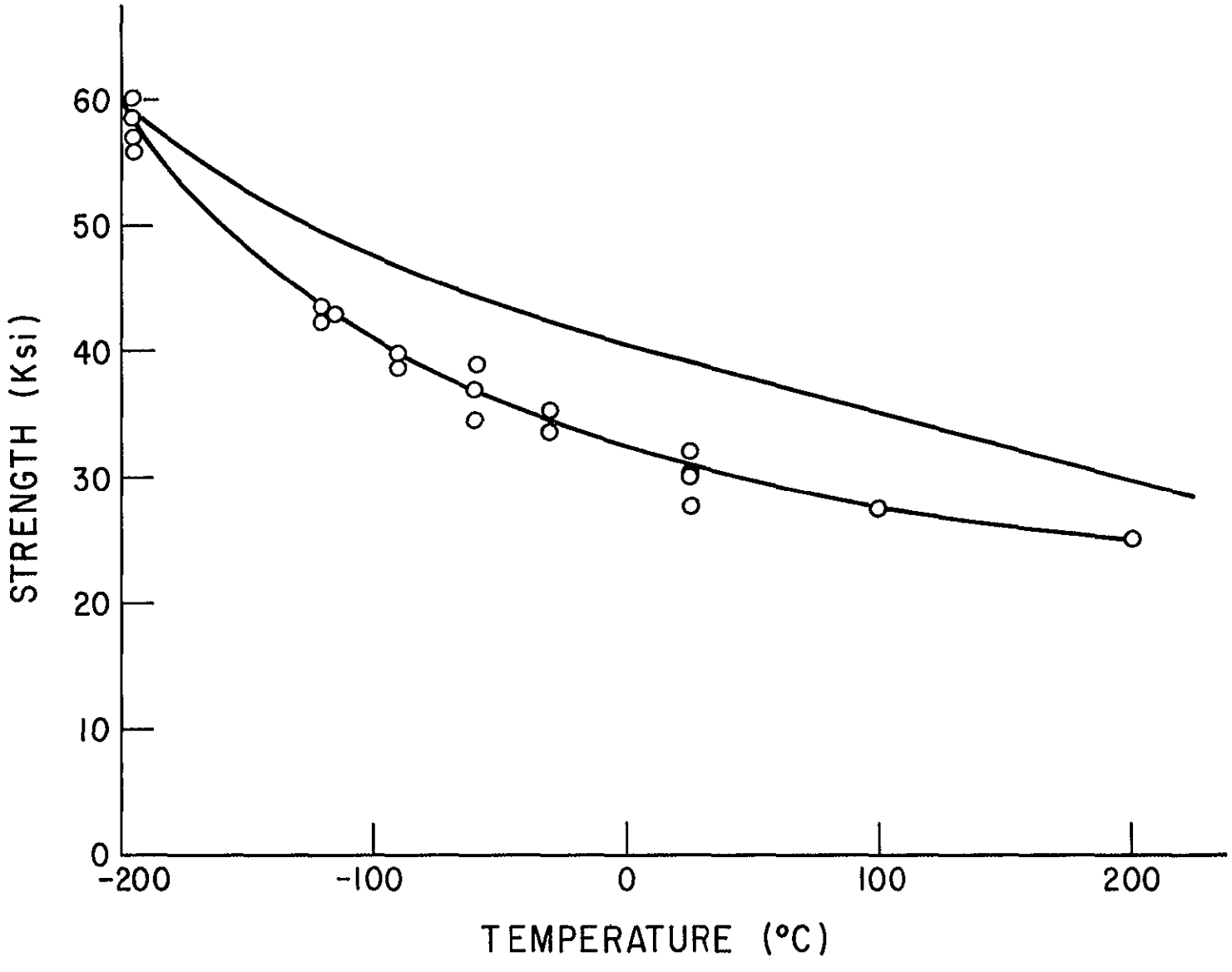

Figure 3 12 THE VARIATION OF THE COMPOSITE LONGITUDINAL STRENGTH WITH THE TEST TEMPERATURE

depicts a decrease in the composite longitudinal strength from a value of 60,000 p s i at -196°C down to about 30,000 p s i at room temperature Change in the properties of the composite constituents with temperature is reflected on the composite strength giving rise to the observed strength temperature dependence

3 3-1 Prediction of Composite Strength

The theories pertaining to computing the composite tensile strength from knowledge of the constituents behavior were discussed in Chapter I Al_3Ni fibers obtained by matrix dissolution were found to have very high aspect ratios The aspect ratio of the fibers (L/d) >> the critical aspect ratio (L_c/d), and therefore the average stress carried by the fibers at failure would be very close to σ_{fb} If each of the two constituents is assumed to behave independently (concept of combined action), σ_c would be given by

$$\sigma_c = V_f \sigma_{fb} + (1 - V_f) \sigma_m' \qquad (1\ 1)$$

where σ_m' is the stress borne by the matrix at the point of fiber failure Equation (1.1) is valid only for a composite with V_f greater than V_{min} which was shown to be the case for the Al - Al_3Ni eutectic alloy

The value of σ_m' is obtained from the stress-strain curve of the matrix corresponding to a strain which is equal to the composite failure strain σ_{fb} and σ_m' vary with temperature and so will σ_c Strength as calculated using equation (1 1) is shown in Fig 3 12 together with the experimentally determined values

It was assumed[11] that the decrease in composite strength with temperature is related to a decrease in the modulus of the reinforcing

phase and shear strength of the matrix Equation (1 1) indicates that the load supported by the composite at failure is mainly carried by the fibers and therefore the variation of fiber ultimate strength with temperature is of predominating importance in determining the composite strength temperature dependence

Decrease in matrix strength with temperature although significant will play only a small part since σ_m' is small as compared to $V_f \sigma_{fb}$. The fact that the total elongation displayed by the composite at fracture decreases with temperature indicates that the decrease in composite strength is mainly due to a decrease in σ_{fb} rather than a decrease in E_f

Strength Model Equation (1 7) gives the shear stress distribution along the fiber-matrix interface for an effective applied load P_{eff} This equation is valid only for the case where both the fibers and matrix are behaving elastically. As indicated by the composite stress-strain curves (Fig 3 1a), the matrix is expected to pass into plastic state before the composite fails, and therefore it is necessary to find the stress distribution along a fiber that is embedded in a plastic matrix

The plasticity of the matrix can be taken into account by introducing a number of simplifying assumptions.[26] The matrix stress-strain curve at a given temperature is linearized, an example of this is given in Fig 3 13. The linearization of the curve would lead to a number of stress ranges depending upon the number of discontinuities introduced in the stress-strain curve In each of the four ranges shown in Fig 3 13, the relationship between the stress and strain is linear

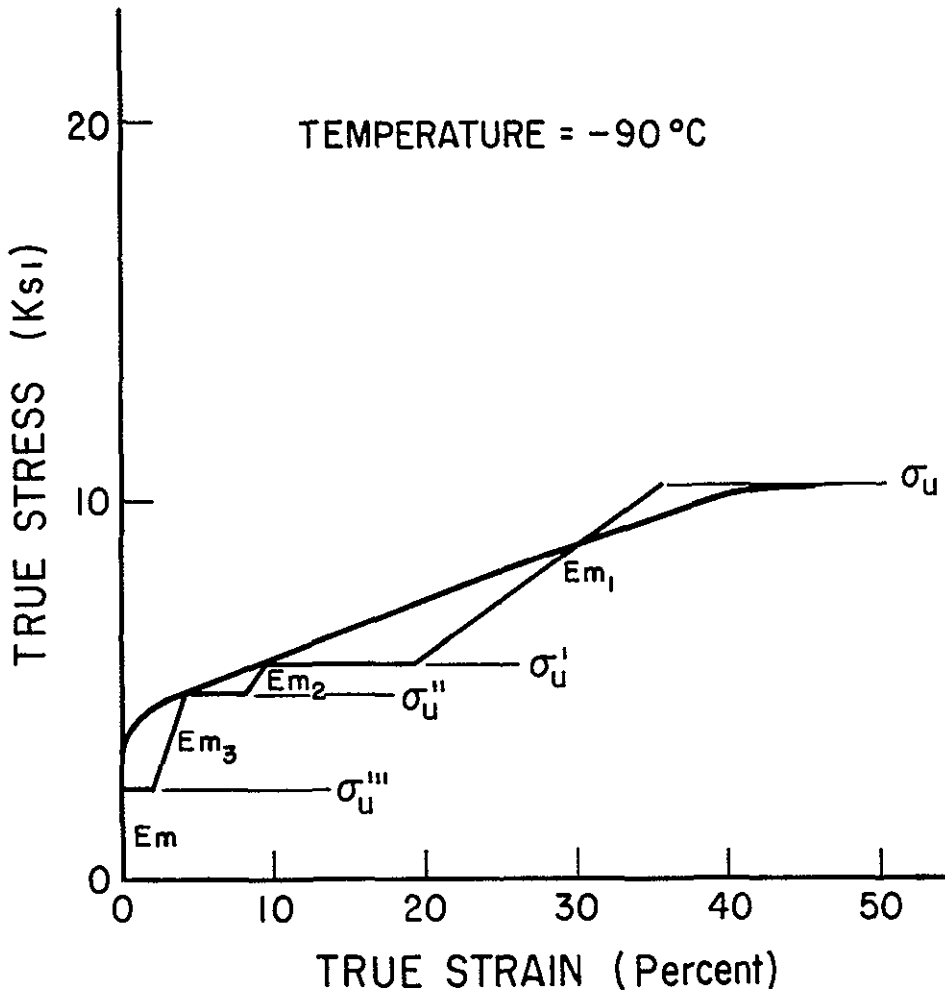

Figure 3 13 LINEARIZATION OF THE MATRIX STRESS-STRAIN CURVE

with the secant modulus equal to the tangent modulus The slope of the idealized stress-strain curve in the different stress ranges is higher at lower temperature, this is due to the increase in $d\sigma/d\epsilon$ with reducing test temperature Values of the slope E_m, and the stress levels corresponding to the points of discontinuities on the idealized curve are given in Table 3 1

Attention is then focused on a single fiber of length 2ℓ and a cross section that is assumed circular with a diameter d As previously mentioned, the Al_3Ni fiber shape, generally elliptical in cross section, approaches that of a circle at fast solidification rates. d was therefore estimated by averaging a large number of measurements made on transverse microsections The fiber is embedded in a matrix which extends radially all around the fiber and along its entire length The ratio between the cross sectional area of the matrix and fiber is taken to be equal to 9 which is the volume fraction ratio of the composite constituents The fiber-matrix model is taken to represent the composite and the composite strength is defined as the tensile stress σ_c that has to be applied in order for the axial stress in the fiber to build up to the fiber breaking stress σ_{fb}, which is taken as the average fiber breaking strength at the temperature in question Such a definition is consistent with the observation that premature fiber cracking does not lead to instability and also with the experimental observations on the fracture surfaces previously discussed

The state of the applied stress σ_c is shown in Fig 3 14 The load applied to the composite corresponding to the stress σ_c will be divided up between the fiber and the surrounding matrix in the ratio of

TABLE 3.1

ELASTIC MODULI AND STRESS LEVELS CORRESPONDING TO THE POINTS OF DISCONTINUITIES ON THE IDEALIZED MATRIX STRESS-STRAIN CURVE

Temperature	$d\sigma/d\varepsilon$ (Ksi)	E_{m_1} (Ksi)	E_{m_2} (Ksi)	E_{m_3} (Ksi)	σ_u (Ksi)	σ_u' (Ksi)	μ	σ_u'' (Ksi)	ν	σ_u''' (Ksi)
-196°C	40 0	80.0	160.0	320 0	24.6	8.2	0.33	7.4	0.30	4 8
-120°C	16 5	33 0	66 0	132.0	13.6	5 8	0.42	5 0	0.36	2.6
- 90°C	14 7	29 4	58 8	117 6	10.5	5.7	0 54	4.8	0.45	2.4
- 60°C	13.3	26.6	53.2	106.4	11.0	6 2	0.56	5.4	0.49	2.4
- 30°C	10 0	20.0	40 0	80.0	10 0	6 4	0 64	5.4	0 54	2.4
25°C	8 0	16 0	32 0	64.0	8.2	6.2	0.75	5.2	0.63	2.2
85°C	9 0	18.0	36.0	72 0	8.4	4 8	0.57	4.2	0 50	2.0
116°C	6 5	13 0	26 0	52 0	7 2	5 0	0.70	4 2	0.58	1.8
153°C	6.0	12.0	24 0	48.0	5.8	3 6	0.62	3.2	0.55	1.4
227°C	4 0	8.0	16 0	32 0	4 3	3 0	0.70	2.8	0 65	1.2

$\mu = \sigma_u'/\sigma_u$

$\nu = \sigma_u''/\sigma_u$

their cross sections Therefore, a load $\sigma_c A_m$ is assumed applied to the matrix and a load $\sigma_c A_f$ is applied to the fiber [24,29] It should be noted that the center of the fiber is located at the point $z = 0$, where z is the distance measured along the fiber axis from its center as depicted in Fig 3 14 The lowest value of the axial stress in the fiber is σ_c at the point $z = \ell$ As z decreases, the axial stress in the fiber builds up whereas the stresses in the matrix parallel to fiber axis decreases as a result of load transfer to the fiber via the interfacial shear stresses developed

The slope of the stress-strain curve (secant modulus) of the matrix, surrounding the fiber, in the different stress ranges is assumed to be given by the corresponding slope of the idealized matrix curve However, since the tensile stress in the matrix at the end of the fiber σ_c is higher than σ_u (matrix ultimate strength), the stress levels corresponding to the discontinuities in the stress-strain curve will be proportionately raised above those corresponding to the discontinuities in the matrix stress-strain curve without any fibers The constant of proportionality is σ_c/σ_u

The fiber-matrix model is then broken up into segments with each of the segments corresponding to one of the stress ranges A segment is treated as a part of an elastic continuum to which equation (1 7) (treating the case of an elastic fiber in an elastic matrix) can be applied using the elastic constants given by the slope of the stress-strain curve in the particular segment The segment at the fiber end will have the lowest modulus E_{m_1}

The effective load differential between fiber and matrix for the case where the load is applied to both is given by equation (1.9) and for a segment where the matrix is still elastic, P_{eff} would be given by

$$P_{eff} = A_m \frac{\sigma_m E_f - \sigma_f E_m}{E_f}$$

where

σ_m = stress applied to matrix

σ_f = stress applied to fiber

If the matrix is to transfer load to the fiber, P_{eff} should be positive and therefore the following inequality has to be satisfied

$$\sigma_m E_f > \sigma_f E_m$$

That is,

$$2\sigma_m > \sigma_f$$

Since the axial stress in the fiber σ_f builds up fast [equation (1 5)] from its value σ_c at fiber end ($\sigma_f > \sigma_c$), whereas tensile strength in matrix decreases with distance from fiber end ($\sigma_m < \sigma_c$), the inequality will not be satisfied. This means that the fiber would start transferring load to the matrix at the point where P_{eff} changes sign and high shear stresses would be developed Experimentally[24] shear stresses were found to be higher only at fiber ends The matrix-fiber model will therefore have no segment where the matrix has an elasticity modulus of $E_m(10 \times 10^6$ p s i)

The state of stress at the end of each segment is shown in Fig 3 15 Segment lengths are assumed to be (ℓ-n), (n-m) and m The effective load producing interfacial shear stress and the shear stress distribution would be given by

$$P_{eff} = \sigma_c \frac{A_m(E_f - E_{m_1})}{E_f}$$

$$\tau_J = \frac{\lambda}{4}\left[\sigma_c \frac{A_m(E_f - E_{m_1})}{A_f E_f + A_m E_{m_1}}\right] \frac{\sinh \frac{\lambda_1 z}{d}}{\cosh \frac{\lambda_1 \ell}{d}} \qquad n < z < \ell$$

$$P_{eff} = A_m \frac{\sigma_c' E_f - \sigma_f(n) E_{m_2}}{E_f}$$

$$\tau_J = \frac{\lambda}{4}\left[A_m \frac{\sigma_c' E_f - \sigma_f(n) E_{m_2}}{A_f E_f + A_m E_{m_2}}\right] \frac{\sinh \frac{\lambda_2 z}{d}}{\cosh \frac{\lambda_2 n}{d}} \qquad m < z < n$$

$$P_{eff} = A_m \frac{\sigma_c'' E_f - \sigma_f(m) E_{m_3}}{E_f}$$

$$\tau_J = \frac{\lambda}{4}\left[A_m \frac{\sigma_c'' E_f - \sigma_f(m) E_{m_3}}{A_f E_f + A_m E_{m_3}}\right] \frac{\sinh \frac{\lambda_3 z}{d}}{\cosh \frac{\lambda_3 m}{d}} \qquad o < z < m$$

where λ is a parameter obtained by substituting the appropriate elastic constants into equation (1.9)

Considering fiber and matrix equilibrium in each of the three segments, the following equations would be obtained

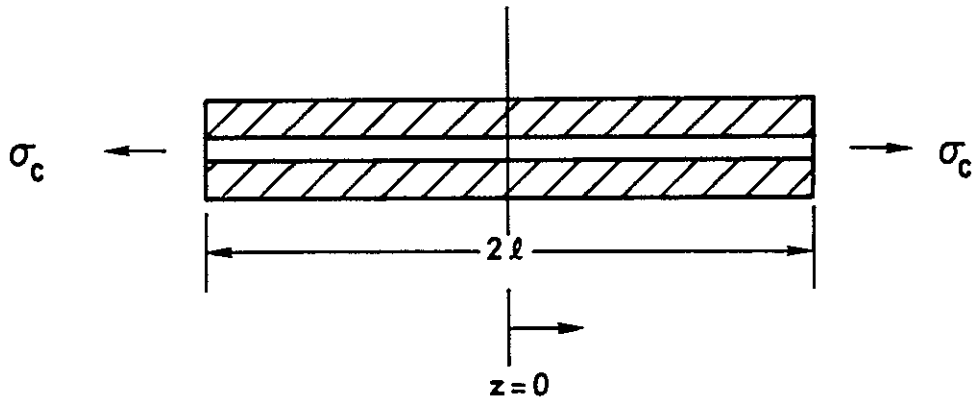

Figure 3.14 STATE OF APPLIED STRESS

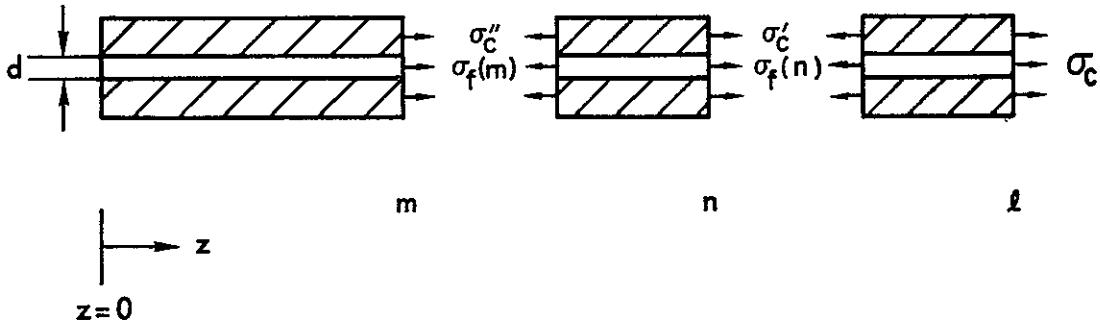

Figure 3 15 THE FIBER-MATRIX MODEL

$$\sigma_f(n) - \sigma_c = \gamma_1 \sigma_c \left[1 - \frac{\cosh a_1 n}{\cosh a_1 \ell}\right] \tag{3.4}$$

$$\sigma_c - \sigma_c' = \delta_1 \sigma_c \left[1 - \frac{\cosh a_1 n}{\cosh a_1 \ell}\right] \tag{3.5}$$

$$\sigma_f(m) - \sigma_f(n) = \left[\gamma_2 \sigma_c' - \delta_2 \sigma_f(n)\right] \left[1 - \frac{\cosh a_2 m}{\cosh a_2 n}\right] \tag{3.6}$$

$$\sigma_c' - \sigma_c'' = \left[\phi_2 \sigma_c' - \psi_2 \sigma_f(m)\right] \left[1 - \frac{\cosh a_2 m}{\cosh a_2 n}\right] \tag{3 7}$$

and

$$\sigma_{fb} - \sigma_f(m) = \left[\gamma_3 \sigma_c'' - \delta_3 \sigma_f(m)\right] \left[1 - \frac{1}{\cosh a_3 m}\right] \tag{3 8}$$

where

$$a = \frac{\lambda}{d}$$

and γ_1, δ_1, γ_2, δ_2, ϕ_2, ψ_2, γ_3, and δ_3 are related to the elastic constants of the fiber and matrix and are given in Appendix A together with the solution to the equations

σ_c was calculated at various test temperatures and is shown in Fig 3 16 where it is compared with the experimentally determined values Knowing σ_c and the distribution of shear stress along the fiber-matrix interface, the axial stress in the fiber $\sigma_f(z)$ at the point of composite failure was obtained

$$\sigma_f(z) = -\int \frac{4\tau}{d} dz + \text{constant}$$

The constant is determined from knowledge of the fiber stress at segment ends.

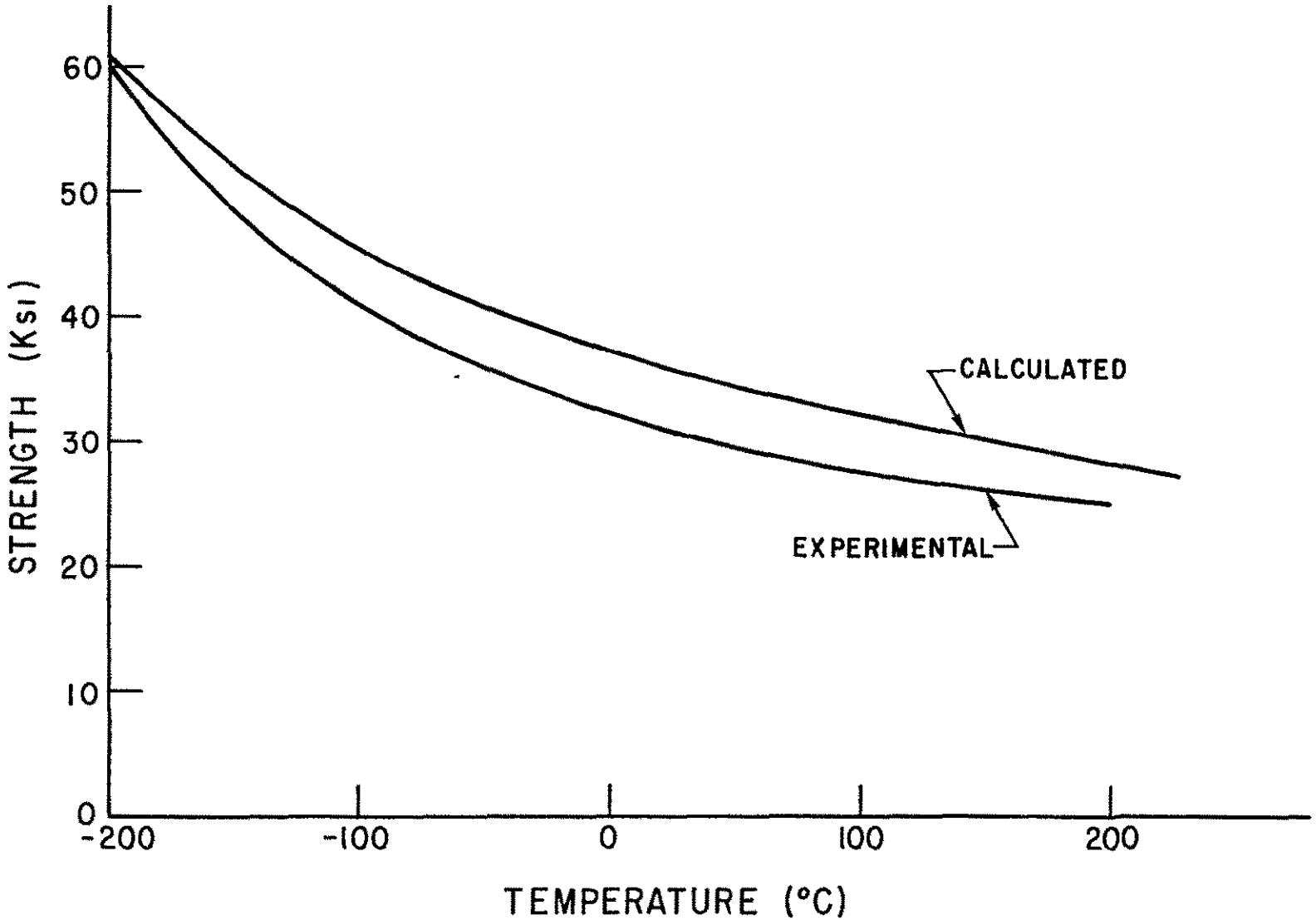

Figure 3 16 THE COMPARISON BETWEEN THE CALCULATED AND EXPERIMENTAL VALUES OF THE COMPOSITE LONGITUDINAL STRENGTH

$$\sigma_f(z) = \begin{cases} \sigma_c\left[1 + \gamma_1\left(1 - \dfrac{\cosh a_1 z}{\cosh a_1 \ell}\right)\right] & n \le z \le \ell \\ \sigma_f(n) + \left[\gamma_2\,\sigma_c' - \delta_2\sigma_f(n)\right]\left[1 - \dfrac{\cosh a_1 z}{\cosh a_1 n}\right] & m \le z \le n \\ \sigma_f(m) + \left[\gamma_3\,\sigma_c'' - \delta_3\sigma_f(m)\right]\left[1 - \dfrac{\cosh a_1 z}{\cosh a_1 m}\right] & 0 \le z \le m \end{cases}$$

(3 9)

Fig 3 17 shows the axial stress distribution in fiber at the point of composite failure (applied stress = σ_c) for different test temperatures

Discussion of the Model. (1) The model predicts the composite strength and its variation with the test temperature in terms of fiber strength and matrix properties Variations in the parameters γ_1, γ_2, δ_1, δ_2,.. that are related to matrix properties have the effect of increasing composite strength as the temperature is lowered. For example, calculations indicated that (see Appendix A) if the fiber strength were to remain unchanged, σ_c would have increased by only about 12% as the temperature was lowered from 25°C → -196°C Fig. 3.16 indicates that σ_c increases by about 70% as temperature drops from 25°C to -196°C Therefore the greater part of the change in strength is brought about by an increase in fiber strength with decreasing temperature

(2) The equilibrium equations for fiber and matrix in the different segments embody those for equilibrium of the segments themselves. Combining equations 3 4 and 3 5 one gets

$$\frac{\sigma_f(n) - \sigma_c}{\sigma_c - \sigma_c'} = \frac{\gamma_1}{\delta_1} = \frac{A_m}{A_f}$$

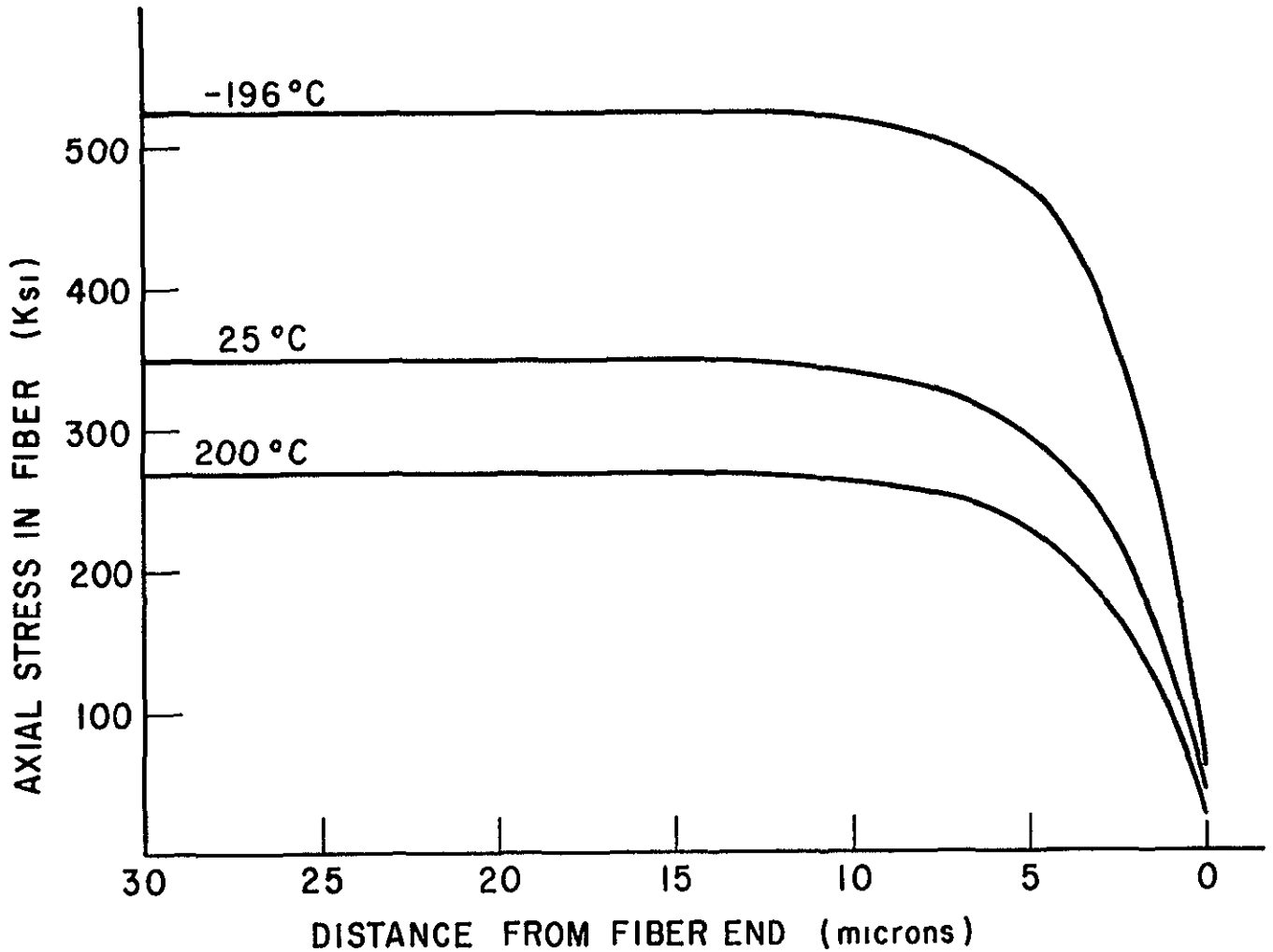

Figure 3.17 AXIAL STRESS DISTRIBUTION IN FIBER AT THE COMPOSITE FAILURE STRESS

which reduces to

$$\sigma_c = \sigma'_c A_m + \sigma_f(n) A_f/(A_m + A_f) \quad .$$

That is, the average stress acting across any cross section through the fiber-matrix model is equal to σ_c.

(3) Increase in fiber axial stress from σ_c at fiber end to its maximum value occurs over a relatively short distance The fibers in the composite possess a high aspect ratio and load transfer to the fiber will therefore occur over a distance that is relatively short as compared to fiber length 2ℓ

(4) As σ_f approaches a constant value (Fig 3 17) no load would further be transferred to the fiber and the matrix stress from there on would remain unchanged Such stresses have a level of 8,000 p s i at -196°C and 2,000 p s i at room temperature

The stress distribution in matrix is shown in Fig 3.18 and the lowest stress level in matrix is given as a function of temperature in Fig 3.19.

3 4 Behavior of Specimens Oriented Normal to Fiber Axis

Stress-strain curves of type E and F tensile specimens are shown in Figs 3 1b and 3 1c Increase in the test temperature has the effect of reducing both the yield stress and strain hardening rate of the material The behavior of a composite when loaded in a direction normal to its fibers is mainly determined by the matrix behavior and therefore, variation in the yield stress and strain hardening rate is ascribed to a similar change in matrix properties with temperature

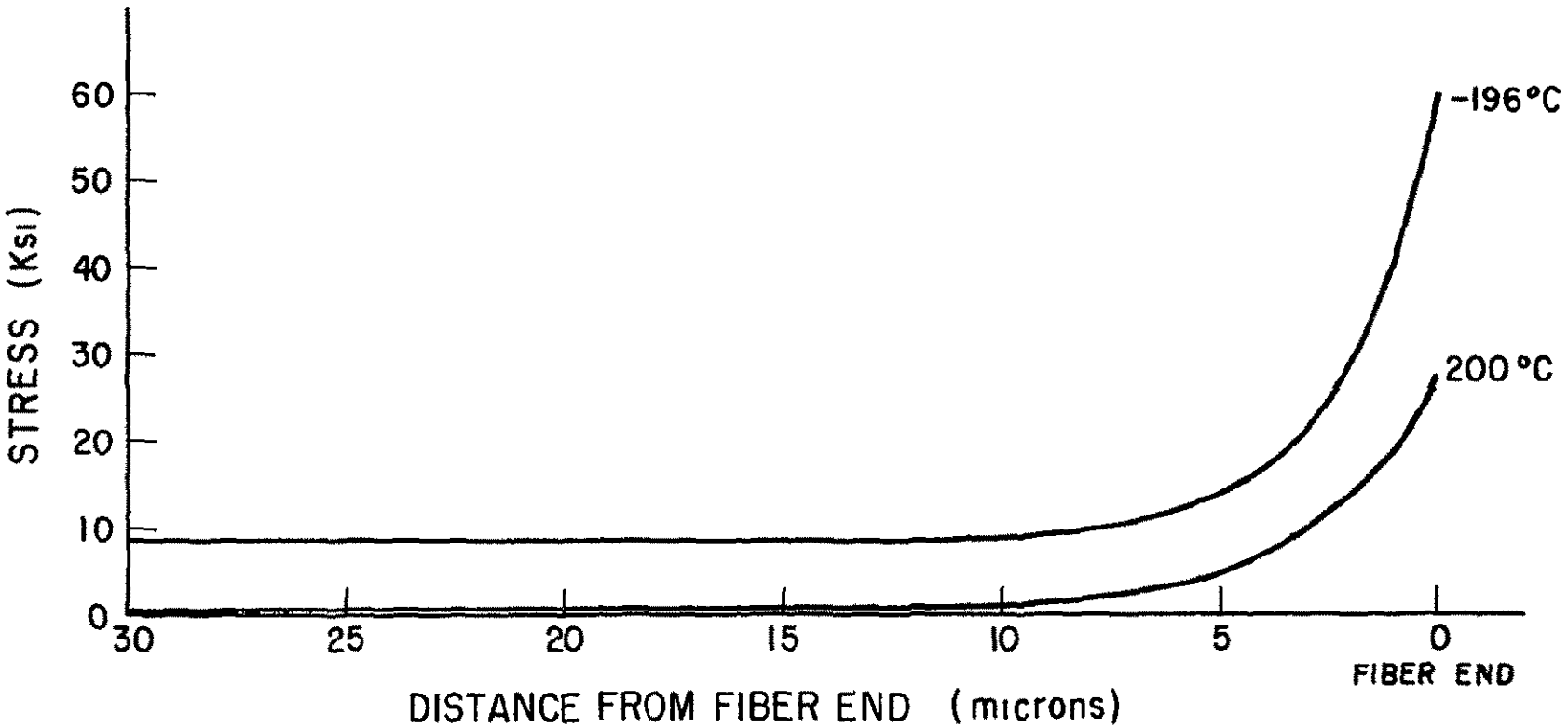

Figure 3.18 STRESS DISTRIBUTION IN MATRIX AT THE COMPOSITE FAILURE STRESS

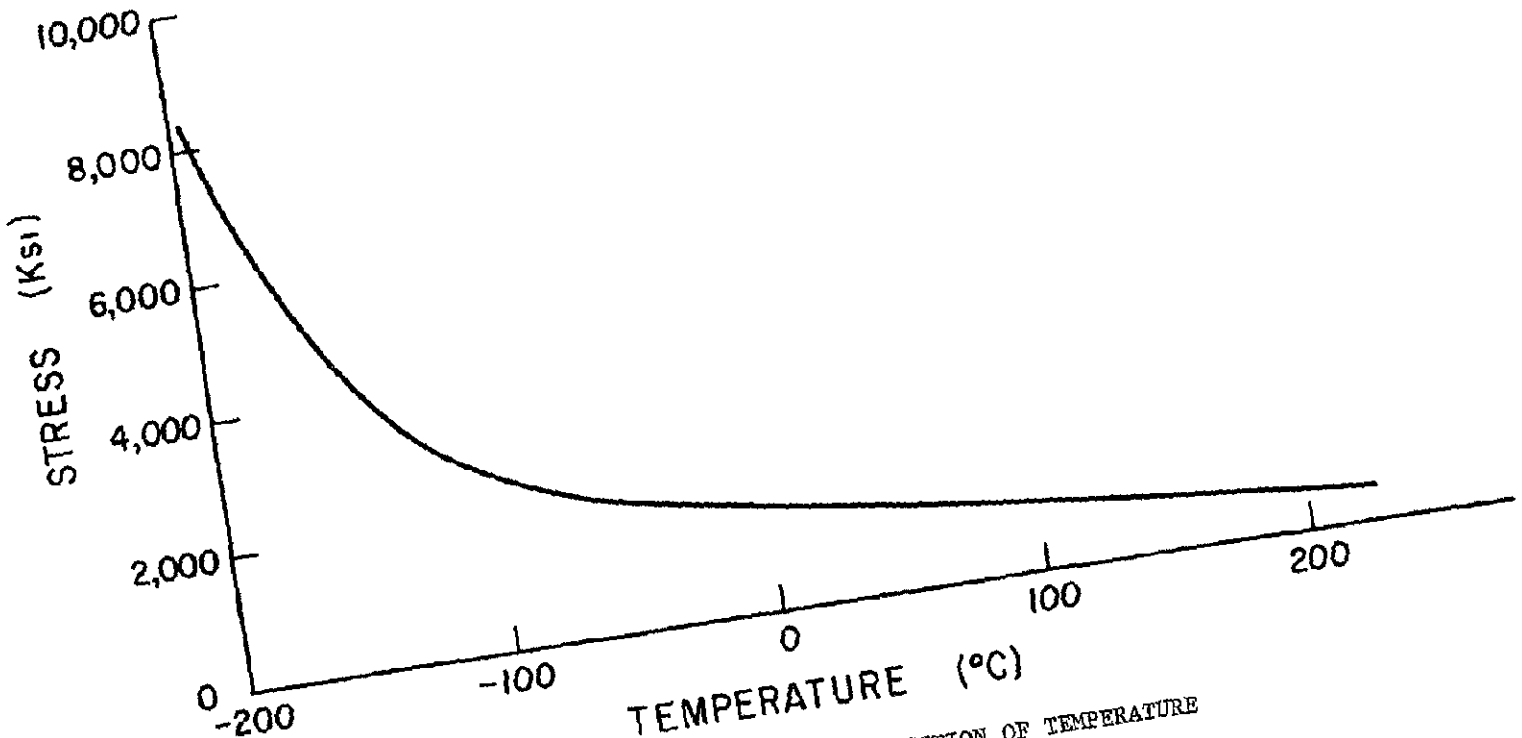

Figure 3.19 LOWEST STRESS IN MATRIX AS A FUNCTION OF TEMPERATURE

The increase in yield stress and $d\sigma/d\epsilon$ of the composite over those of the plain matrix is apparently due to the presence of the fibers which have the following effects

(1) Dispersion strengthening fibers could provide a barrier to dislocation motion in the matrix thus raising its initial flow stress σ_Y and its flow stress at later stages of deformation

(2) Plastic constraint fiber presence could lead to an increase in σ_Y as well as in $d\sigma/d\epsilon$ as they constrain plastic flow in matrix

3 4-1 Transverse Strength

The fracture mode as a function of orientation was studied[44] and it was shown that flow of the matrix was transverse to the fibers when aligned at 90° to stress axis Fracture surface at 90° is predominantly indicative of ductile fracture with a few broken fibers lying in the surface

Since the load is carried by the matrix and the matrix strength drops with temperature, the composite strength would do likewise The fibers have the effect of raising the strength of the matrix through several strengthening mechanisms that are believed to be operative

(1) Plastic constraint. Kelly and Davies[21] have suggested that a reasonable value to assume for the constrained matrix is about 15% higher than the tensile strength of the unconstrained matrix Experimentally determined strength values were found to be still higher.

(2) Loading the fibers: shear of the matrix along a plane that lies at an angle to the fibers will have a component of shear parallel to the fiber axis and therefore transfer load to the fibers

(3) Dispersion strengthening.

Variation in the ultimate strength (maximum load divided by the initial area of cross section of the specimen) with temperature for both E and F type specimens is shown in Fig. 3 20 It is noted that the strength of type F specimens is always a little higher than that of type E. The strength values obtained were quite consistent This was not the case for those obtained parallel to the growth direction where some scatter in the strength values was observed (Fig 3112)

Higher values of the strength of type F specimens as compared to those of type E are ascribed to a higher plastic constraint exerted by the fibers in a type F specimen

3 4-2 Tensile Ductility

The extent of slip and therefore deformation in loaded specimens is affected by fiber interference with the dislocation motion in the matrix If a slip plane is parallel to the fiber axis, which is the case for a type F specimen, slip would readily occur in a direction perpendicular to the fiber axis in such a plane (plane being near to 45° to fiber axis) If, on the otherhand, a slip plane is at an angle to the fiber axis, which is the case for a type E specimen, slip will be more difficult to initiate as compared to the first case It follows that slip in type F specimens will be more extensive as compared to that occurring in specimens of the type E orientation

This argument, which is represented schematically in Fig. 3 21, would lead to the conclusion that the tensile ductility would be higher for type F specimens than for type E A plot of percent elongation at failure as a function of the test temperature (Fig 3 5) indicates that

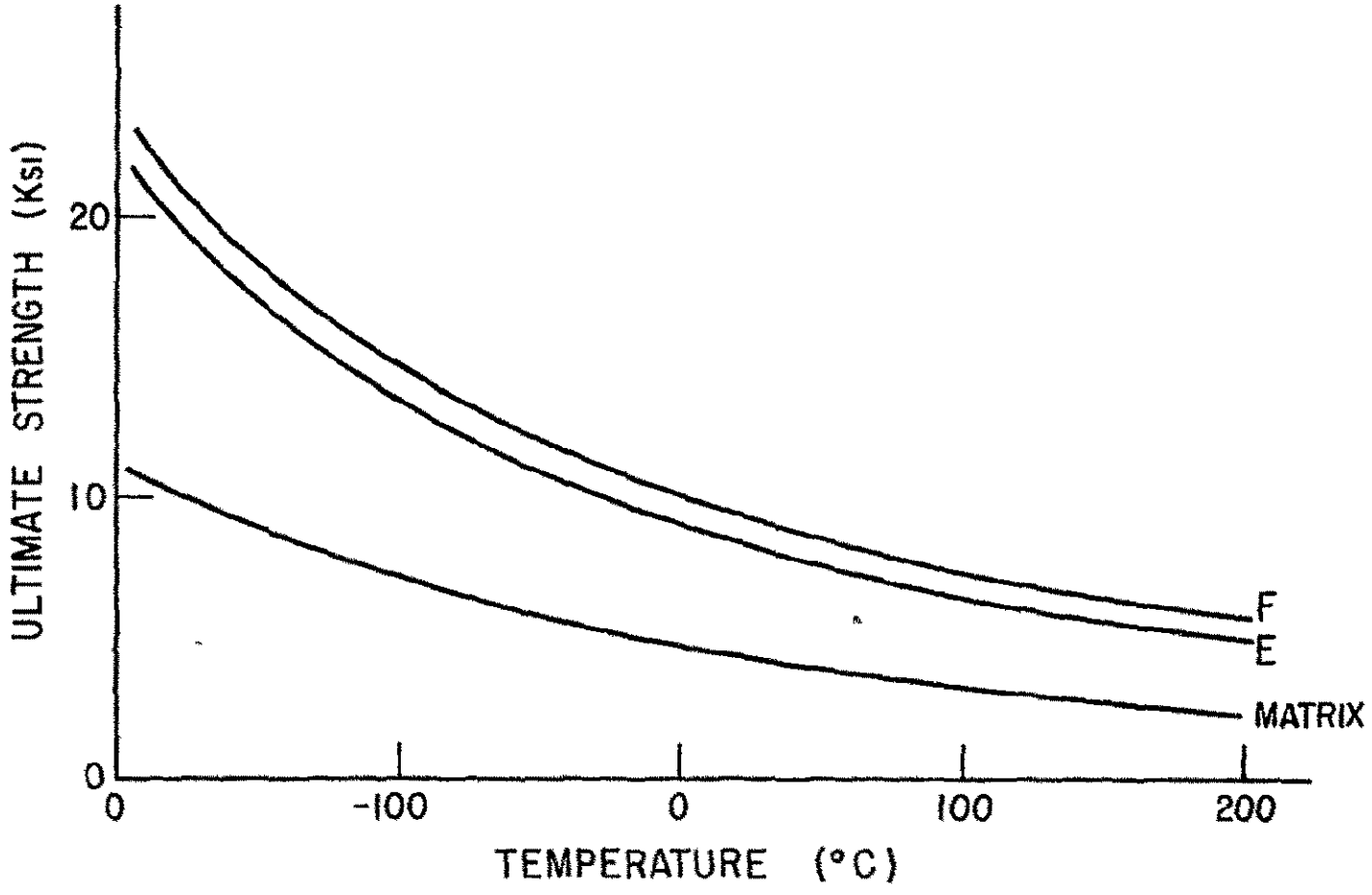

Figure 3.20 THE VARIATION OF THE COMPOSITE TRANSVERSE STRENGTH WITH TEMPERATURE

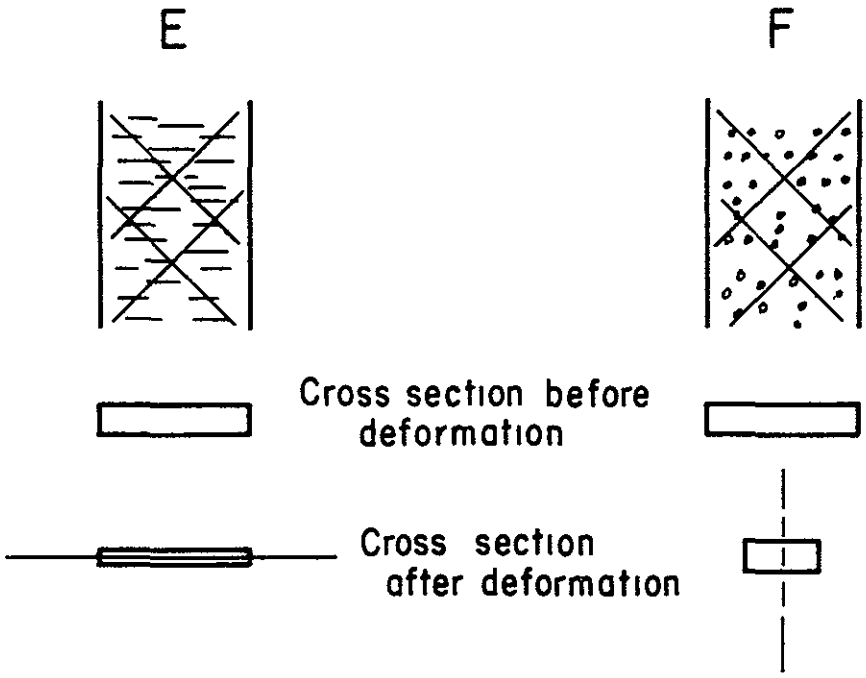

Figure 3 21 SCHEMATIC DRAWING OF THE DEFORMATION IN TYPE E AND F TENSILE SPECIMENS

the elongation at fracture is higher for type F orientation. It is also observed that the tensile ductility drops with temperature reaching a minimum and then starts to increase as the temperature is increased further

In contrast to type A specimens where no necking was observed on failure, considerable necking accompanied failure of the composite when loaded in the transverse direction However, a distinct difference in the direction of necking between type E and F was observed

The capacity of the composite for deformation in a direction parallel to fiber axis is limited by the elastic fiber strain which does not exceed a few percent (2 → 3%). Therefore, when the specimens are loaded in the transverse direction (normal to their fibers), the fibers would limit contraction of the material in the direction parallel to their axis As a result, when necking takes place, contraction in the material would be considerable only in the direction normal to the fibers The schematic diagram shown in Fig 3 21 indicates that the width of type F specimens is considerably reduced when the specimens neck down On the other hand, the thickness is shown to have undergone considerable reduction in type E specimens

Fig 3 22 shows the percentage reduction in area as a function of temperature for both type E and F specimens The pattern in the change of the ductility of the composite (in the transverse direction) with the test temperature follows that of the matrix (Fig 3 22)

The shape of the ductility-temperature curve of the matrix can be qualitatively explained by the methods of applied mechanics The strain hardening rate of the matrix increases with decreasing temperature and since higher rate of hardening by straining leads to greater uniform

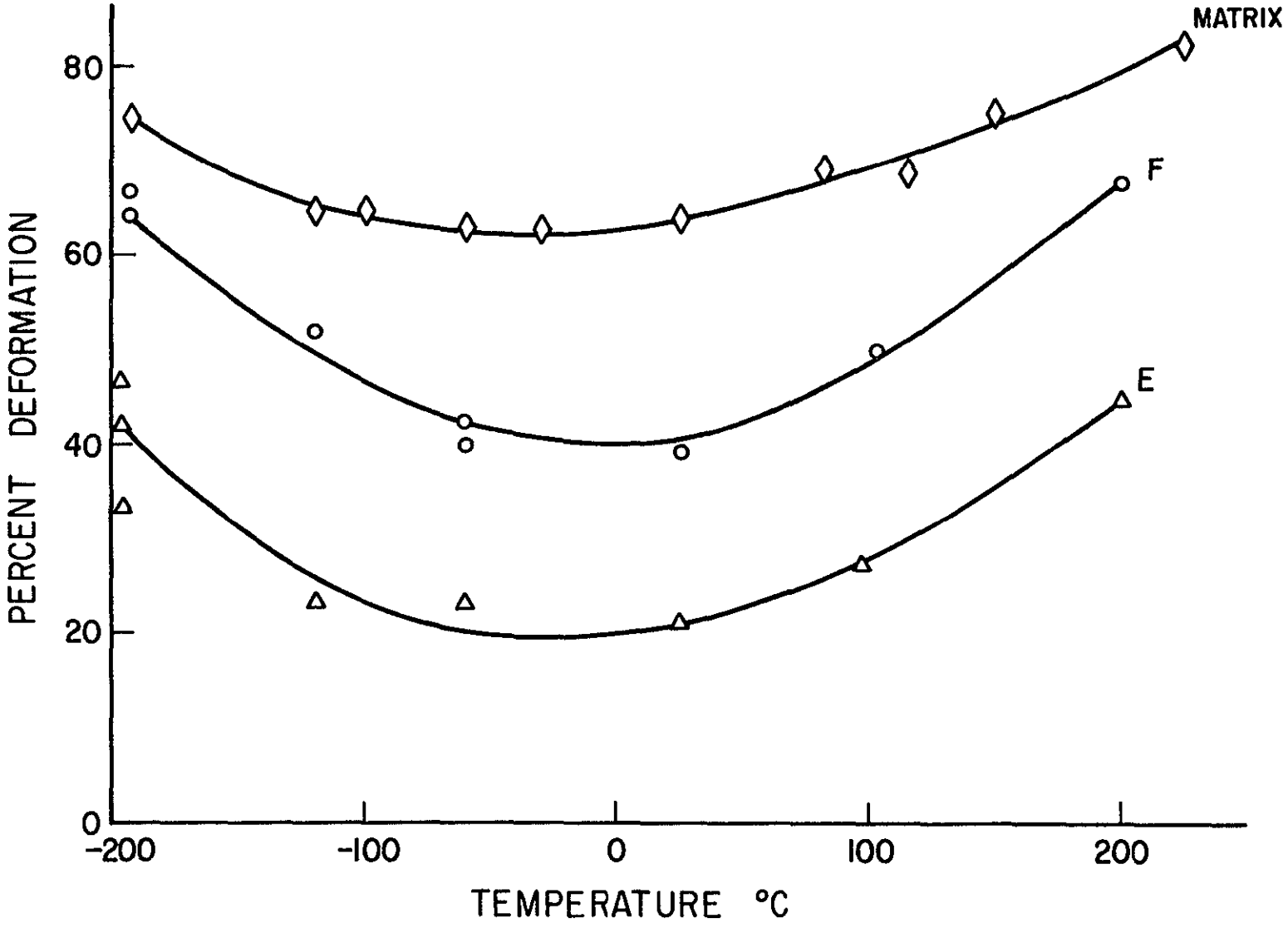

Figure 3 22 THE VARIATION IN MATRIX ELONGATION ON FRACTURE AND PERCENTAGE REDUCTION IN AREA OF TYPE E AND F SPECIMENS WITH THE TEST TEMPERATURE

elongation before necking begins, the ductility of the material will increase as the temperature is lowered Ductility is high when the strain hardening rate is high because localized deformation (i e , formation of a neck) will lead to hardening, this will retard further deformation from occurring in this region before final local failure, thus increasing the uniform elongation

At high temperature (beyond the point of minimum), the rate of hardening is close to zero and the strain hardening approach used in explaining the low temperature behavior cannot account for the high ductility observed at high temperatures An explanation of this high temperature trend can be given as follows The decrease in yield stress with the increase in temperature leads to a decrease in the strain rate according to the relation,

$$\dot{\epsilon} = (\frac{1}{K})\sigma^{(1/m)}$$

where K and m are material constants and m is known as the strain rate sensitivity exponent When localized plastic flow occurs in tensile specimens (i.e , a neck begins), the corresponding flow rate in that region will depend on the flow stress and therefore will decrease as the temperature is raised Thus the uniform elongation of such a material would be expected to be high at higher temperatures

CHAPTER IV

THE EFFECT OF FIBER ORIENTATION ON THE DISTRIBUTION OF PLASTIC DEFORMATION IN CHARPY SPECIMENS

The experiments described in this section were designed to study the effect of fiber orientation on the plastic deformation ahead of the notch in Charpy specimens. Specimens with their fibers oriented at different angles to the loading axis were deformed to various values of P (applied load) and the deformation patterns were revealed using the etching technique described in Chapter II The extent of plastic deformation was theoretically estimated as a function of the applied load (stress intensity factor) and then compared to the experimentally determined values

The plastic bend angle θ_p was correlated with the local plastic strains which were measured using microhardness values. The transverse strains expressed as the percentage contraction at the notch root were evaluated as a function of the applied load and bend angle The transverse strains ε_{zz}, determined for specimens with different fiber orientations, clearly demonstrate the anisotropic plastic behavior of the composite. The relationship between the longitudinal strain ε_{yy} and the transverse strain ε_{zz} was also determined

The fiber orientations A, E and F adopted for this study are shown in Fig 2.6 A number of specimens of each orientation were mechanically polished on one side to a 6μ diamond finish, chemically polished and then heat treated before they were deformed The specimens were subsequently etched to reveal the deformation patterns on the surface The etch pits produced in the deformed region gave the impression of a darker region on a macroscopic scale The fact that the initial dislocation density

was not high helps to distinguish between the deformed and undeformed regions Typical plastic zones developed on the surface of specimens with the type F and A orientations are depicted in Figures 4.1 and 4.2 respectively Figure 4.3 shows etch pits in an undeformed region of a type A specimen, where the density of the etch pits is low compared to that in the plastically deformed zone ahead of the notch

4.1 Deformation Patterns

4 1-1 Specimens with the Type F Fiber Orientation

The deformation patterns observed with the aid of the etching technique, Fig 4 4, show the development of the plastic zone below the notch on the specimen surface. The smallest amount of deformation detected was on the specimen deformed to P = 105 pounds when a zone of about 0 1 mm extended from the middle of the notch root It could thus be stated that the etching technique used is capable of revealing regions of plastic deformation of this size.

Further deformation to P $\simeq$ 140 pounds produces two hinges that extend from the corners of the notch root and which broaden and penetrate deeper into the ligament upon further deformation

High magnification photographs taken for the plastic zone, Figures 4.5 and 4.6, reveal the existence of two dislocation etch pit arrays Each array is apparently due to glide dislocations lying in a slip plane, so an array forms (lies on) the trace of a slip plane on the side surface of the specimen. The angle between the two arrays is therefore the angle between the traces of the two slip planes on the side surface of the specimen.

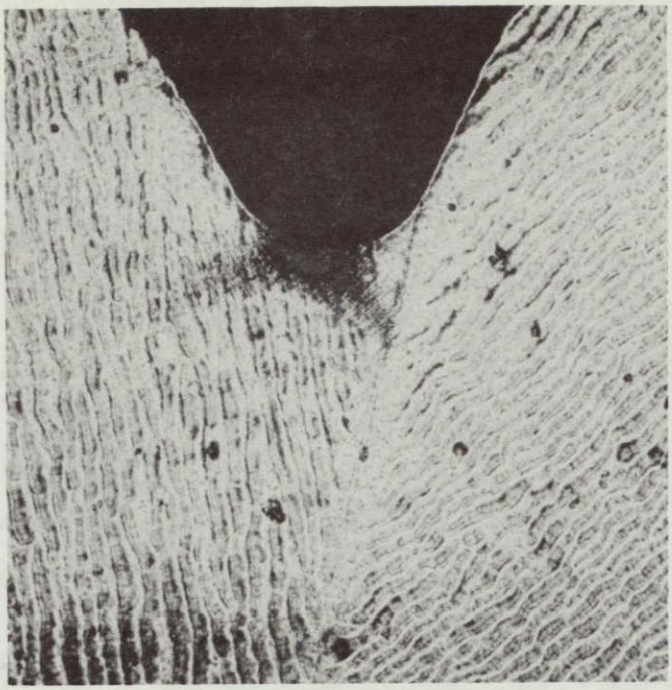

(a)

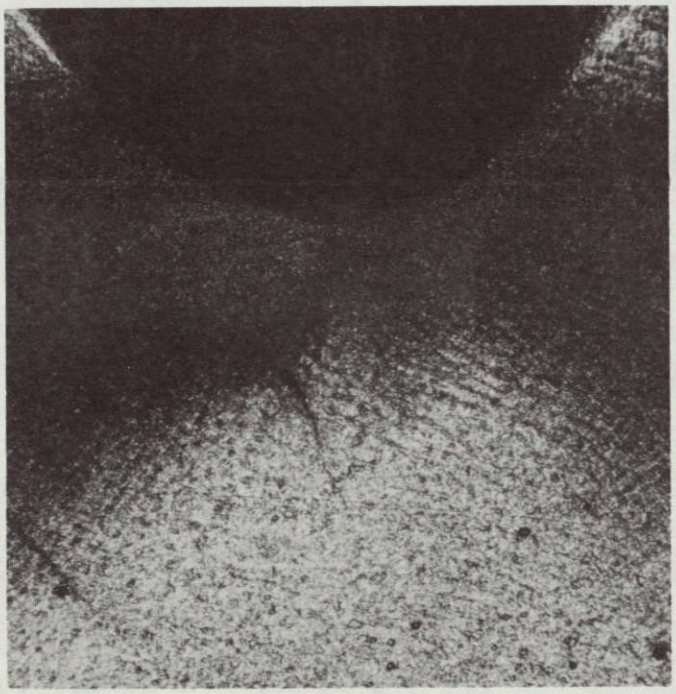

(b)

Figure 4.1 TYPICAL PLASTIC ZONES DEVELOPED ON THE SURFACE OF DEFORMED TYPE F SPECIMENS, MAGNIFICATION = 50X, (a) P = 160 lb., (b) P = 350 lb.

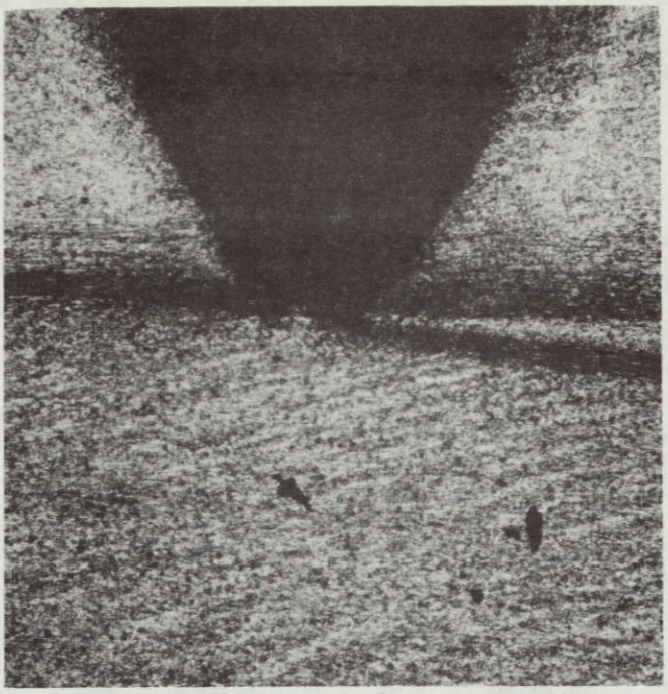

(a)

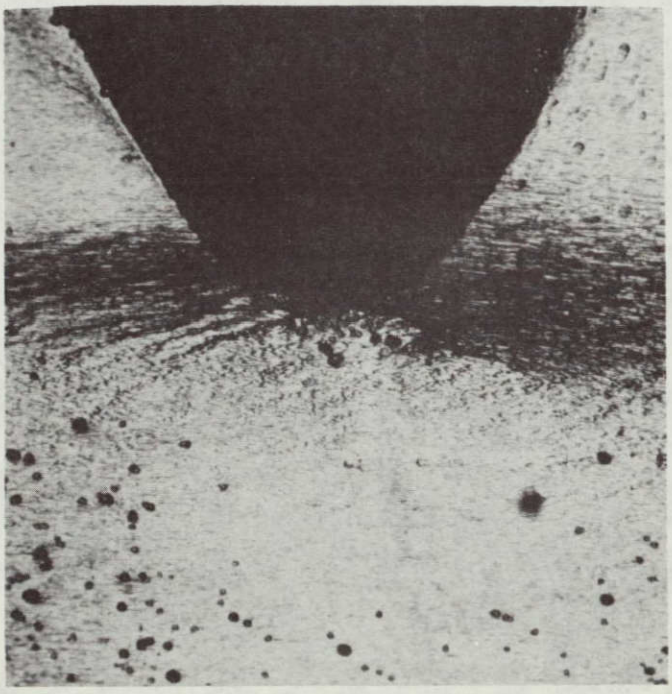

(b)

Figure 4.2 DEFORMATION PATTERNS DEVELOPED ON THE SURFACE OF DEFORMED TYPE A SPECIMENS, MAGNIFICATION = 50X, (a) P = 455 lb., (b) P = 505 lb.

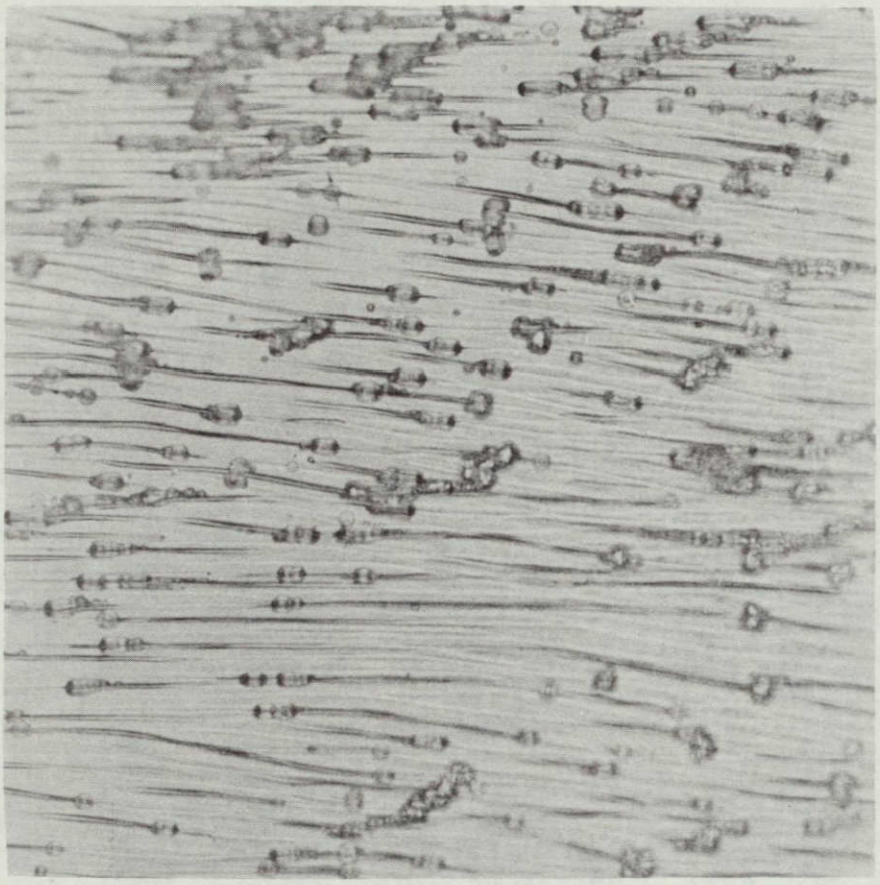

Figure 4.3 DISLOCATION ETCH-PITS IN AN UNDEFORMED REGION OF A TYPE A SPECIMEN, MAGNIFICATION = 800X.

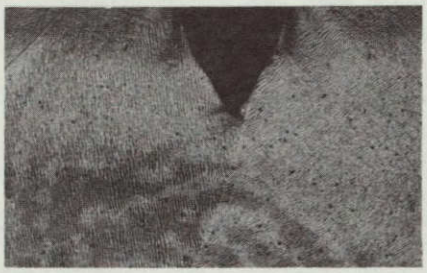

(a)

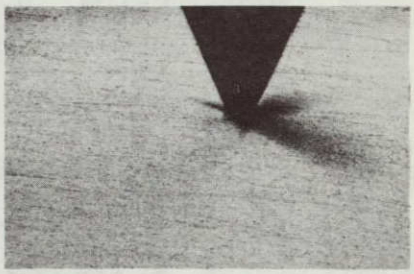

(b)

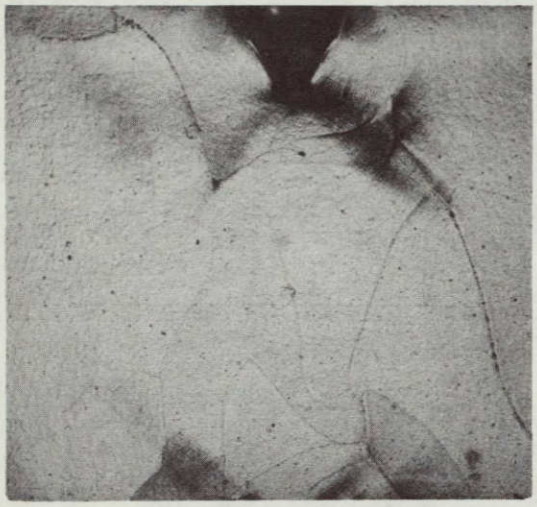

(c)

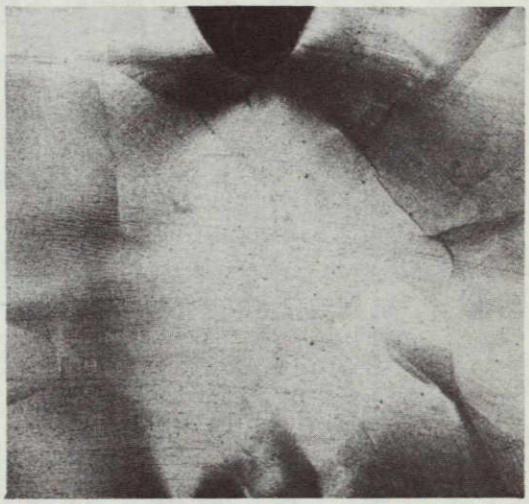

(d)

Figure 4.4 DEVELOPMENT OF THE PLASTIC ZONE ON THE SURFACE OF TYPE F SPECIMENS, MAGNIFICATION = 7X, (a) P = 160 lb., (b) P = 200 lb., (c) P = 210 lb., (d) P = 350 lb.

Figure 4.5 DISLOCATION ETCH-PIT ARRAYS IN THE PLASTIC ZONE OF A DEFORMED TYPE F SPECIMEN, MAGNIFICATION = 800X.

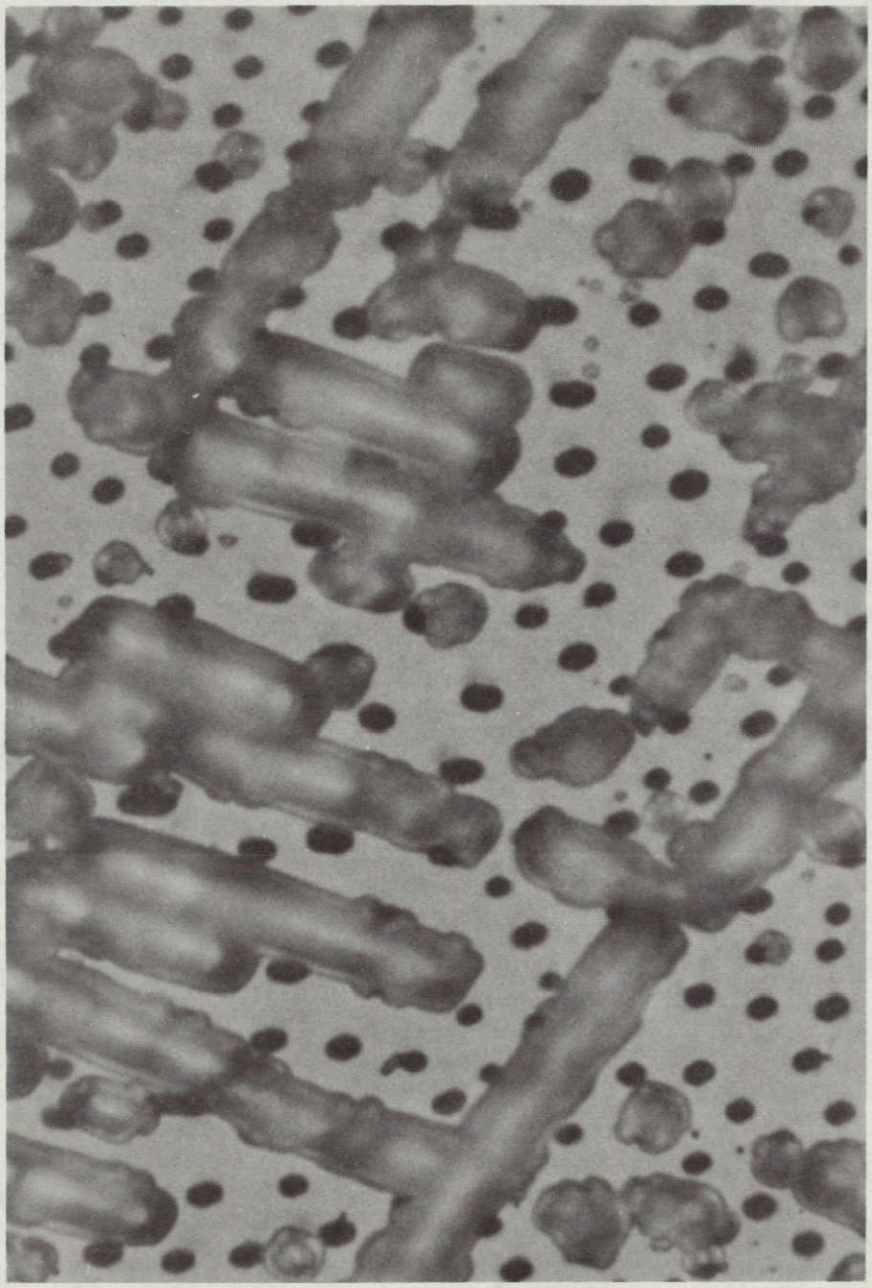

Figure 4.6 ETCH-PIT ARRAYS AT A MAGNIFICATION OF 2560X.

Angle between slip plane traces. It was found by Lemkey, Hertzberg and Ford[38] that a single unique crystallographic relationship exists between the Al and Al_3Ni phases formed during the unidirectional solidification of the high purity Al - Al_3Ni eutectic alloy. As a result, the <110> direction in the Al matrix will tend to be parallel to the growth direction. Therefore, in type F specimens the side surface of the specimen should correspond to a {110} type plane.

The slip planes and their traces on the specimen side surface can be found for a given orientation of the stress axis (stress axis lies in the specimen side surface). Figure 4.7 shows a general case where the stress axis is at an angle to the [110] direction. The orientation of the stress axis is in the standard triangle, Figures 4.7 and 4.8. For such an orientation, the behavior of Al would be for slip to occur on the primary slip system $(11\bar{1})$ [101]. As deformation proceeds, slip would also occur on the conjugate system $(1\bar{1}1)$ [110]. The traces of the slip planes $(11\bar{1})$ and $(1\bar{1}1)$ on the side surface $(1\bar{1}0)$ are [110] and [112] respectively.

The measured angle between the two etch pit arrays varies from 60° to 75° as compared to 55° which is the angle between the [110] and [112] directions. Deviation of the specimen side surface from exact parallelism with the $(1\bar{1}0)$ plane leads to an angle between the traces on the side surface that is different from that between the traces on the $(1\bar{1}0)$ plane namely the [110] and [112] directions.

The etch pit density was found to increase as the deformation proceeds (Fig. 4.9) and the etch pits were not particularly concentrated around the fibers.

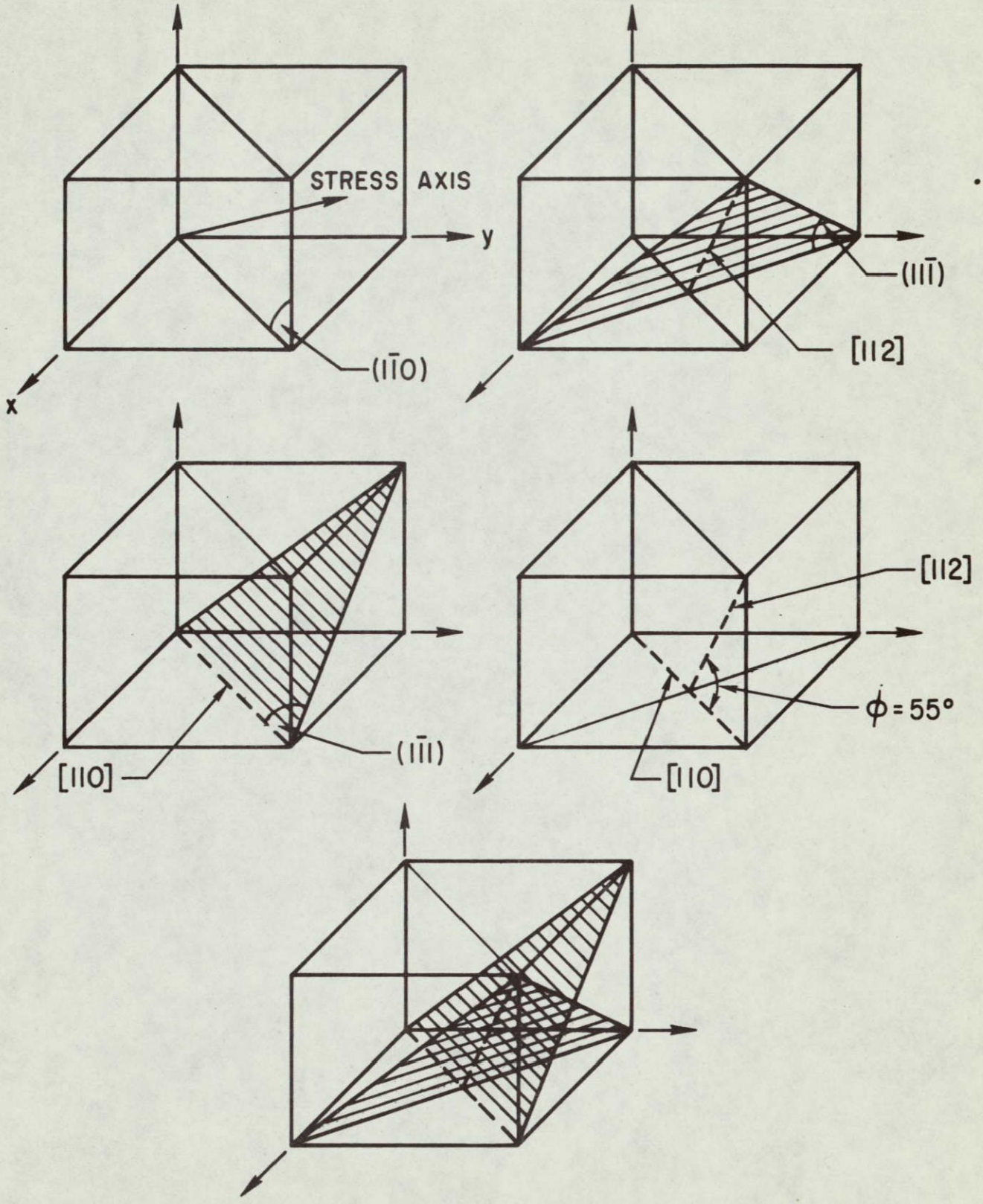

Figure 4.7 SLIP PLANES AND THEIR TRACES ON THE SPECIMEN SIDE SURFACE

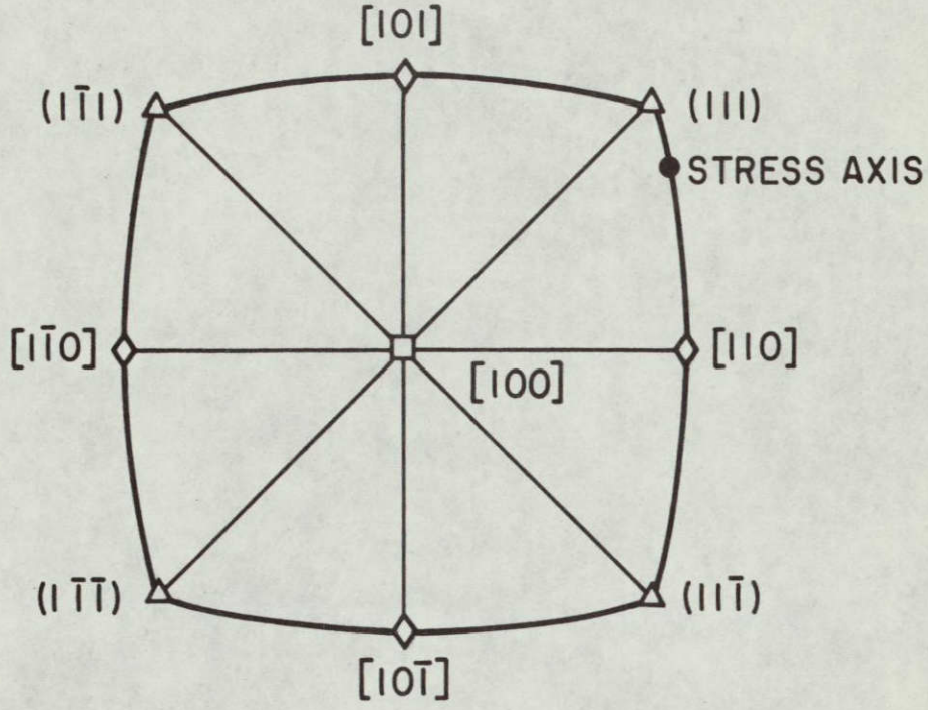

Figure 4.8 STEREOGRAPHIC PROJECTION OF THE SLIP PLANES

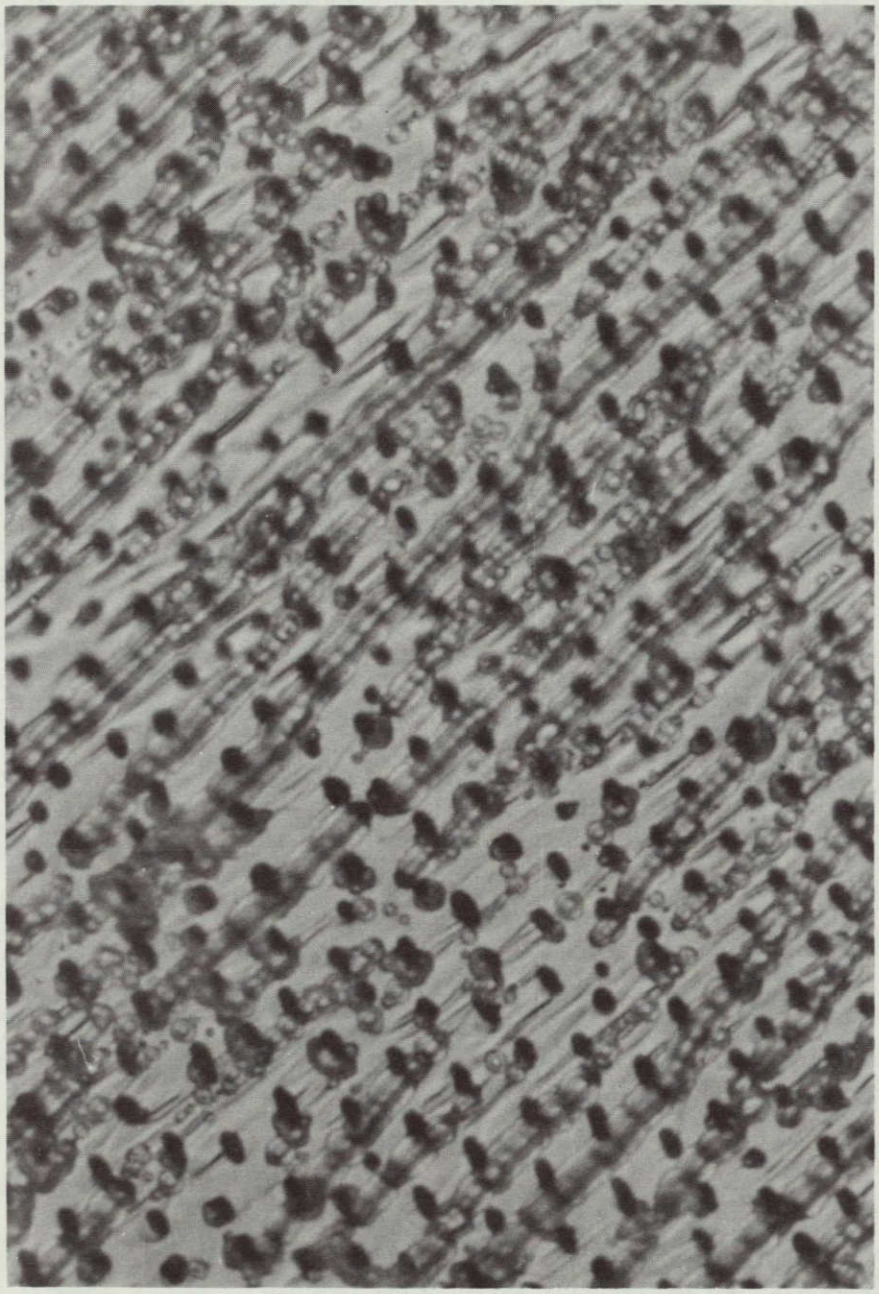

Figure 4.9 DISLOCATION ETCH-PITS IN A TYPE F SPECIMEN LOADED TO P = 250 lb., MAGNIFICATION = 2500X.

4.1-2 Specimens with the Type A Orientation

The deformation patterns observed with the aid of the etching technique, Fig. 4.10, show the development of the plastic zones below the notch root on the side surface of the specimens. The smallest amount of deformation detected was on the specimen deformed to P = 165 when a zone of about 0.04 mm extended from the middle of the notch root. With further increase of the applied load, the plastic zone was found to penetrate a little deeper into the specimen ligament and to extend in the lateral direction. Further deformation $P \tilde{=} 425$ causes a crack to initiate right at the notch root. The plastic zone was found to extend a distance 0.18 mm in the plane of the notch, before the crack started to develop.

High magnification photographs of the plastic zones, Fig. 4.11, reveal the distribution of the dislocation etch pits. They tend to have a higher density at fiber-matrix interface thus indicating considerable interaction of the fibers with dislocations in the matrix.

4.1-3 Specimens with the Type E Orientation

Macrographs of deformed specimens with the type E fiber orientation were obtained under indirect lighting. As a result, the elastic (undeformed) regions appear dark because light is reflected away by the chemically polished surface. The yielded zones appear white because the irregular surface caused by the high density of dislocation etch pits reflects light into the microscope. Figure 4.12 shows the deformation pattern developed on the surface of a type E specimen. The fibers in type E are oriented in a way that impedes slip in the matrix. Therefore, plastic flow in the matrix is not as extensive as in type F specimens

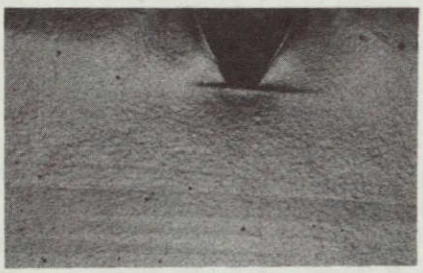

(a)

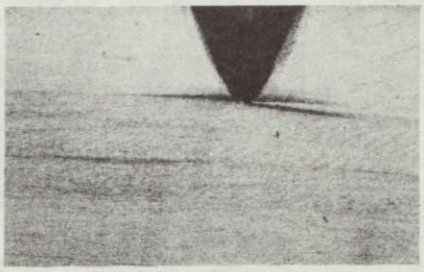

(b)

(c)

(d)

Figure 4.10 DEVELOPMENT OF THE PLASTIC ZONE ON THE SURFACE OF TYPE A SPECIMENS, MAGNIFICATION = 7X, (a) P = 355 lb., (b) P = 455 lb., (c) P = 505 lb., (d) P = 560 lb.

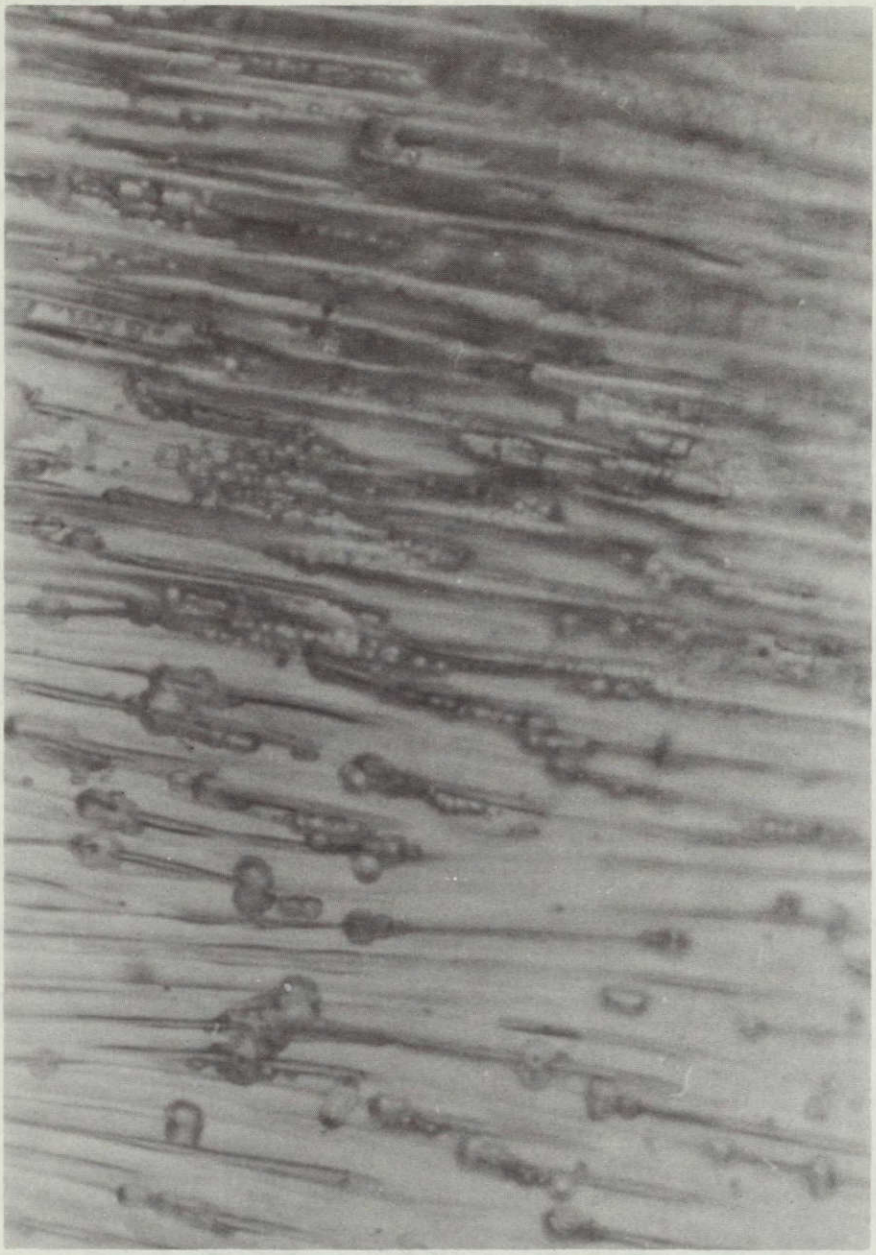

Figure 4.11 DISLOCATION ETCH-PITS IN A DEFORMED TYPE A SPECIMEN, MAGNIFICATION = 1600X.

where slip occurred with little interference from the fibers. Figure 4.13 shows the dislocation etch pits in the plastically deformed zone of a type E specimen.

4.2 Plastic Zone Size

The extension of the plastic zone was measured from the notch root in the plane of the notch. The variation of the plastic zone size with the applied load P is represented in the form of the graph R versus P in Fig. 4.14 for type F orientation and in Fig. 4.15 for type A.

Extrapolating the relation between R and P to zero values of R gives the applied load P_{LY} required to initiate slip at the notch root. P_{LY} was found to be 50 pounds for type F (Fig. 4.14) and 75 pounds for type A (Fig. 4.15).

4.2-1 Elastic Stress Concentration Factor

A notched specimen remains completely elastic until the applied nominal stress σ_N times the elastic stress concentration factor K_σ could cause plastic flow in the matrix at the notch root (x = 0, Fig. 4.16). That is plastic flow in the matrix begins when

$$\sigma_N = \frac{\sigma_{yy}}{K_\sigma} = \frac{\sigma_Y}{K_\sigma}$$

where σ_Y is the uniaxial stress to be applied to initiate plastic flow in the matrix.

In three point bending the nominal stress at the notch tip is given by the relation

$$\sigma_N = \frac{6M}{ta^2}$$

where

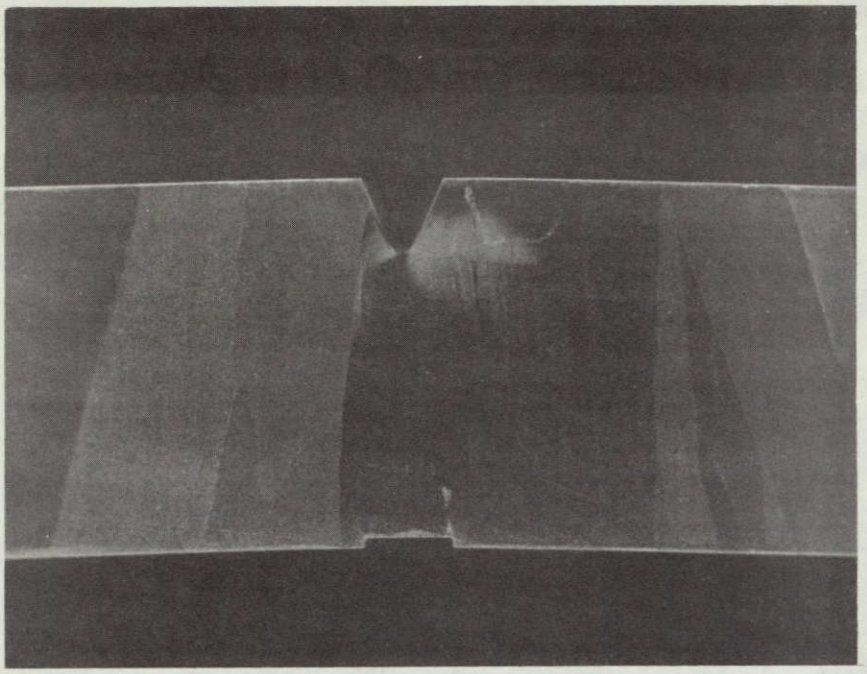

Figure 4.12 DEFORMATION PATTERN DEVELOPED ON THE SURFACE OF A TYPE E SPECIMEN LOADED TO P = 250 lb., MAGNIFICATION = 4.8X.

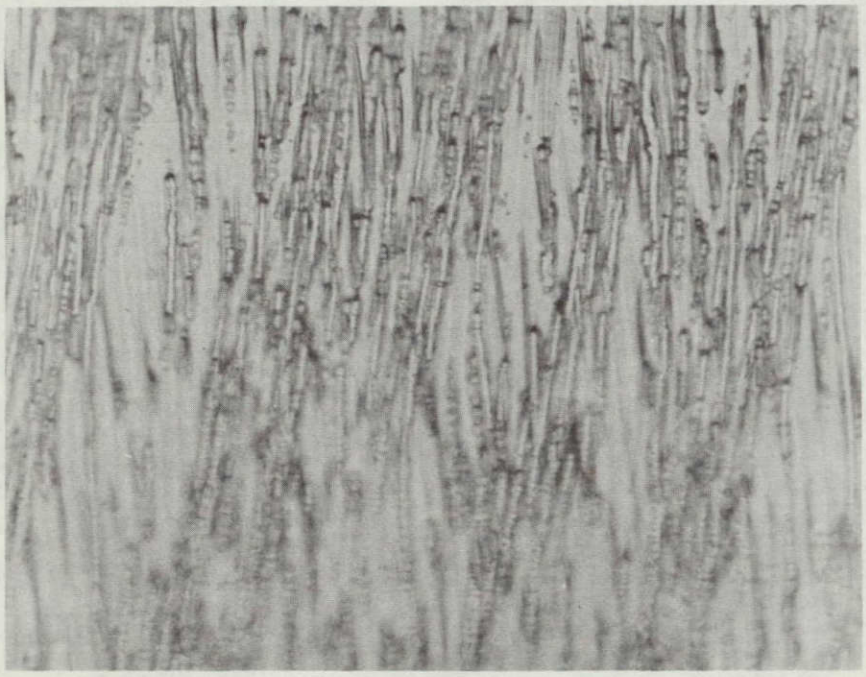

Figure 4.13 ETCH-PITS IN THE PLASTIC ZONE OF A TYPE E SPECIMEN LOADED TO P = 250 lb., MAGNIFICATION = 800X.

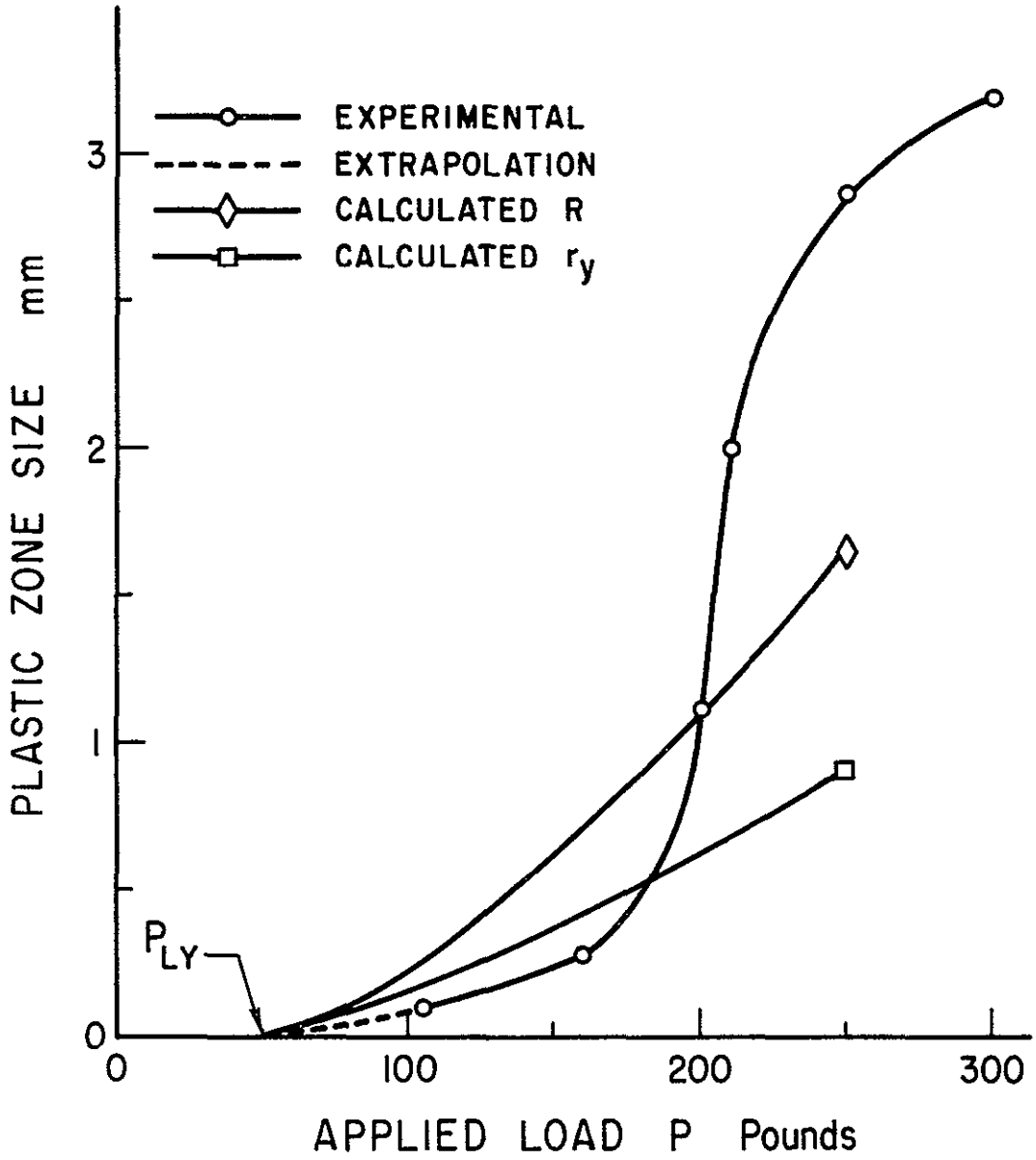

Figure 4.14 THE EFFECT OF APPLIED LOAD ON THE GROWTH OF THE PLASTIC ZONE IN TYPE F SPECIMENS

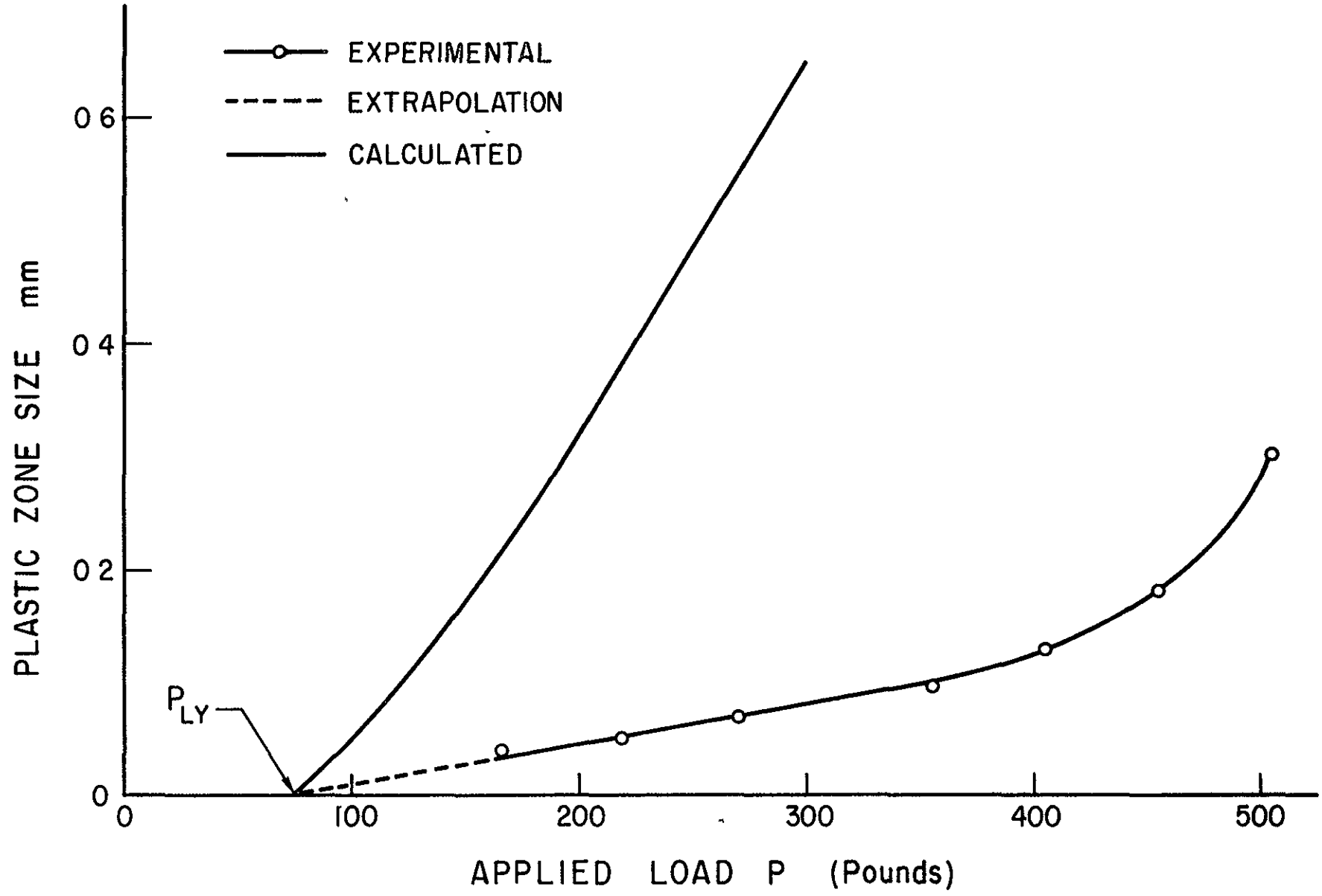

Figure 4 15 THE EFFECT OF APPLIED LOAD ON THE GROWTH OF THE PLASTIC ZONE IN TYPE A SPECIMENS

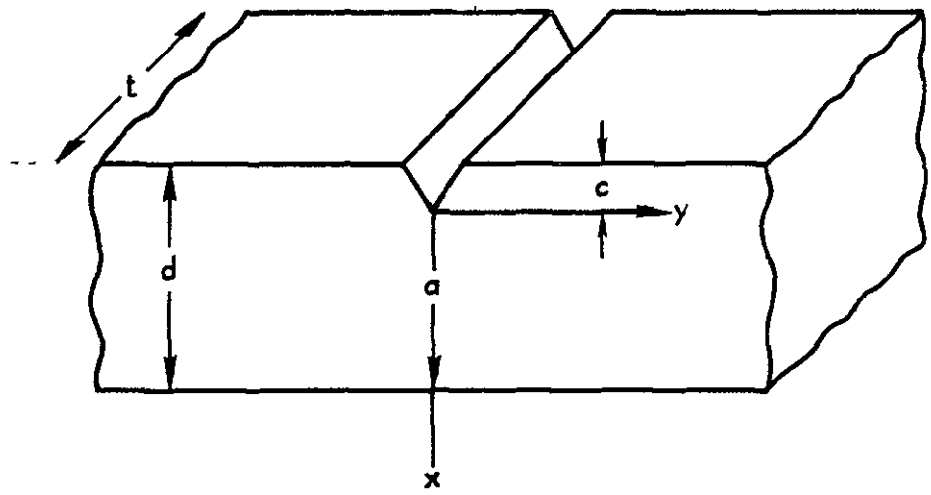

Figure 4 16 COORDINATE SYSTEM USED TO DEFINE THE STRESS FIELD σ_{yy} AHEAD OF THE NOTCH IN A NOTCHED BAR

M = applied bending moment = $\frac{PL}{4}$ (L = specimen span)

t = specimen thickness

a = depth of the notched cross section.

The assumption that the material is elastically isotropic is made throughout this work. This assumption is justified since the fibers (10% by volume) will have only a small effect on the elastic constants of the matrix. However, the effect is slightly greater in the longitudinal direction as compared to that in the transverse direction. Elastic anisotropy of the Al matrix is not taken into consideration.

K_σ is determined by the geometry of the notch (depth d, root radius ρ, flank angle ω, ligament depth a and the ratio c/d). Neuber[51] devised a simple geometrical procedure to calculate K_σ by averaging the stress concentration factors for both a shallow and deep notch. He obtained a series of Nomograms for determining K_σ for any given notch geometry. For the Charpy geometry K_σ was found to be equal to 4.2.[52] The relationship between P and σ_{yy} at the notch root would then be

$$\sigma_{yy} = K_\sigma \sigma_N = K_\sigma \frac{6M}{ta^2} , \qquad (4.1)$$

or

$$P = 3.9 \times 10^{-3} \sigma_{yy}$$ [52,53]

where P in pounds and σ_{yy} in p s i.

For local yielding to occur, $\sigma_{yy} = \sigma_Y$.

Therefore,

$$P_{LY} = 3.9 \times 10^{-3} \sigma_Y \qquad (4.2)$$

The value of σ_Y obtained from equation (4.2) is 12,800 p s.i. for specimens with the type F orientation (P_{LY} = 50), and 19,200 for type A orientation (P_{LY} = 75). These values are compared to 10,000 and 15,000 respectively which are the values obtained from the tensile tests described in Chapter III σ_Y as obtained from the stress-strain curve for the type A orientation corresponds to the point on the curve where the slope changes due to plastic flow of the matrix

4.3 Theoretical Estimation of the Variation of R withP

The longitudinal stress σ_{yy} is maximum at the notch tip (x = 0) and is given by

$$\sigma_{yy} = K_\sigma \quad \sigma_N$$

Ahead of the root for x>o, σ_{yy} decreases with x Weiss[54] has shown that

$$\sigma_{yy}(x) = K_\sigma \ \sigma_N \sqrt{\frac{\rho}{\rho+4x}} \quad 0 \leq x < \frac{\rho}{4}(k_\sigma^2 - 1) \tag{4.3}$$

In bending equation (4.3) has to be modified to account for the fact that the stress gradient is steeper since σ_N itself decreases linearly with x That is[55]

$$\sigma_N(x) = \frac{2\sigma_N}{a}\left(\frac{a}{2} - x\right) \tag{4 4}$$

where σ_N is the nominal stress at notch root and $\sigma_N(x)$ is the nominal stress at a distance x ahead of the notch tip. Substituting for $\sigma_N(x)$ in equation (4.3), σ_{yy} will take the form

$$\sigma_{yy}(x) = K_\sigma \frac{2\sigma_N}{a}\left(\frac{a}{2} - x\right)\sqrt{\frac{\rho}{\rho+4x}} \tag{4.5}$$

$$K_\sigma \quad \sigma_N = \frac{1000P}{3.9}$$

Therefore,

$$\sigma_{yy}(x) = \frac{2000P}{3.9a}\left(\frac{a}{2} - x\right)\sqrt{\frac{\rho}{\rho+4x}}$$

Putting in the numerical values for a and ρ for the Charpy geometry, σ_{yy} eventually takes the form

$$\sigma_{yy}(x) = 1627\ 5P\ (0.1576 - x)\sqrt{\frac{0.01}{0.01+4x}}\ , \qquad (4.6)$$

which gives the elastic stress distribution ahead of the notch for an applied load P. This equation indicates that the elastic stress in the vicinity of the notch can be very large Localized plastic deformation occurs when the appropriate yield criterion is satisfied and a plastic zone is created near the notch tip.[1] Spread of the yield zones with increasing the applied load P depends on the mode of deformation Assuming plane stress conditions on the free surface of the specimen, the zone will extend a distance r_y, in the plane of the notch, which, for an applied load P, is obtained by putting σ_{yy} equal to σ_Y at $x = r_y$. That is r_y is given by

$$\sigma_Y = 1627.5P\ (0\ 1576 - r_y)\sqrt{\frac{0\ 01}{0.01+4r_y}}$$

Solving for r_y, we get

$$r_y^2 - r_y\left[0.3152 + 9\ 936P_{LY}^2\frac{1}{P^2}\right] + \left[0.02484 - 0.02484P_{LY}^2\frac{1}{P^2}\right] = 0$$

(4 7)

The variation of r_y with the applied load P is represented in Figures 4.14 and 4.15 together with the experimentally measured values of the plastic zone size

For the type F orientation the stresses σ_{yy} could be assumed constant and equal to σ_Y inside the plastic zone To take up the load that was carried by the elastic material in the region $o<r<r_y$, the plastic zone has to extend to a distance R such that[1]

$$\sigma_Y R \simeq \int_0^{r_y} \sigma_{yy}(x)\, dx$$

which gives R as

$$R \simeq \int_0^{r_y} K\frac{2\sigma_N}{\sigma\sqrt{a}}\left(\frac{a}{2} - x\right)\sqrt{\frac{\rho}{\rho+4x}}\; dx/\sigma_Y \qquad (4\ 8)$$

Performing the integration and substituting in the numerical values for the constants yield R corresponding to an applied load P. That is,

$$R = 0.635\,\frac{P}{P_{LY}}\,[0\ 078\ (\sqrt{0\ 01+4r_y} - 0.1)$$

$$+ 0\ 083\{(0\ 01 - 2r_y)\sqrt{0\ 01+4r_y} - 0.001\}] \qquad (4\ 9)$$

The variation of R with P as obtained from equation (4 9) is represented in Fig. 4.14. The figure shows a gradual increase in R with the applied load. However, the values of R predicted from the analysis are higher than the experimentally measured values As the applied load is increased, R increases at a faster rate and as the point of plastic instability is reached, a sudden increase in R is observed. This sudden

increase in R with P is not predicted by the analysis since it breaks down and is no longer valid beyond the point of plastic instability.

In mild steel the general yield load P_{GY} can be obtained from the load-deflection curve due to sharp yielding in this material P_{GY} was found to coincide with the sudden spread of plastic hinges across the specimen ligament from the root of the notch to the compression side [56] For specimens with the type F orientation, the load corresponding to the sudden increase in R could be taken as the general yield load P_{GY}. From Fig. 4 14 P_{GY} = 200 pounds. The relation between R and P can then be replotted as R versus P/P_{GY} to give curves similar to those shown in Fig 4 14

Figures 4.14 and 4.15 indicate that the development of the plastic zone with P in type A is very limited as compared to type F This is due to the following reasons:

(1) σ_Y, which is the value σ_{yy} should achieve for first slip to take place at the notch root, is higher for type A specimens than it is for type F. Extrapolating the relation between the plastic zone size and the applied load gives a value of P = 75 pounds as the load required for first slip to occur

(2) Plastic flow in the matrix results in effective load transfer to the fibers The stress σ_{yy} inside the plastic zone would, therefore, continue to rise beyond σ_Y as deformation proceeds. As a result, the plastic zone can take up the load that was carried by the elastic material, ahead of the notch, by raising the stress levels σ_{yy} within the zone through effective loading of the fibers, rather than by extending the zone itself

The values of r_y, as obtained for type A specimens, are much higher than the experimentally measured values (Fig. 4 16), indicating that the deformation is more constrained than the analysis assumes.

Dependence of R on the Stress Intensity Factor Gross has determined the relationship between the stress intensity factor K_I and the applied moment M and found[57,58]

$$K_I = \frac{4M}{d^{3/2}} [31.7(\frac{c}{d}) - 64\ 8(\frac{c}{d})^2 + 211(\frac{c}{d})^3]$$

Substituting for M, d and c/d yields the relation between K_I and P That is,

$$K_I = 35\ 3\ \ P \tag{4.10}$$

Therefore, the relationship between R and K_I will be similar to that between R and P.

4.4 Angular Dependence of the Plastic Zone Extension

The elastic stress distribution in the neighborhood of elliptical holes and hyperbolic notches has been obtained by Creager and Paris.[59] For the coordinate system shown in Fig 4 17, the expressions for σ_{xx}, σ_{yy} and τ_{xy} under conditions of plane stress in the opening mode are as follows

$$\sigma_{xx} = \frac{K_I}{\sqrt{2\pi r}} \cos\frac{\theta}{2} [1 - \sin\frac{\theta}{2} \sin\frac{3}{2}\theta] - \frac{K_I}{\sqrt{2\pi r}} \frac{\rho}{2r} \cos\frac{3}{2}\theta$$

$$\sigma_{yy} = \frac{K_I}{\sqrt{2\pi r}} \cos\frac{\theta}{2} [1 + \sin\frac{\theta}{2} \sin\frac{3}{2}\theta] + \frac{K_I}{\sqrt{2\pi r}} \frac{\rho}{2r} \cos\frac{3}{2}\theta$$

$$\tau_{xy} = \frac{K_I}{\sqrt{2\pi r}} \sin\frac{\theta}{2} \cos\frac{\theta}{2} \cos\frac{3}{2}\theta - \frac{K_I}{\sqrt{2\pi r}} \frac{\rho}{2r} \sin\frac{3}{2}\theta \tag{4 11}$$

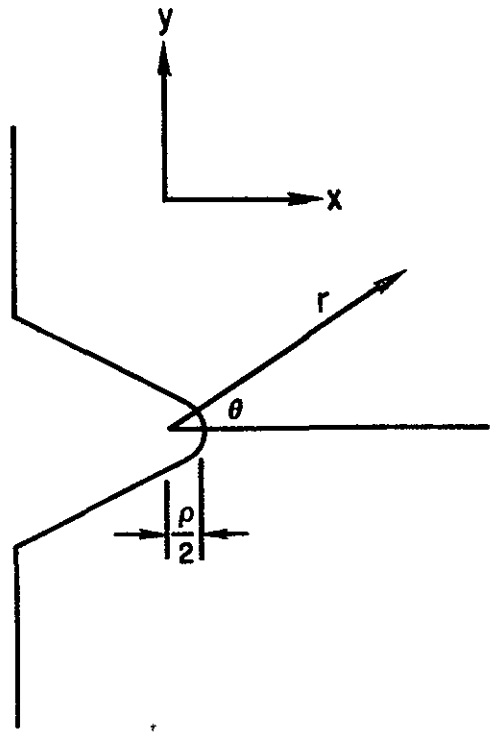

Figure 4 17 COORDINATE SYSTEM FOR STRESS FIELD

It should be noted that the origin is a distance of $\rho/2$ away from the crack tip, where ρ is the radius of curvature at the crack tip. The expressions for the stress distribution, as given by equations (4.11), hold for both the elliptic hole and the hyperbolic notch and it will be assumed that they are also valid for the Charpy notch These stress field equations differ from their plane (mathematically sharp) crack counterparts by a single additional term dependent upon the radius of curvature at the tip. For $\rho \to o$, the stress field equations for an infinitely sharp crack are recovered from equations (4.11).

To a first approximation, the extension of the plastic zone in a direction given by the angle θ can be found by putting $\tau^{max}(r,\theta)$ equal to k, where k is the yield stress in shear, and solving for r in terms of θ That is,

$$\tau^{max} = \sqrt{\frac{1}{4}(\sigma_{xx} - \sigma_{yy})^2 + \tau_{xy}^2} \quad .$$

Putting in the expressions for σ_{xx}, σ_{yy}, and τ_{xy} gives τ^{max} as

$$\tau^{max}(r,\theta) = \frac{K_I}{2\sqrt{2\pi r}} \sqrt{\rho^2/r^2 + \sin^2\theta} \quad . \qquad (4\ 12)$$

Equation (4.12) gives the maximum shear stress at any point (r,θ) in the plane due to an applied load $P(K_I = 35\ 3P)$. At the notch tip τ^{max} is given by

$$\tau^{max}(\rho/2,0) = \frac{K_I}{2\sqrt{\pi\rho}} = 100\ P,$$

and

$$\sigma_{yy}(\rho/2,0) = \frac{K_I}{\sqrt{\pi\rho}} = 200\ P \quad .$$

Therefore, $\tau_i^{max}(\rho/2,0) = \frac{1}{2}\ \sigma_{yy}(\rho/2,0)$ which means that for uniaxial tension and when yielding occurs $\tau^{max} = k = \frac{1}{2}\ \sigma_Y$. This indicates that the Tresca criterion is the criterion for yielding. For the Charpy geometry, $\sigma_{yy}(\rho/2,0) = 256.3\ P$, as given by equation (4 2), and k will thus be given by $k = \frac{1}{2}\ \sigma_Y = 128\ P_{LY}$ as compared to $100P_{LY}$ obtained from equation (4.12). This discrepancy is attributed to the assumption that the stress field equations obtained by Creager and Paris for the hyperbolic notch and elliptical hole are valid for the Charpy notch.

Putting $\tau^{max}(r_y, \theta) = k$ in equation (4 12) we get

$$k = 128\ P_{LY} = \frac{K_I}{2\sqrt{2\pi r_y}} \sqrt{\rho^2/r_y^2 + \sin^2\theta}\ .$$

This equation will finally take the form

$$12.35 \times 10^5\ r_y^3 - 3738\ 27\left(\frac{P}{P_{LY}}\right)^2 \sin^2\theta\ r_y^2 - 0\ 373827\left(\frac{P}{P_{LY}}\right)^2 = 0 \qquad (4\ 13)$$

Roots of the Equation. The equation is written as

$$r_y^3 + P_2\ r_y^2 + P_1\ r_y + P_o = o$$

Define λ and μ as

$$\lambda = \frac{1}{3}\ P_1 - \frac{1}{9}\ P_2^2$$

$$\mu = \frac{1}{6}\ (P_1\ P_2 - 3P_o) - \frac{1}{27}\ P_2^3$$

For the case where $P_1 = 0$, λ and μ would be given by

$$\lambda = -\frac{1}{9} P_2^2$$

$$\mu = -\frac{1}{2} P_o - \frac{1}{27} P_2^3 \quad .$$

Therefore,

$$\lambda^3 + \mu^2 = -[\frac{1}{9} P_2^2]^3 + [\frac{1}{2} P_o + \frac{1}{27} P_2^3]^2 \quad .$$

For the values of P_2 and P_o given by the coefficients in equation (4.13), the quantity $\lambda^3 + \mu^2$ was found to be greater than zero. Under such conditions namely $\lambda^3 + \mu^2 > o$, the equation will have one real root and a pair of complex conjugate roots

The real root r_y for an applied load $P \geq P_{LY}$ was calculated as a function of the angular coordinate θ at intervals of 5°. The relationship between r_y and θ is presented in Fig. 4.18 for different P/P_{LY} ratios The extension of the zone in the lateral direction as well as in the x-direction in the plane of the notch were obtained from Fig. 4 18 and then compared with the experimental values as shown in Fig 4 21 Fig 4 21a indicates that the lateral extension of the plastic zone as obtained from Fig 4.18 is in fair agreement with the experimentally measured values for type A specimens However, the extension of the zone in the plane of the notch as predicted by the analysis (assuming plastic isotropy) was much larger than that experimentally observed in type A specimens On the other hand, Fig. 4.21b indicates that prediction of the zone extension in the plane of the notch is in good agreement with

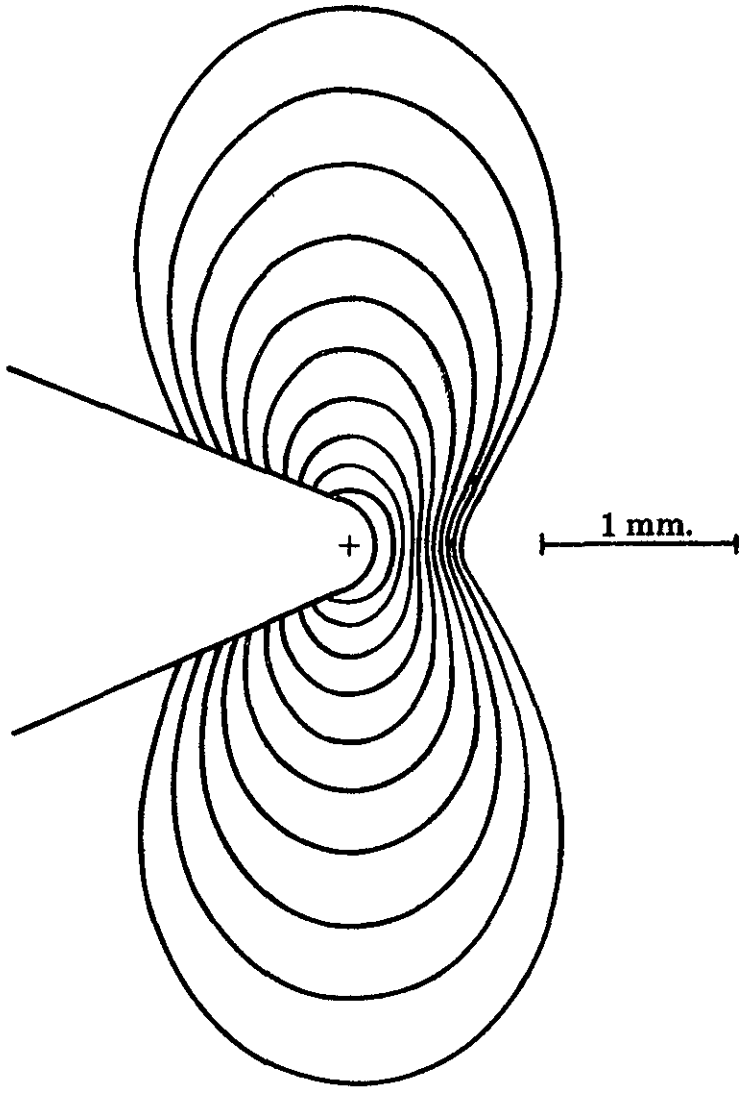

Figure 4.18 VARIATION OF r_y WITH θ FOR VARIOUS P/P_{LY}, THE SMALLEST ZONE CORRESPONDS TO $P/P_{LY} = 3/2$ AND P/P_{LY} INCREASES BY INTERVALS OF 1/2

the experimental values in the early stages of deformation of type F specimens.

4.5 Effect of Plastic Anisotropy

In conducting the above analysis, the plastic anisotropy of the material was not taken into account. As was shown, the load P_{LY} required to initiate slip in the matrix at the notch root depends on the orientation of the fibers with respect to the loading axis

Hill[60] introduced a yield criterion for states of anisotropy possessing three mutually orthogonal planes of symmetry at every point, the intersections of these planes are called principal axes of symmetry If these axes are chosen to be as Cartesian axes of reference, the yield criterion as given by Hill will be

$$F(\sigma_y - \sigma_z)^2 + G(\sigma_z - \sigma_x)^2 + H(\sigma_x - \sigma_y)^2 + 2L\tau_{yz}^2$$

$$+ 2M\tau_{zx}^2 + 2N\tau_{xy}^2 = 1$$

where F, G and H are constants related to the tensile yield stresses in the principal directions of anisotropy and L, M and N are related to the yield stresses in shear with respect to the principal axes of anisotropy. The direction along which the fibers are aligned is unique which means that it does not change from one point to the other in the material. Therefore, the orthogonal planes of symmetry and consequently the principal axes of anisotropy will not vary their direction throughout the specimen

Approximating conditions on the specimen surface by those of plane stress, the yield criterion reduces to

$$F\,\sigma_y^2 + G\,\sigma_x^2 + H(\sigma_x - \sigma_y)^2 + 2N\tau_{xy}^2 = 1 \quad . \tag{4 14}$$

For the type F fiber orientation, the z-axis is an axis of rotational symmetry (the composite is isotropic along any direction in the plane normal to the fibers) For such a case, the following relationships between the constants in the yield criterion will hold [60]

$$N = F + 2H = G + 2H \ .$$

Therefore, the yield criterion will further simplify to

$$F(\sigma_x^2 + \sigma_y^2) + H(\sigma_x - \sigma_y)^2 + 2(F + 2H)\tau_{xy}^2 = 1 \tag{4 15}$$

F and H are given by

$$2F = 1/\sigma_Z^2 \ , \ F + H = 1/\sigma_Y^2$$

where σ_X, σ_Y and σ_Z are the tensile stresses to be applied to initiate plastic flow in the matrix in the principal directions of anisotropy. Using the stress field equations given by Creager and Paris and substituting in the values for F and H, we obtain the relation between r_y and θ. That is

$$r_y^3 - \frac{K_I^2}{2\pi}\left[2F\cos^2\frac{\theta}{2} + \left(\frac{1}{2}F + H\right)\sin^2\theta\right] r_y^2 - \frac{K_I^2}{2\pi}\rho^2\left(\frac{1}{2}F + H\right) = 0 \tag{4.16}$$

The solution to this equation and its comparison with the experimental results are presented in Figs 4 19 and 4 21, respectively

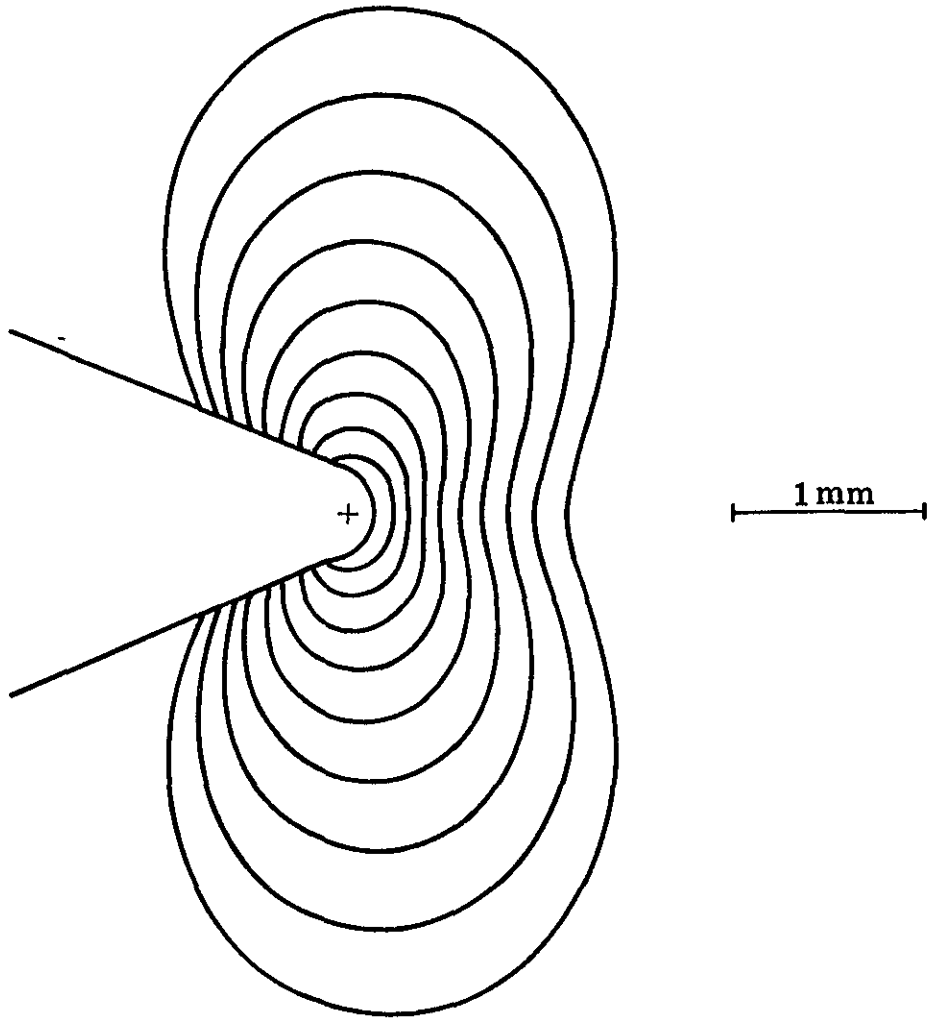

Figure 4 19 VARIATION OF r_y WITH θ FOR TYPE F SPECIMENS TAKING PLASTIC ANISOTROPY OF THE MATERIAL INTO ACCOUNT, THE SMALLEST ZONE CORRESPONDS TO $P/P_{LY} = 3/2$ AND P/P_{LY} INCREASES BY INTERVALS OF 1/2

The extension of the plastic zone in the x-direction as obtained from Fig 4.19 is presented as a function of the applied load in Fig 4.21b. It is noted that the theoretically calculated values are higher than the experimentally determined ones

For type A the fibers lie parallel to the y-axis which will be an axis of rotational symmetry Consequently the following relations between the constants in the yield criterion will hold

$$M = F + 2G = H + 2G$$

and the yield criterion will simplify to

$$F\,\sigma_y^2 + G\sigma_x^2 + F(\sigma_x - \sigma_y)^2 + 2N\tau_{xy}^2 = 1 \qquad (4\ 17)$$

where F, G and N are given by

$$2F = 1/\sigma_Y^2 \ , \ G + F = 1/\sigma_X^2 \ , \ 2N = \frac{1}{T}\,2$$

where T is the yield stress in shear with respect to the z-axis. If T is taken to be $1/2\ \sigma_Z = 1/2\ \sigma_X$, the relationship between r_y and θ will finally be

$$r_y^3 - \frac{K_I^2}{2\pi}\left[(F + G)\cos^2\frac{\theta}{2} + (F - G)\cos\frac{\theta}{2}\sin\theta\,\sin\frac{3}{2}\theta + \frac{1}{4}(F + G)\sin^2\theta\,\sin^2\frac{3}{2}\theta + F\sin^2\theta + G\sin^2\theta\cos^2\frac{3}{2}\theta\right] r_y^2$$

$$- \frac{K_I^2}{2\pi}\left[\rho(F - G)\cos\frac{\theta}{2}\cos\frac{3}{2}\theta + \frac{1}{4}\rho(F - 3G)\sin\theta\,\sin 3\theta\right] r_y$$

$$- \frac{K_I^2}{2\pi}\left[\frac{\rho^2}{4}(F + G)\cos^2\frac{3}{2}\theta + \rho^2\,(F + G\sin\frac{3}{2}\theta)\right] = 0 \ . \qquad (4.18)$$

Equation (4.18) has only one real root and a pair of complex conjugate roots Figure 4.20 depicts the value of the real root as a function of the angular coordinate θ for various values of P. The comparison between the calculated and experimental values of the plastic zone extension in the x and y directions is shown in Fig. 4 21. Fig 4 21a indicates that the agreement between the theoretical and experimental variation of the lateral extension of the plastic zone in type A specimens improved as the plastic anisotropy of the material was taken into consideration

4.6 Longitudinal Strain

Root strains were estimated using a microhardness technique This technique which is good for measuring both surface and internal strains has been applied by Knott,[61] and Wilshaw[56] to measure plastic strains around notches The technique is based on the fact that as a material is plastically deformed its resistance to further deformation increases The microhardness is therefore some function of the plastic strain.

Briefly, a number of compression specimens were strained to known amounts and the corresponding microhardness values measured to give a calibration curve. The magnitude of the plastic deformation at the root of the deformed Charpy specimen was related to that in the calibration specimen by the microhardness values Since the technique is essentially one of comparison, the orientation of the fibers with respect to the axis of loading in the test piece and the calibration specimens were equivalent.

4 6-1 Calibration

The compressive specimens shown in Fig 4 22 were used to obtain the calibration curves. The specimen ends were mechanically polished

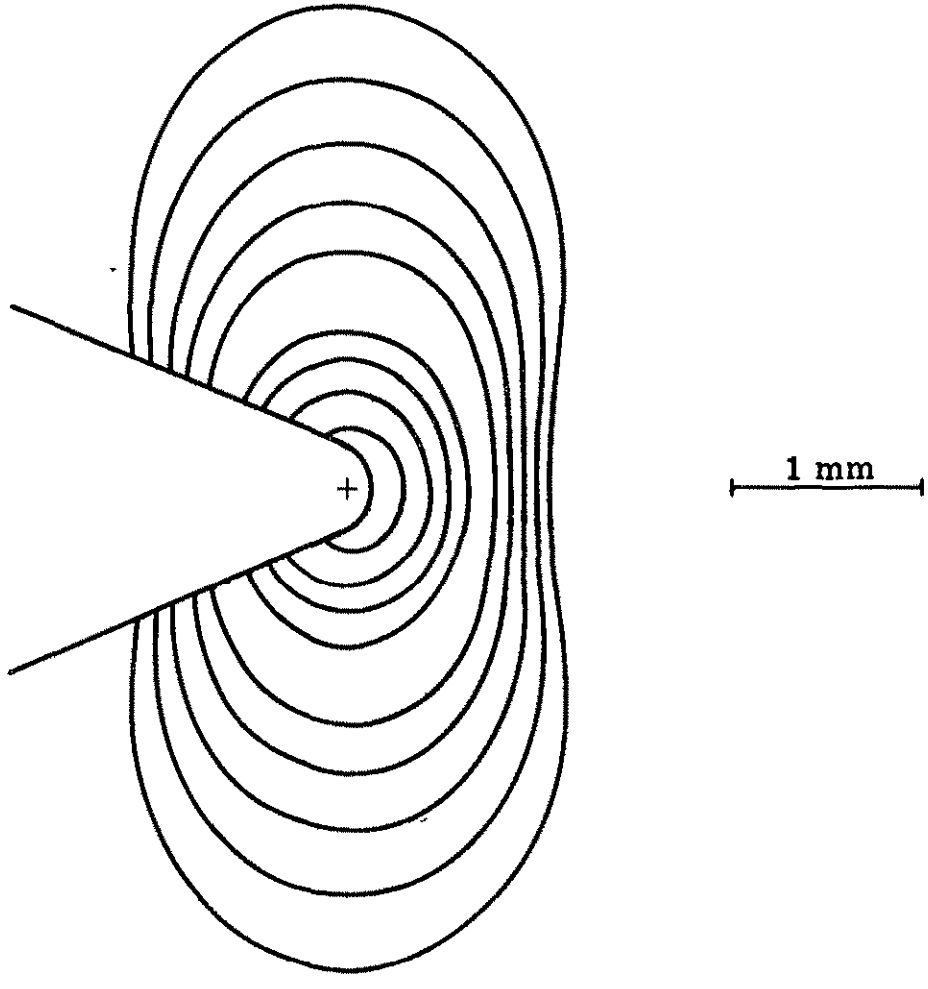

Figure 4.20 VARIATION OF r_y WITH θ FOR TYPE A SPECIMENS TAKING PLASTIC ANISOTROPY OF THE MATERIAL INTO ACCOUNT, THE SMALLEST ZONE CORRESPONDS TO $P/P_{LY} = 2$ AND P/P_{LY} INCREASES BY INTERVALS OF 1/2

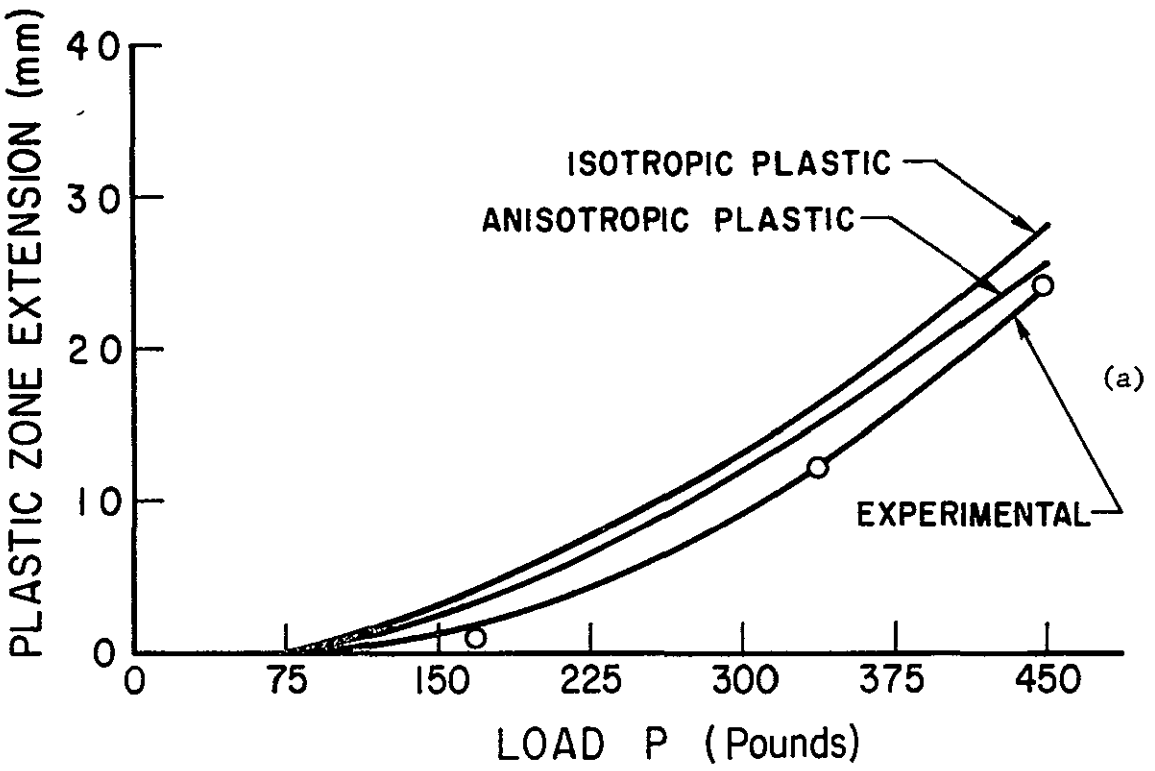

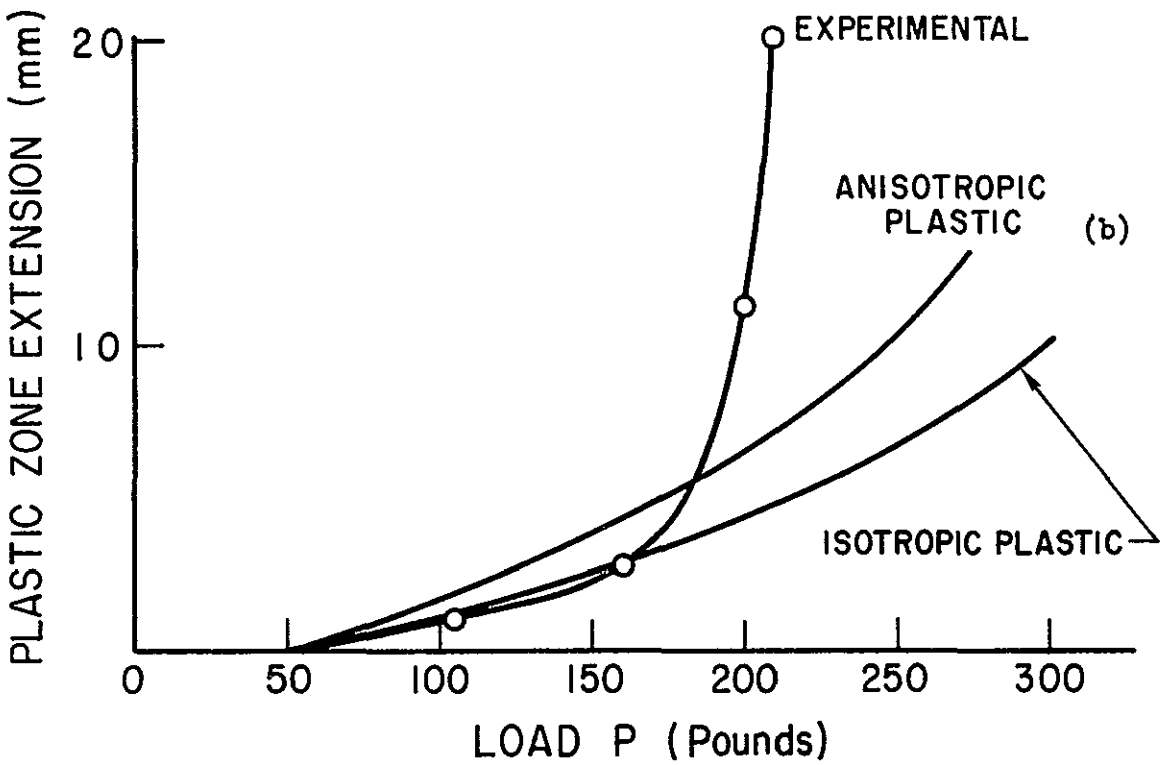

Figure 4 21 (a) VARIATION OF THE LATERAL EXTENSION OF THE PLASTIC ZONE WITH THE APPLIED LOAD IN TYPE A SPECIMENS,
(b) VARIATION OF THE EXTENSION IN THE PLANE OF THE NOTCH OF THE PLASTIC ZONE WITH THE APPLIED LOAD IN TYPE F SPECIMENS

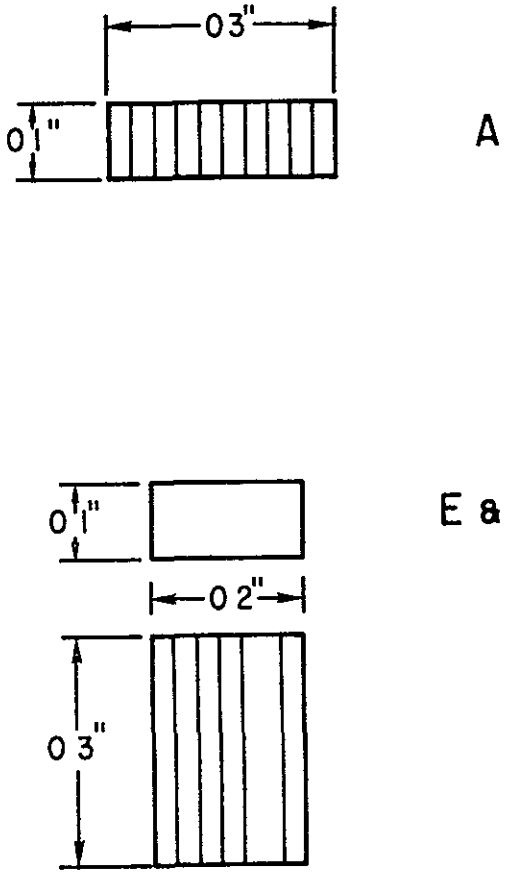

Figure 4.22 COMPRESSION SPECIMENS USED TO OBTAIN THE CALIBRATION CURVES

through 1μ diamond finish before they were checked for parallelism. Controlled amounts of plastic deformation were obtained by compressing the specimens at a strain rate of 10^{-3} sec^{-1}. Barreling was largely reduced for strains below about 40% axial compression by using a lubricant between the specimen ends and the compression plates. For axial compression in the direction of the fibers, barreling was difficult to control for deformations beyond 20%.

The deformed control specimens were mounted in cold setting plastic, mechanically polished to their midsection and then through 6μ diamond finish before they were electropolished Electropolishing removes any cold worked material which might have been introduced during mechanical polishing. Microhardness measurements were made on a Lietz microhardness tester The polished surface of the specimen was indented with a diamond pyramid and the diagonal d of the indent produced under an applied load P was measured The hardness H is related to P and d by the following relation

$$H = 1854.4 \frac{P}{d^2} \quad Kgm/mm^2$$

where P is the load in grams and d the length of the diagonal of the indent in microns The indent diagonal normal to the fibers was taken as the basis of comparison for type A and E specimens, whereas for type F the two diagonals were equivalent (the composite is isotropic in a plane normal to the fiber axis) Each specimen was indented six times under four different loads and the values of P and d were plotted on a log - log graph to obtain a family of isostrain Meyer lines as shown in Figures 4.23 and 4.24. The microhardness was calculated for a specific indent size of

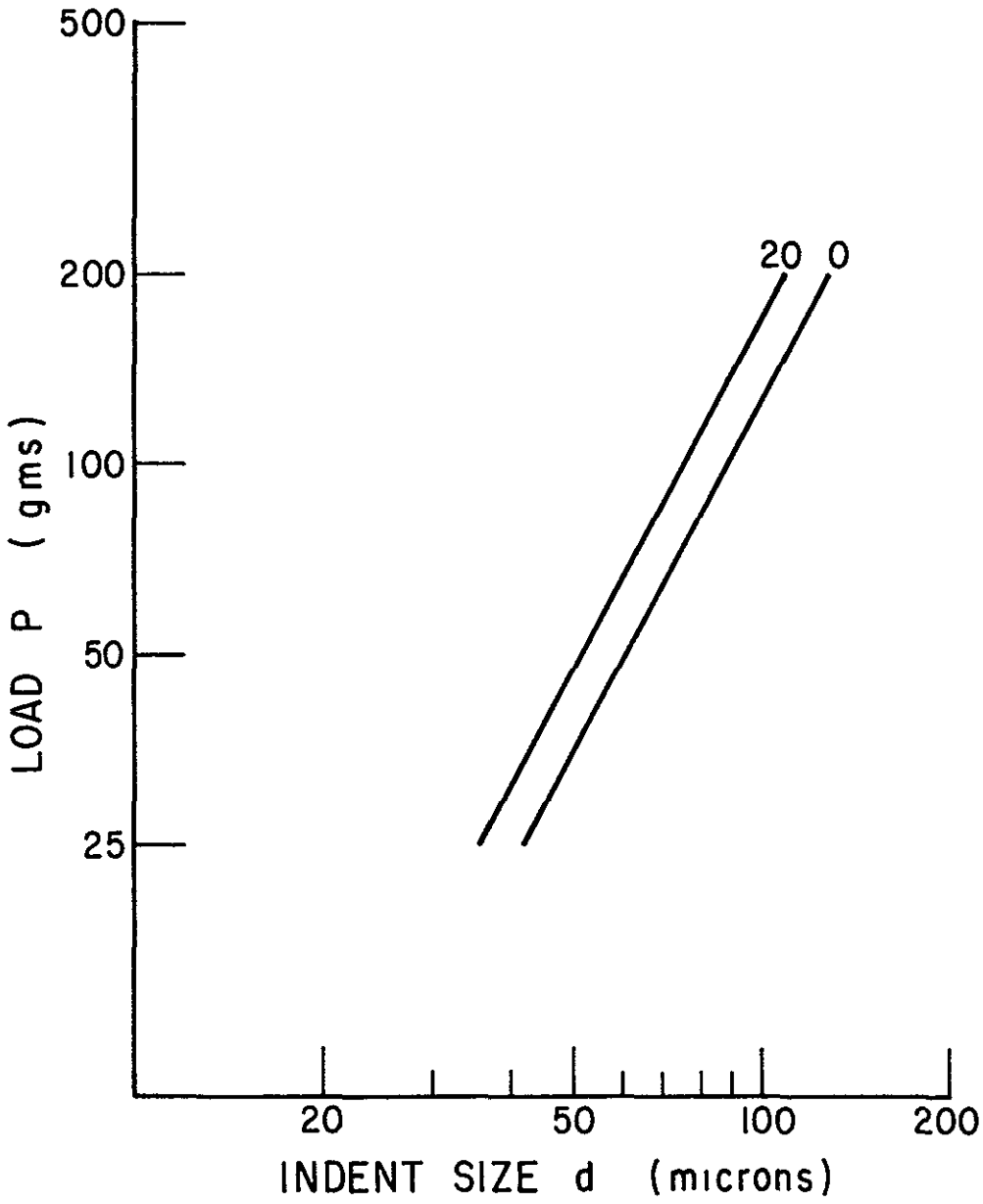

Figure 4.23 A PLOT OF LOG P VERSUS LOG D FOR DIFFERENT STRAINS (TYPE A)

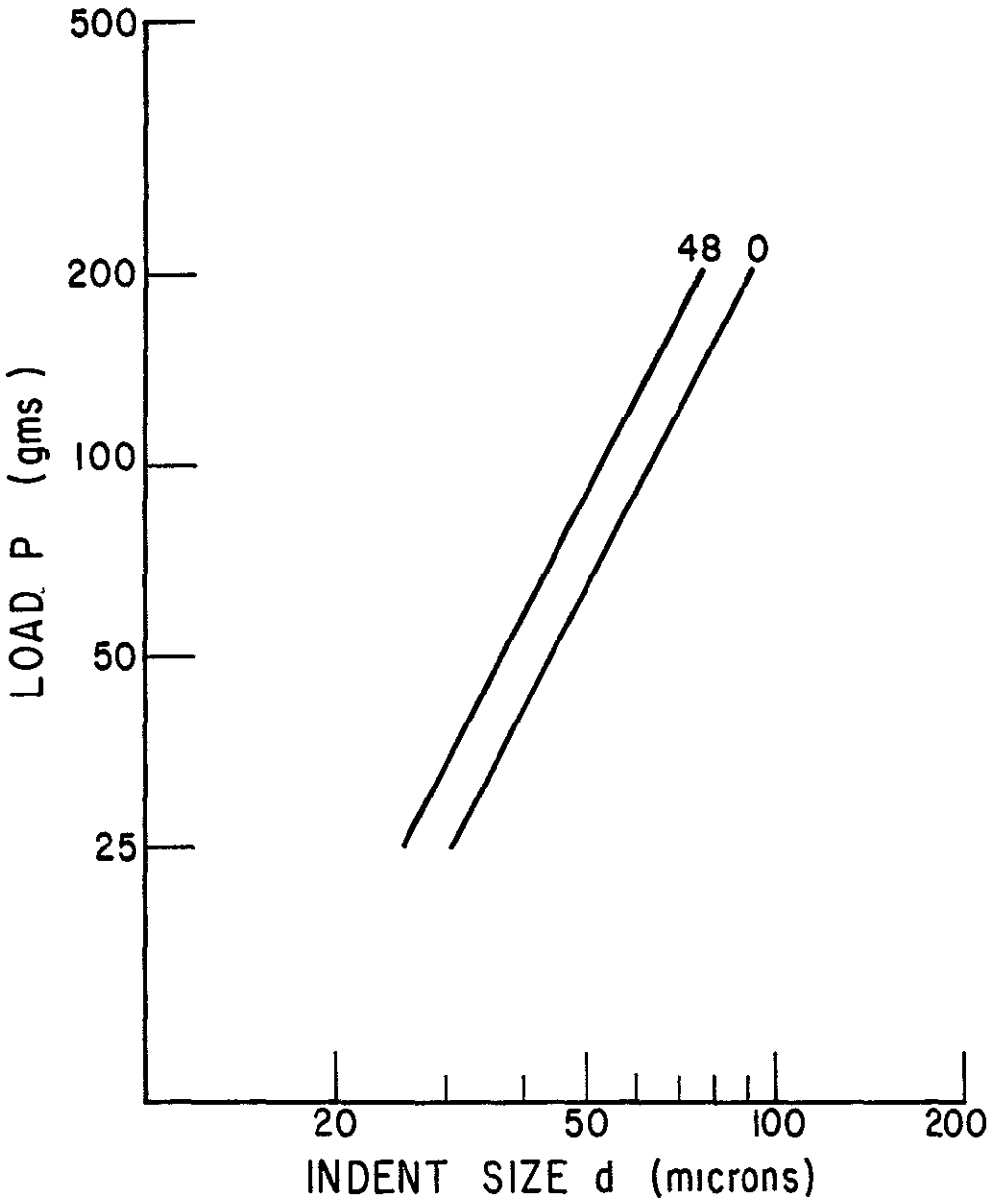

Figure 4.24 A PLOT OF LOG P VERSUS LOG D FOR DIFFERENT STRAINS (TYPE F SPECIMENS)

50μ and plotted against the strain as presented in Figures 4.25 and 4.26 for the different orientations dealt with in this work.

The shape of the calibration curve depends on the strain hardening rate of the material. The lower the strain hardening coefficient, the shallower and less sensitive is the calibration curve The degree of scatter in the microhardness values is due to inhomogeneities of the microstructure and strain Scatter in the microhardness values is greater than encountered with a homogeneous material such as steel

4.6-2 Root Strain Measurements

The deformed specimens were cut along their longitudinal midsection The sectioned specimens were mechanically and electrolytically polished in the same manner as were the calibration specimens Microhardness measurements were then made in a region adjacent to the notch root Each specimen was indented three times under a 50 gm load. Indent centers were about 35μ from the notch root. The value of the microhardness corresponding to a 50μ size indent was calculated and the corresponding root strain was then obtained from the calibration curves. The value of the root strain is related to the applied load P and the bend angle θ_p in Figures 4 27 and 4 28 respectively

For mild steel, Wilshaw[56] has shown that the distribution of plastic strain is not affected by changes in temperature. Ahead of the Charpy V-notch and in the notch plane the strain distribution is given by[56,62]

$$\varepsilon(x) = F \frac{\theta_P}{x}$$

where x is the distance ahead of the Charpy notch and F is a constant that depends on the root radius.

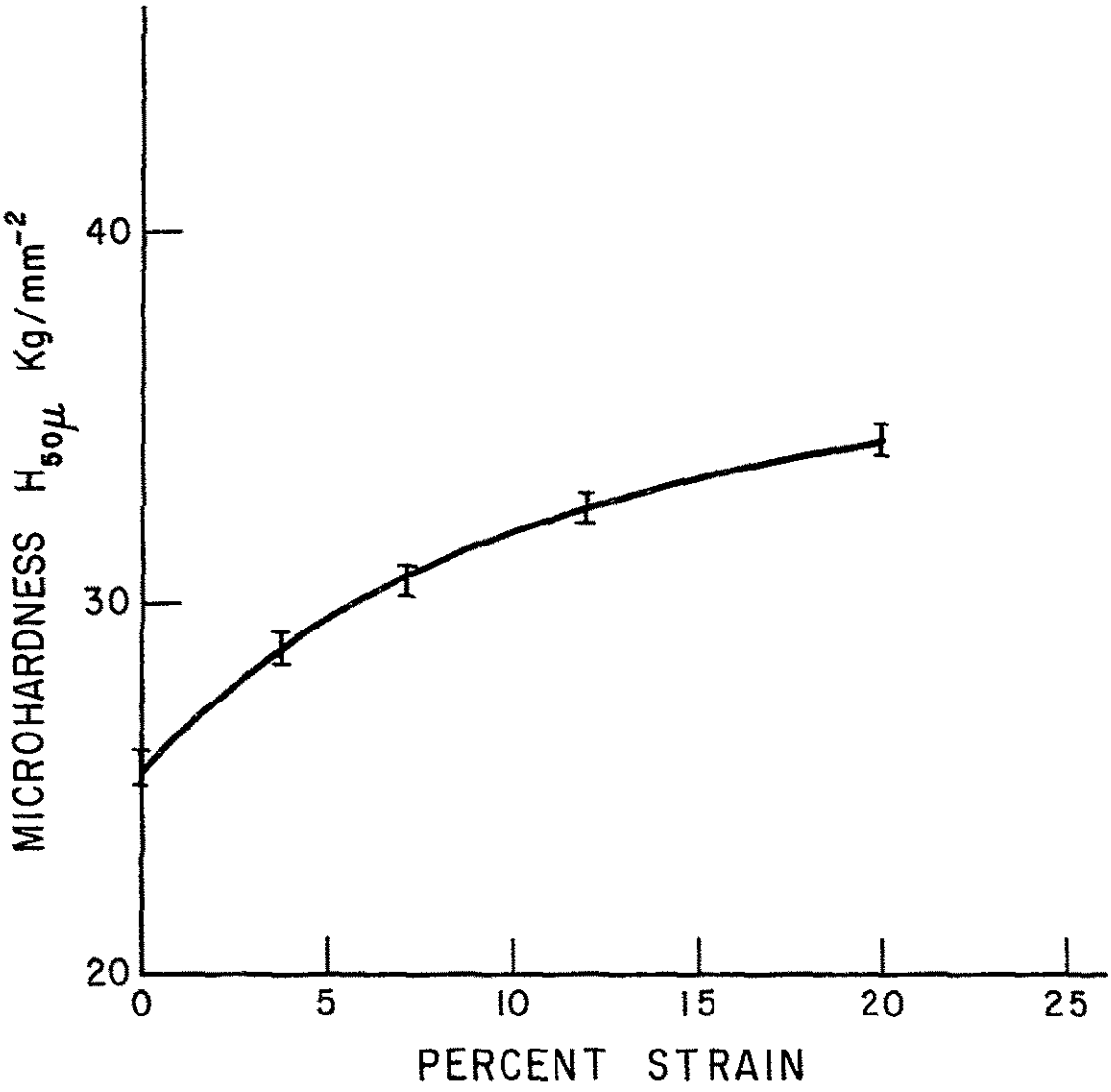

Figure 4 25 THE VARIATION OF MICROHARDNESS WITH STRAIN FOR AN INDENT SIZE OF 50μ (TYPE A)

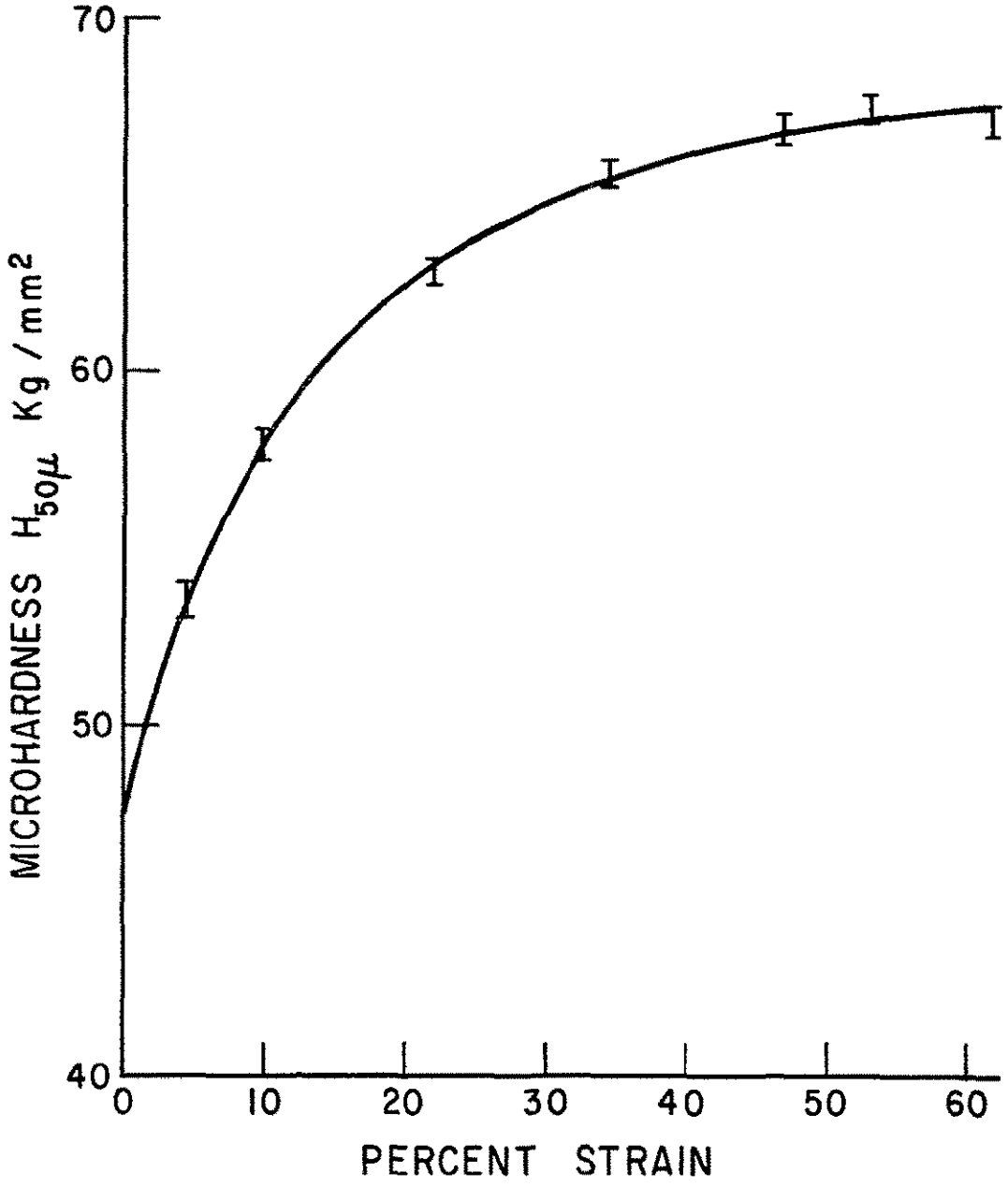

Figure 4.26 THE VARIATION OF MICROHARDNESS WITH STRAIN FOR AN INDENT SIZE OF 50μ (TYPE F)

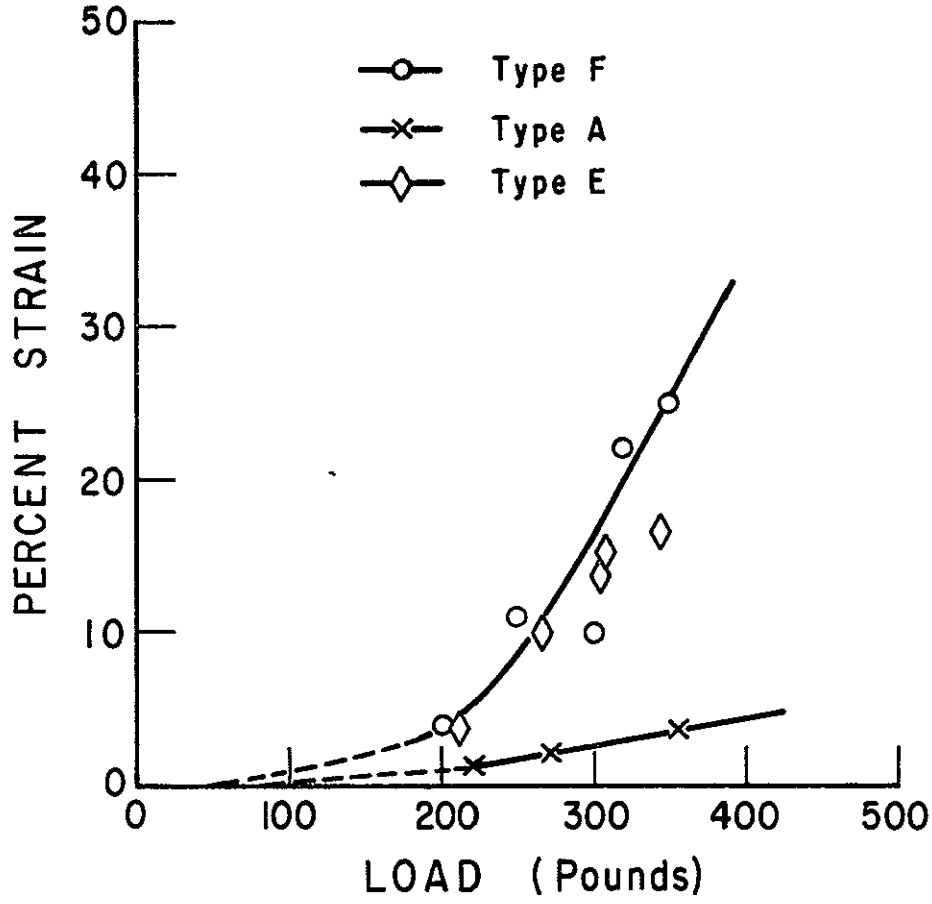

Figure 4.27 VARIATION OF ROOT STRAIN WITH APPLIED LOAD

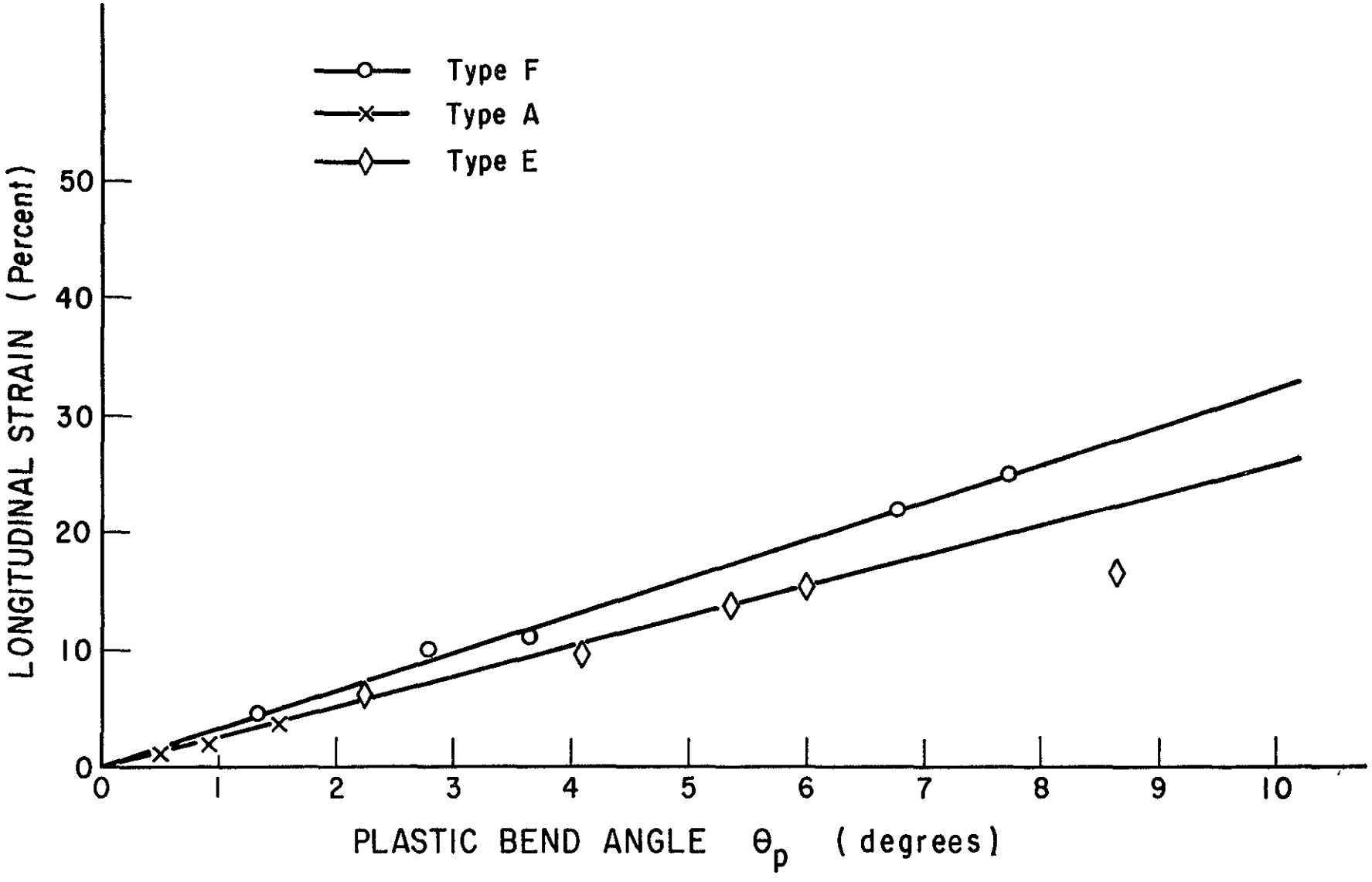

Figure 4 28 VARIATION OF ROOT STRAIN WITH BEND ANGLE

Experimentally it was found that[56] the root strains are finite at a given value of θ_p and Tetelman and Wilshaw[63] modified the above equation to

$$\varepsilon(x) = F \frac{\theta_p}{x} \qquad x \geq x^*$$

where x* is some finite distance ahead of the notch over which the root strains are constant.

The measurements made on the composite indicate that the root strain is given by (Fig. 4 28)

$$\varepsilon_{yy} = \beta \cdot \theta_p$$

where β is a constant that is equal to 3 2 forttype F specimens and to 2.6 for type A and E specimens.

The distribution of plastic strain is not affected by changes in temperature and the experimental relationship between the bend angle and root strain at room temperature will continue to be valid for predicting root strains at other temperatures

4.7 Transverse Strain

The transverse notch contraction at the notch root was measured using a Lietz microscope. The polished side surface of the specimen was first brought into focus and the position was measured using a calibrated scale in the microscope eyepiece. The position of the lowest part of the notch root surface was similarly measured and from the difference between the two readings on the calibrated scale, the contraction in the transverse direction was determined The transverse notch contraction

which will be referred to as the transverse strain was correlated with the applied load P and the bend angle θ_p and is shown for the different type orientations in Figures 4.29 and 4.30 respectively

The slope of the curve of type E specimens, shown in Fig 4 29, increases with P and tends to high values as cracking is incipient As for type F, the slope of the curve increases with P at a slow rate then starts to decrease until the curve eventually levels off to a very small percentage of notch contraction The curve has been extrapolated below 200 pounds, assuming that the transverse strain is zero at P = 50 pounds which is the load equal to P_{LY}.

The transverse strain for a type E specimen, Fig. 4.30, increases with the angle of bend θ_p in a linear fashion at a rate of 0.7% per degree. The slope of the curve tends to decrease as cracking is incipient. As for type F, the slope of the curve is almost linear at the beginning and then starts to gradually decrease until it finally levels off corresponding to a plastic bend angle of about 10° The initial rate of transverse strain increase with θ_p is about 0 1% per degree.

4.8 Discussion

The variation of the transverse strain with the applied load and plastic bend angle for the three type orientations reflects the anisotropic nature of the plastic behavior of the composite The transverse strain is a function of the longitudinal strain and for mild steel a linear relationship with a slope of 1/8 was obtained between the two.[56] In a fiber composite, the functional relationship depends on the orientation of the fibers with respect to the loading axis and the notch edge The material can undergo a considerable deformation in a direction

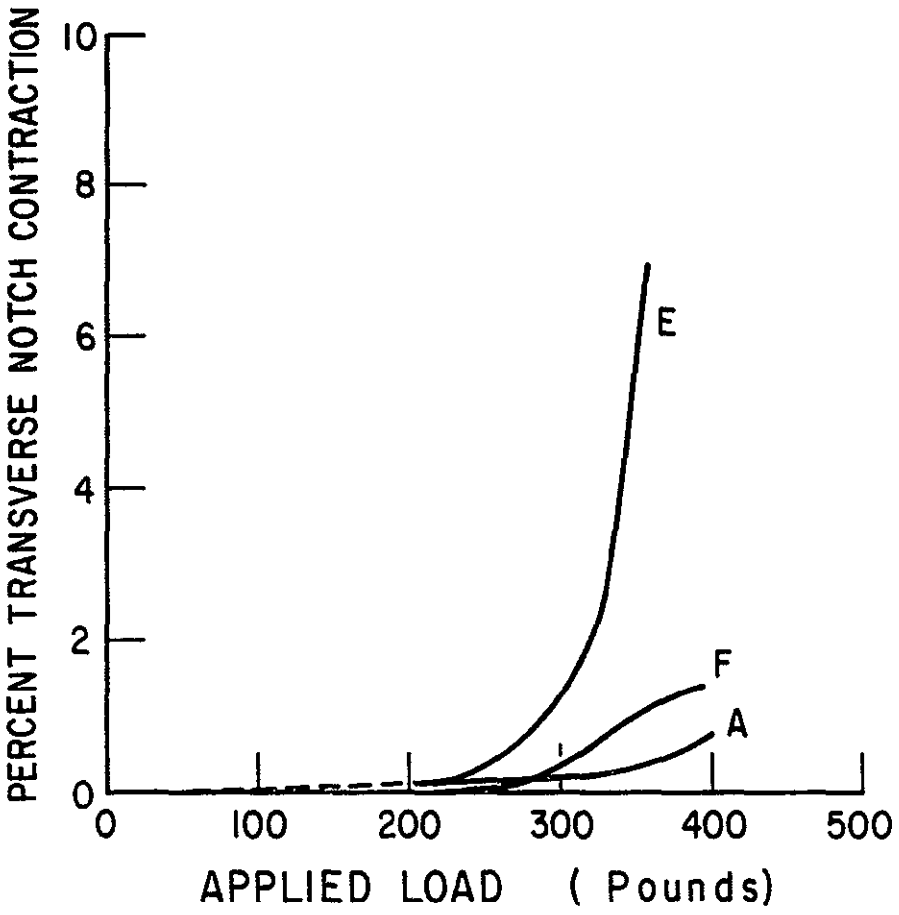

Figure 4.29 VARIATION OF NOTCH CONTRACTION WITH APPLIED LOAD

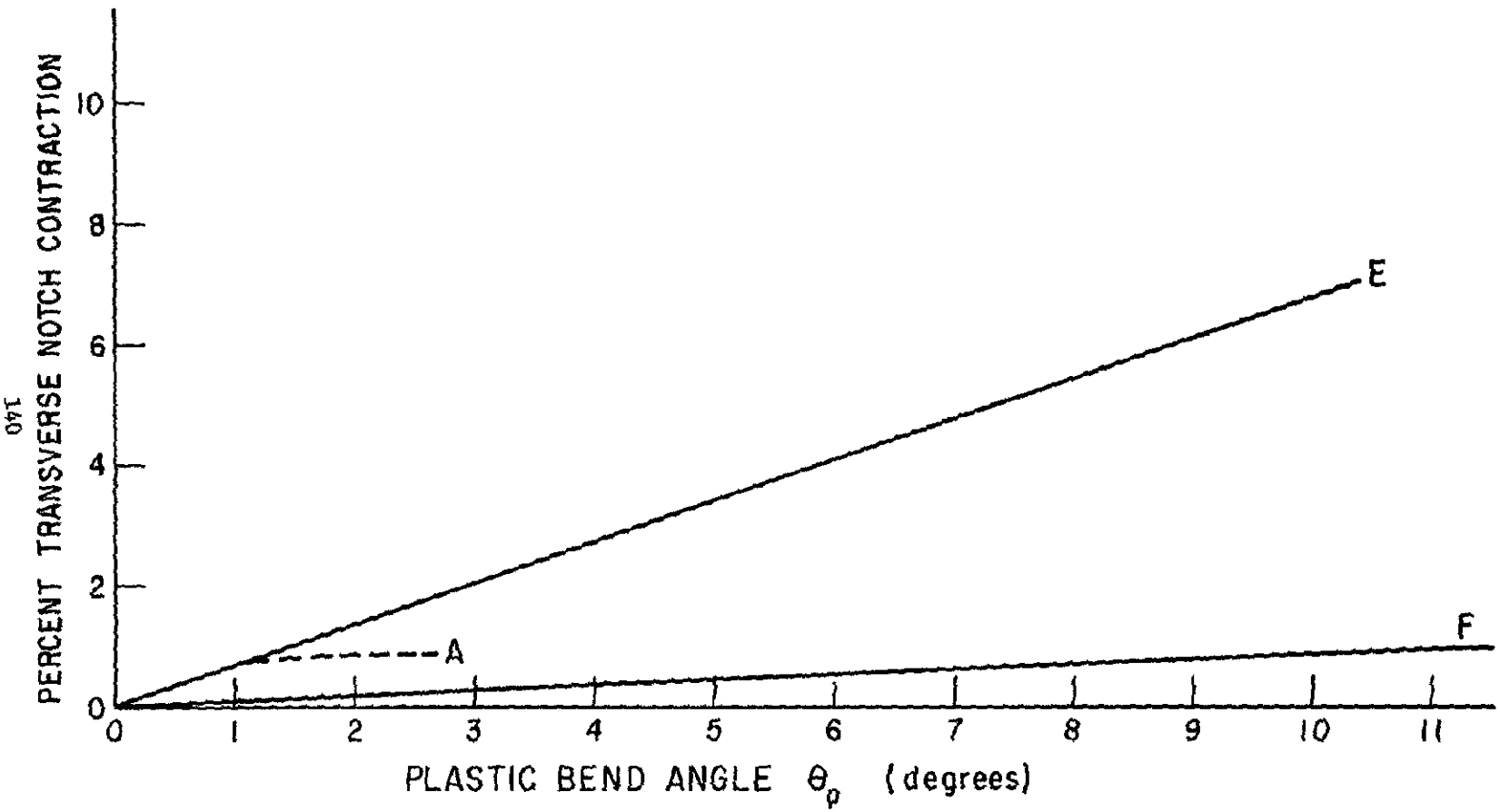

Figure 4.30 VARIATION OF NOTCH CONTRACTION WITH BEND ANGLE

normal to the fiber axis whereas in the direction parallel to the fibers, deformation is limited by the elastic strain of the fibers which does not exceed 2% at room temperature. In addition to the longitudinal strain, transverse strain will also depend on the ability of the material to undergo plastic deformation in that particular direction and therefore on fiber orientation.

The relationship between the transverse and longitudinal strain for the three type orientations is represented in Fig 4.31 This relationship can be expressed as

$$\varepsilon_{zz} = \alpha \varepsilon_{yy}$$

where ε_{zz} and ε_{yy} are the transverse and longitudinal strain respectively, and α is a parameter that depends on the fiber orientation

For type A specimens the longitudinal strain ε_{yy} is small and so will be the transverse strain. On the other hand, in a type F specimen, the material is loaded in a direction normal to the fibers Therefore, the longitudinal strains would attain values as high as 40% However, the fact that the fibers are aligned parallel to the notch edge would considerably diminish the transverse notch contraction, hence α_F is considerably small ($\alpha_F = 1/40$) as shown in Fig. 4 31. Considerable contraction is observed in the x-direction as shown in Fig 5 5. Large deformations along the y-axis results in a correspondingly large deformation along the z-axis in type E specimens ($\alpha_E = 1/4$) No significant contraction was observed along the x-axis which is the fiber direction in this case.

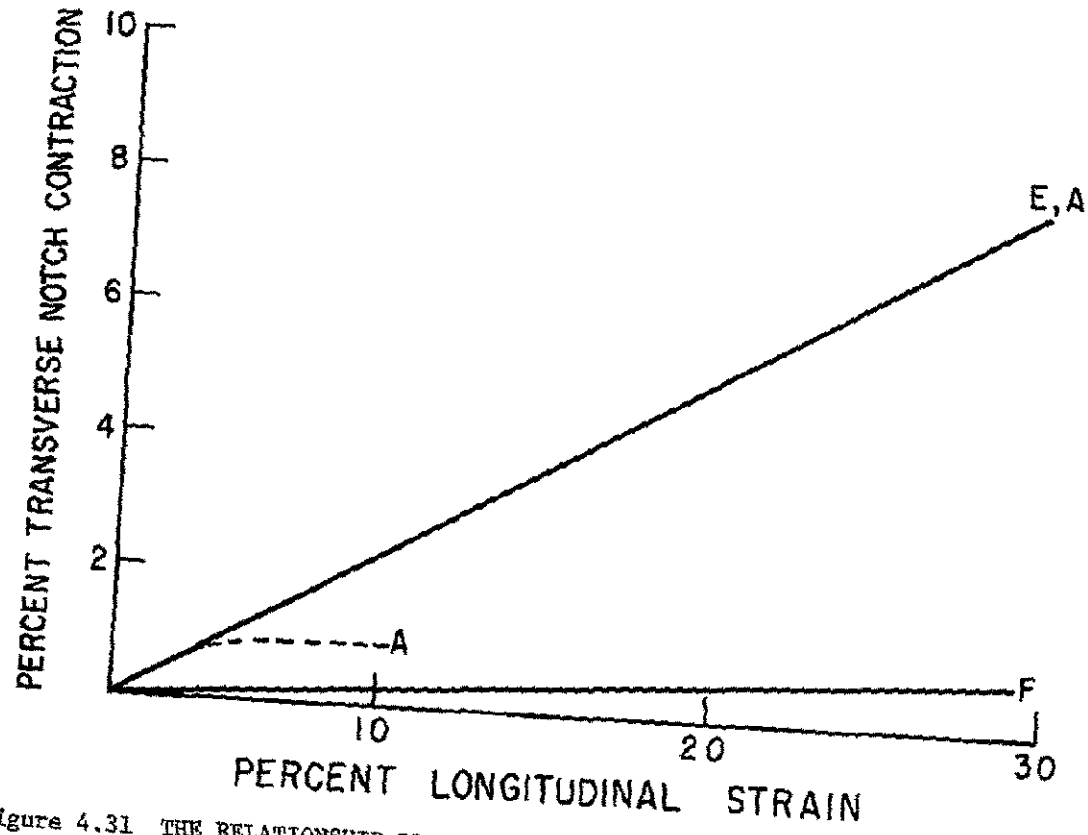

Figure 4.31 THE RELATIONSHIP BETWEEN THE TRANSVERSE AND LONGITUDINAL STRAIN

CHAPTER V

THE EFFECT OF TEMPERATURE AND FIBER ORIENTATION ON THE LOAD CARRYING CAPACITY AND FRACTURE INITIATION IN CHARPY BARS

The experiments described in this chapter were designed to determine the dependence on temperature of the load carrying capacity of Charpy bars for the three fiber orientations A, E and F Experiments designed to correlate fracture initiation with the macroscopic strain parameter θ_P (plastic bend angle) at different temperatures were also conducted The angle of bend at approximately the moment of fracture initiation θ_I, was determined and correlated with the local plastic strains which were measured using microhardness values. The initiation load P_I which is the load to be applied to deform the specimen to a bend angle θ_I was compared to the ultimate load P_u

Criteria for fracture initiation were introduced and discussed

5 1 The Load-Deflection Curve

The relationship between the applied load and the deflection of the specimen δ is plotted in Fig 5 1 P-δ curves are shown for each of the three fiber orientations at three different temperatures, -196°C, 25°C, and 200°C A common feature among the curves is that none of them exhibits a well-defined yield point and consequently a general yield load could not be obtained from the curves Even after the maximum load is achieved, fracture proceeds in a stable manner at all temperatures in the range -196°C→200°C A continuous path of plastic deformation can be traced across the section of a bar with the fiber orientation type F at a load of about 200 pounds ´This load can be regarded as the load for the

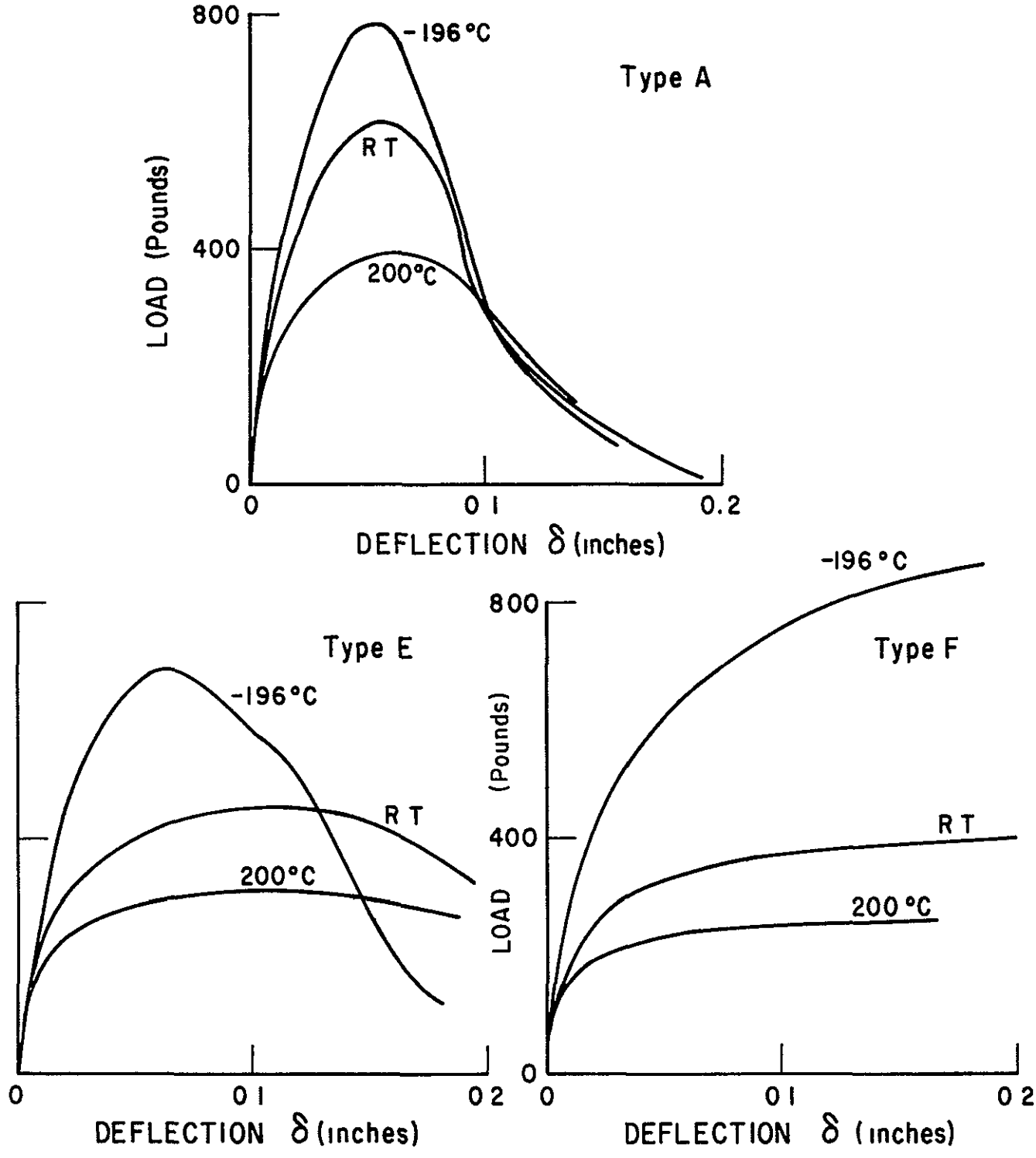

Figure 5.1 THE LOAD-DEFLECTION CURVE

onset of plastic instability or in other words the general yield load as discussed in Chapter IV

5 2 Ultimate Load

The relationship between the ultimate load of Charpy bars loaded in three point slow bend and the test temperature is shown in Fig 5 2 For the type F orientation, the ultimate load exhibits a monotonic decrease as the temperature increases, a behavior which is qualitatively similar to that of the composite tensile strength in the transverse direction (Fig 3 20) As for the A and E orientations, the behavior was found to be linear with the ultimate load dropping at the rate of 20 pounds/30°C for type A and one pound/degree for type E. Fig 5 2 also depicts the variation of the load corresponding to the limit of proportionality on the P-δ curve with the test temperature This load was found to be lower at higher temperatures, a behavior which is common for the three orientations

It should be noted that fracture proceeded in a stable manner even for the type A fiber orientation which gives the lowest ductility of all orientations at all temperatures in the range -196°C→200°C Although cracks started to develop, the load supported by the specimen continued to increase until eventually the ultimate load was reached, then the load started to decrease on further deformation However, for specimens with the type F orientation the load did not start to decrease in the deformation range limited by the maximum bend angle imposed by the bend jig The difference between P_u and P_I which depends on the test temperature, will be discussed later.

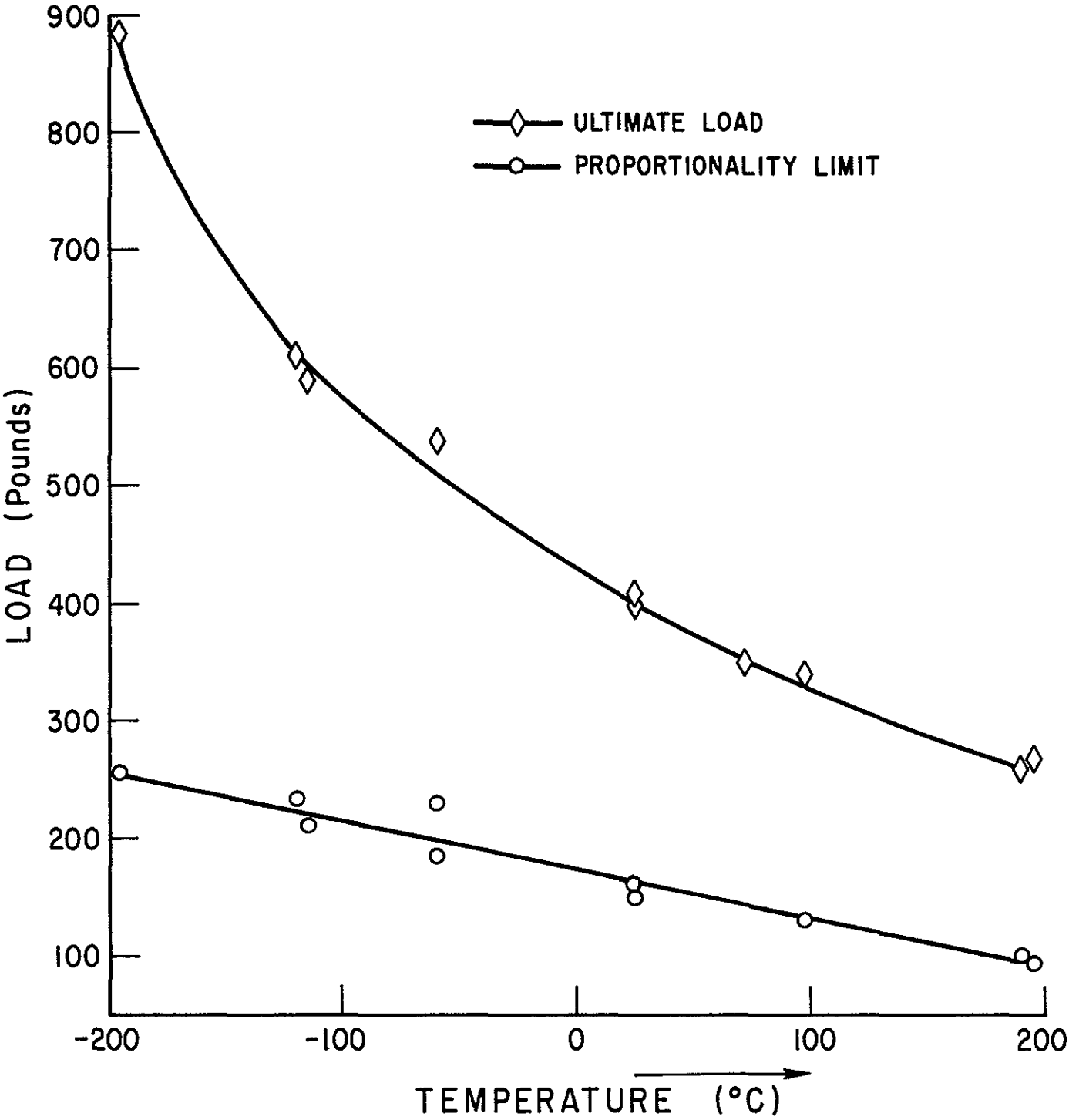

Figure 5 2a VARIATION OF THE ULTIMATE LOAD WITH TEMPERATURE FOR THE TYPE F SPECIMENS

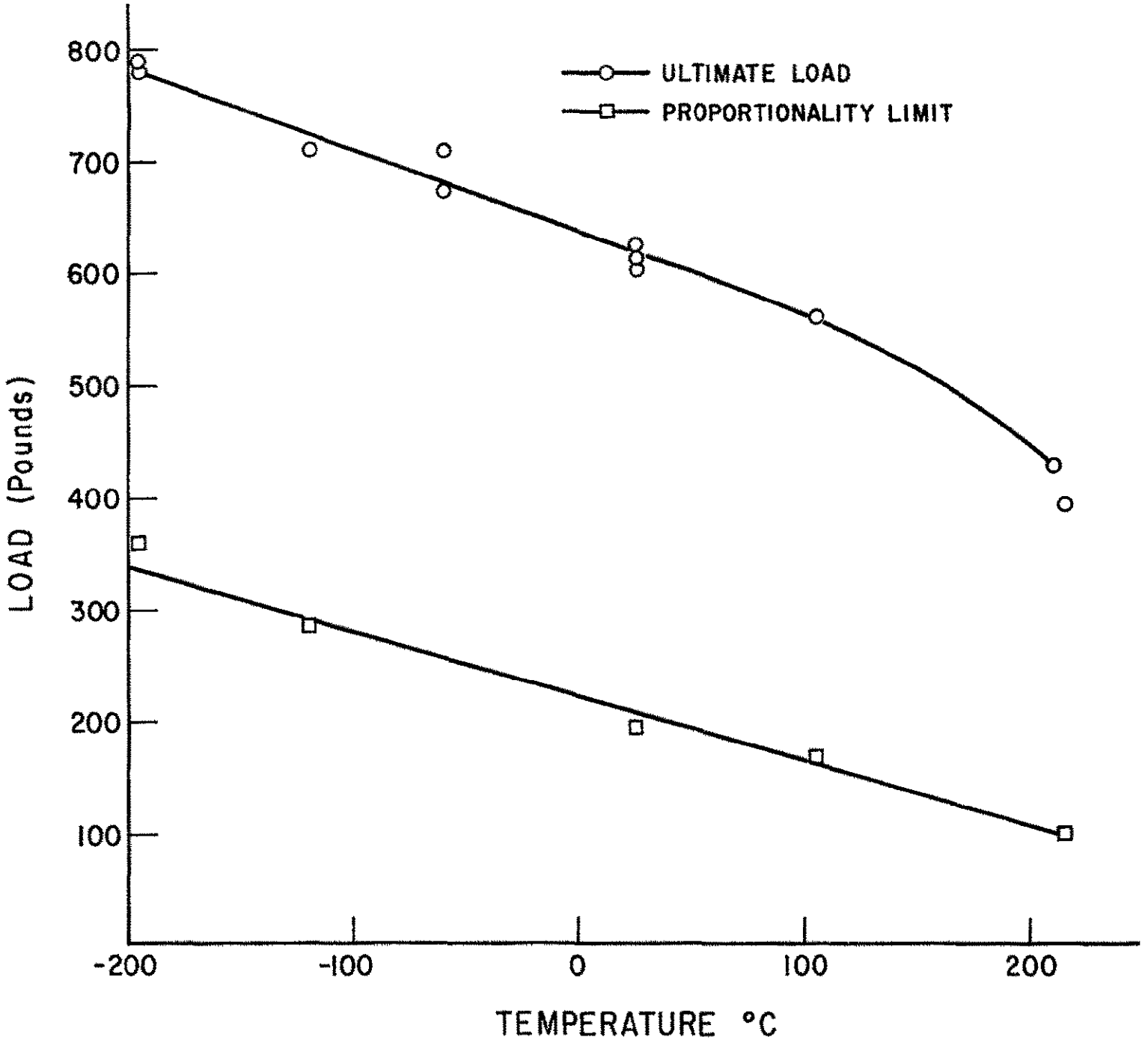

Figure 5.2b VARIATION OF THE ULTIMATE LOAD WITH TEMPERATURE FOR THE TYPE A SPECIMENS

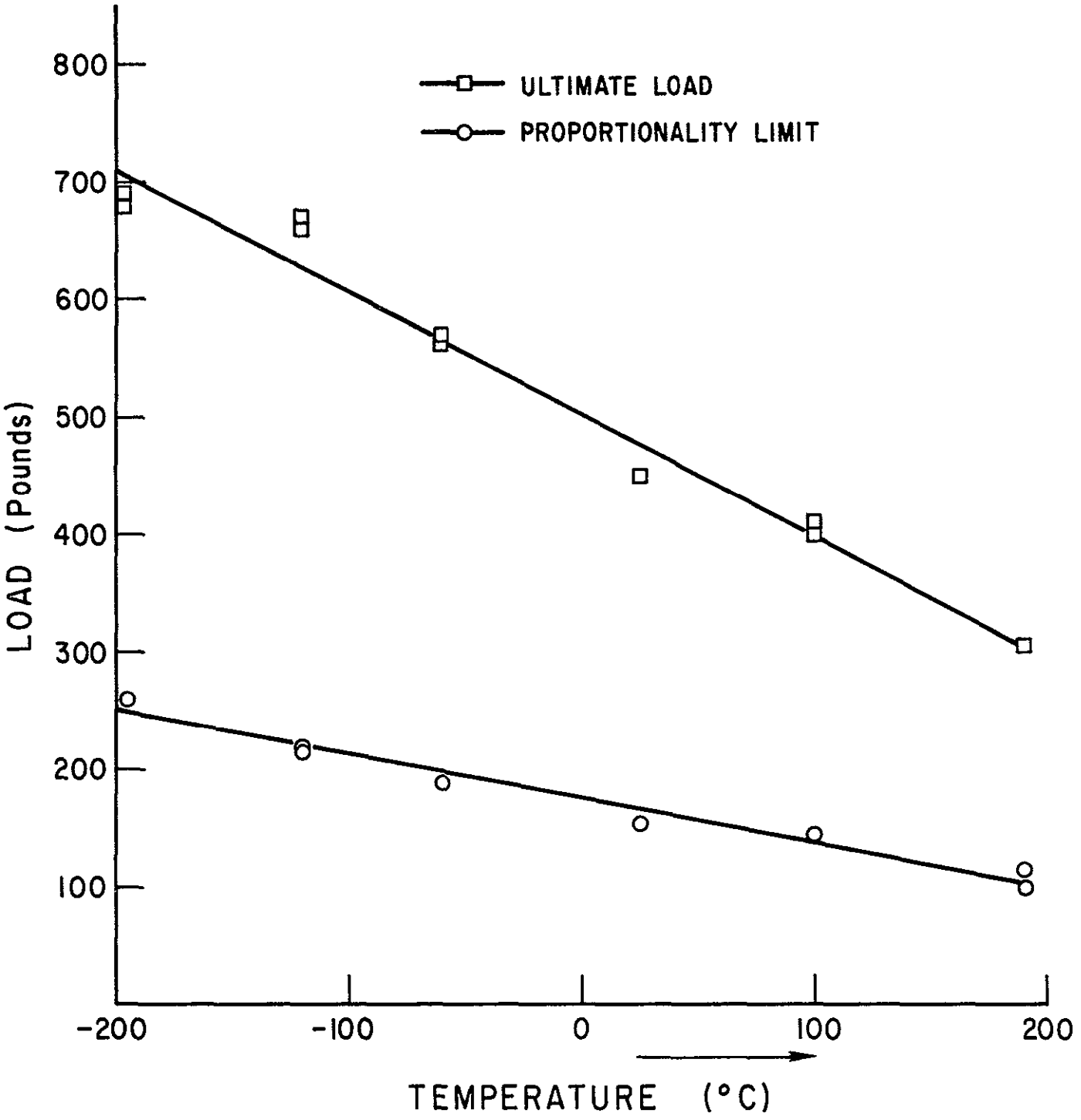

Figure 5 2c VARIATION OF THE ULTIMATE LOAD WITH TEMPERATURE FOR THE TYPE E SPECIMENS

5 3 The Fracture Surface

Fracture profiles of type A specimens loaded to failure at different test temperatures in the range -196°C→200°C are shown in Fig 5 3 It is noted that the net propagation of the crack is in the transverse direction However, the crack locally tends to turn and run longitudinally The change in the direction of the crack as it stably propagates across the specimen ligament results in an irregular fracture surface that becomes more irregular at higher test temperatures (Fig 5 3) The tendency of the crack to divert its direction more frequently at higher temperatures is presumably due to the decrease in matrix strength as the temperature is raised Splitting in the matrix between the fibers can proceed under the effect of the transverse stress σ_{xx} ahead of the moving crack and since the matrix becomes weaker at higher temperatures, splitting in it can occur more readily at higher test temperatures

Fracture surfaces of the type E specimens were found to be quite flat Crack propagation in the transverse direction now parallel to the fibers, is prevented from being diverted laterally by the presence of the fibers on either side Fracture profiles of type E specimens loaded in three point slow bend are represented in Fig. 5.4 It is noted that the crack did not propagate across the entire ligament even when the specimens were deformed to the maximum bend angle imposed by the jig Depth and width of the crack were found to depend on temperature, with the crack getting shallower and its width becoming more restricted to the central part around the specimen midsection at higher test temperatures

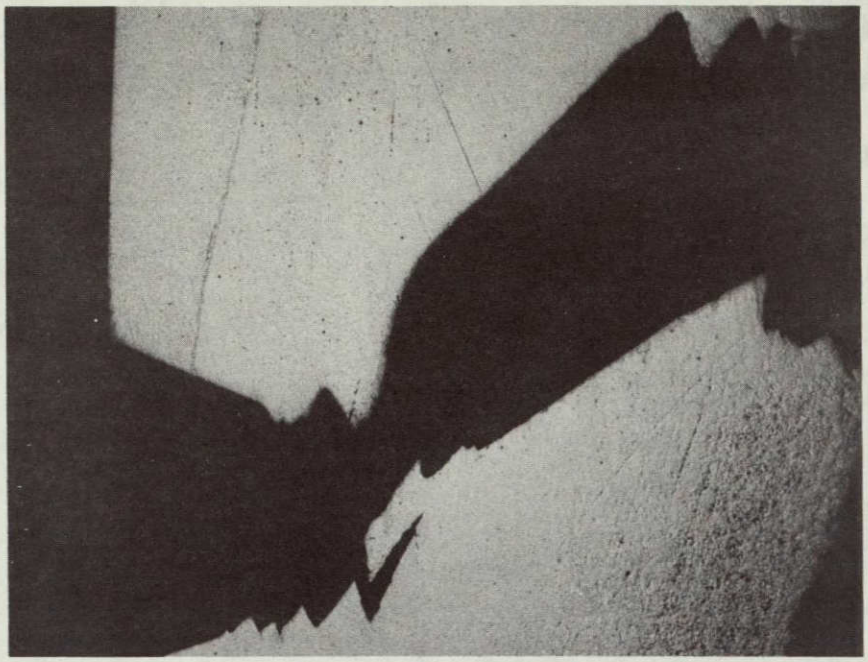

(a)

(b)

Figure 5.3 FRACTURE PROFILE OF TYPE A SPECIMENS, MAGNIFICATION = 9.6X, (a) Temperature = -196°C, (b) Temperature = 200°C.

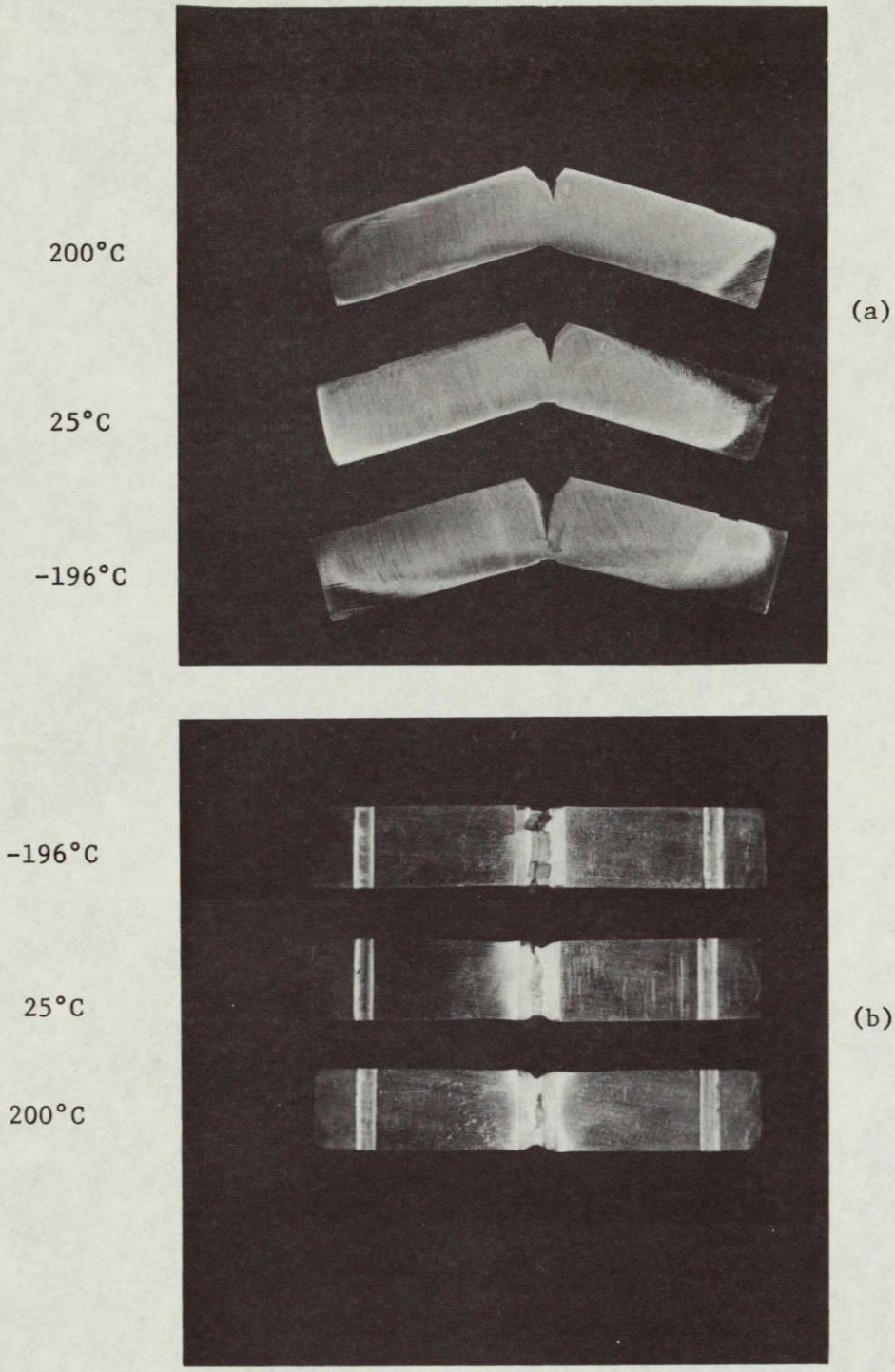

Figure 5.4 (a) FRACTURE PROFILE OF TYPE E SPECIMENS DEFORMED TO THE SAME BEND ANGLE AT VARIOUS TEMPERATURES, (b) A TOP VIEW OF THE SAME SPECIMENS.

The general appearance of a type F specimen deformed in three point bending is shown in Fig. 5.5. A crack started at the notch root and extended to a small distance ahead of the root. The crack surface appeared to be rough since the crack could readily be diverted around fibers or on slip planes near 45^{o} to the advancing crack direction. Therefore, the crack surface would be limited to a cylindrical surface parallel to the whisker orientation.[36] Replicas of the fracture surface are shown in Fig. 5.6.

In the process of starting a crack and having it propagate across the specimen section, energy is absorbed. The fracture energy is the summation of two energy terms, initiation and propagation. Fracture initiation and crack propagation are discussed in the following sections.

5.4 Fracture Initiation

The plastic bend angle θ_I (corresponding to an applied load P_I) required to initiate fracture in Charpy specimens loaded in three point bending were determined as a function of the temperature for type A and E specimens.

The specimens were polished on one side to a 6μ diamond finish before they were loaded at various test temperatures. After unloading, the specimen surface was investigated for possible cracks developing in the notch vicinity. The lowest part of the notch root surface was brought in focus at a fairly high magnification (100X) and scanned for cracks that might have developed. If cracking was not observed, the applied load would be increased until the specimen eventually started to crack. Specimens deformed to selected values of P below P_I, which is the load

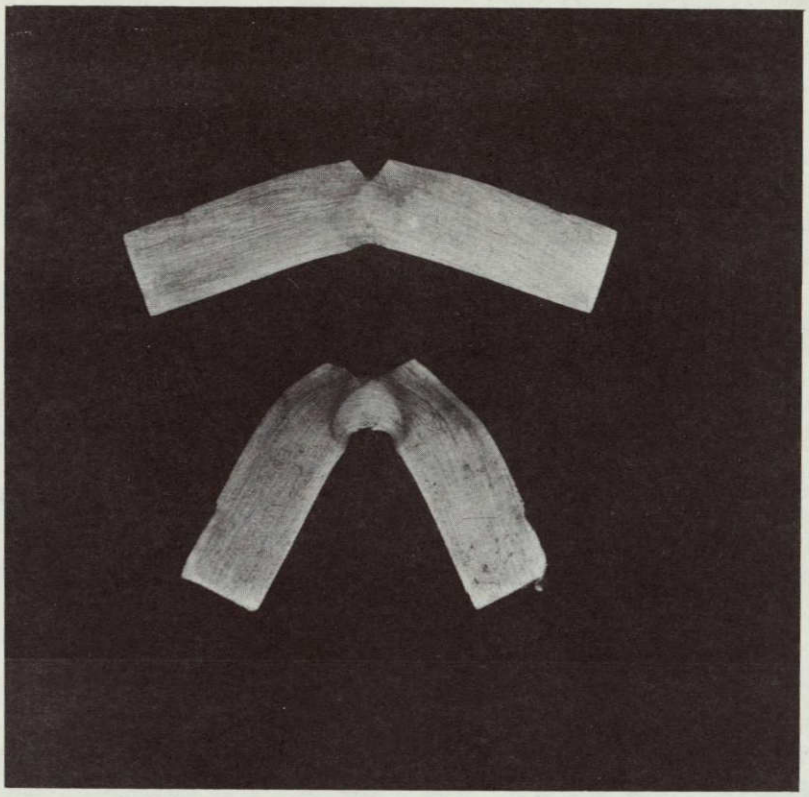

Figure 5.5 GENERAL APPEARANCE OF A DEFORMED TYPE F SPECIMEN.

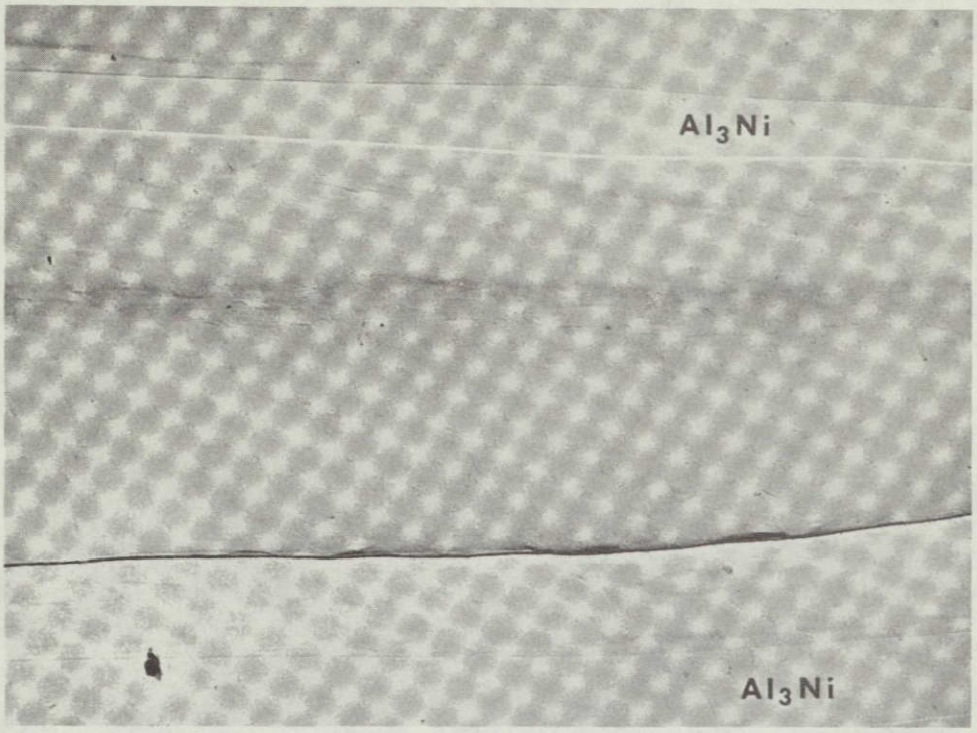

(a)

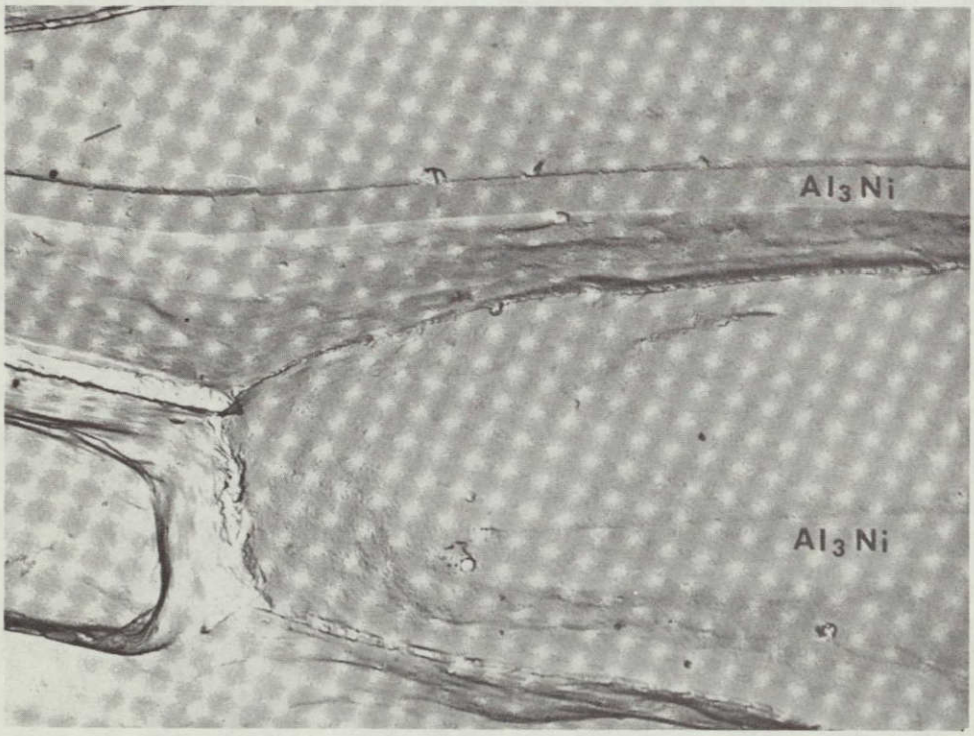

(b)

Figure 5.6 REPLICAS OF THE FRACTURE SURFACE (SALKIND AND GEORGE[36]), MAGNIFICATION = 8500X, (a) Type E, (b) Type F.

recorded for crack initiation along the notch root, were sectioned longitudinally along the midplane, polished and then metallographically examined. No cracks were found to develop below the notch root.

5.4-1 Location of First Crack

Cracking in type A specimens starts at the notch root along the entire length of the leading edge of the notch (Fig. 5.7); this was found to be the case at all temperatures in the range of interest $-196^{o}C \rightarrow 200^{o}C$. As for type E specimens, cracking starts at the notch root in the specimen midsection at all temperatures in the range (Fig. 5.8).

5.4-2 The Relationship between θ_I and T, and P_I and T

The relationship between θ_I and the test temperature is depicted in Fig. 5.9. It is noted that:

(1) The plastic bend angle required for fracture initiation in type A specimens increases as the test temperature is lowered.

(2) At any temperature in the range $-196^{o}C \rightarrow 200^{o}C$, the plastic bend angle for crack initiation in type E is much higher than that required to initiate cracks in type A.

(3) For type E specimens, θ_I decreases with the temperature reaching a minimum of about 5^{o} 30' corresponding to a temperature of about $-30^{o}C$ then starts to increase with further increase in the test temperature. This behavior is similar to the variation of the elongation on fracture in tensile loading.

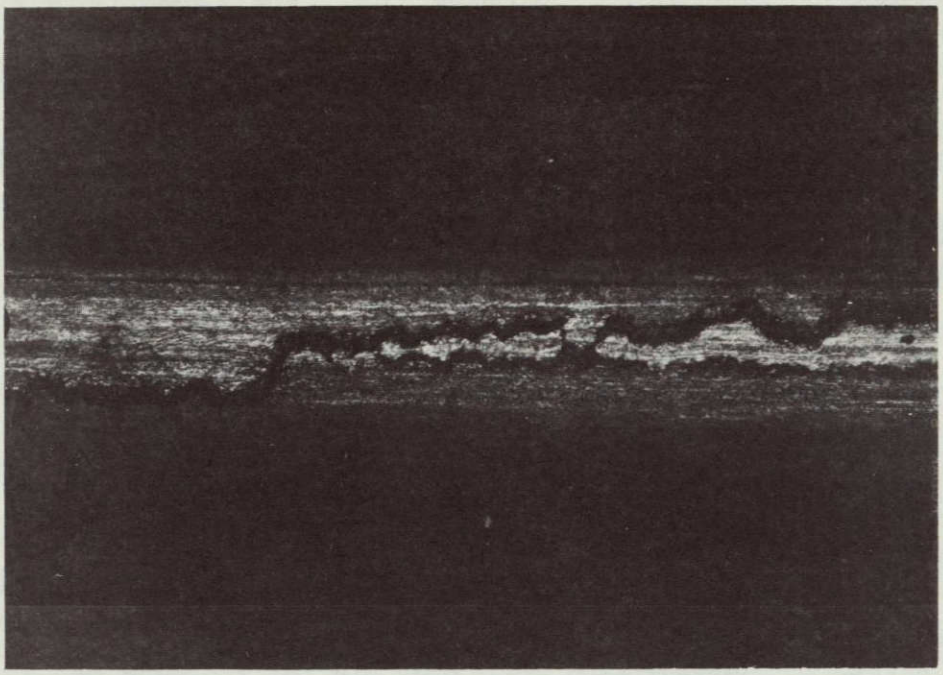

Figure 5.7 CRACK INITIATION IN A TYPE A SPECIMEN, MAGNIFICATION = 100X.

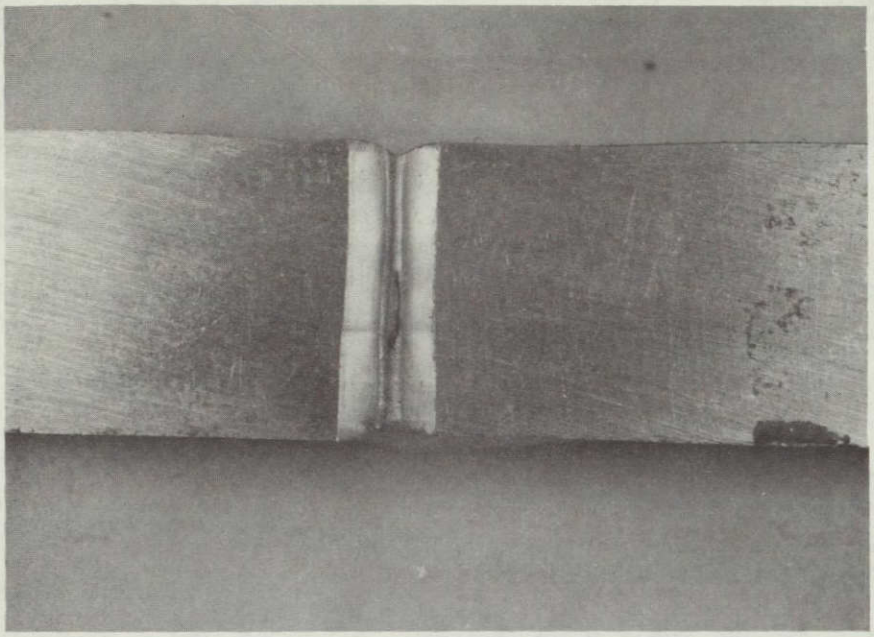

(a)

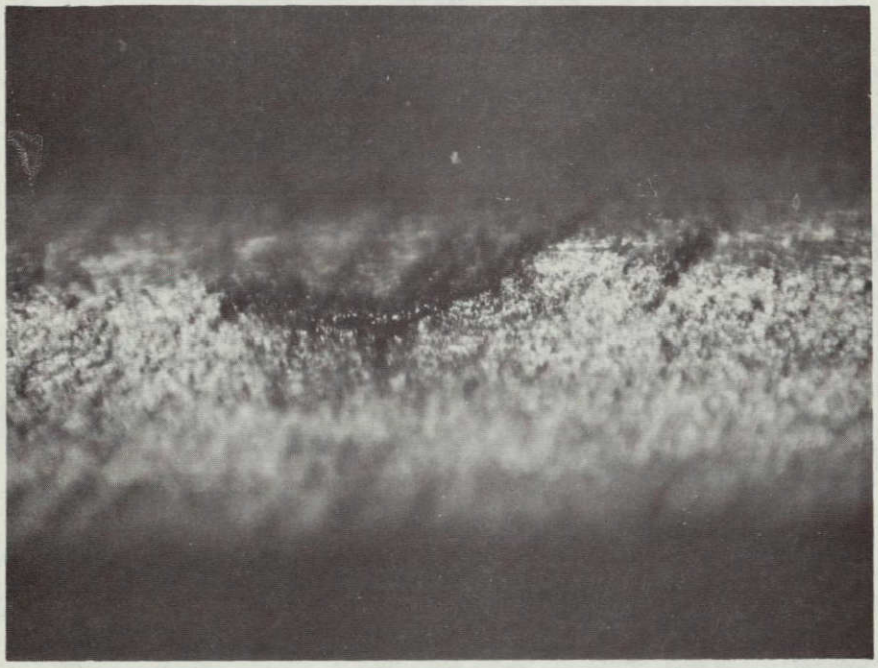

(b)

Figure 5.8 CRACK INITIATION IN A TYPE E SPECIMEN, (a) MAGNIFICATION = 4X, (b) MAGNIFICATION = 100X.

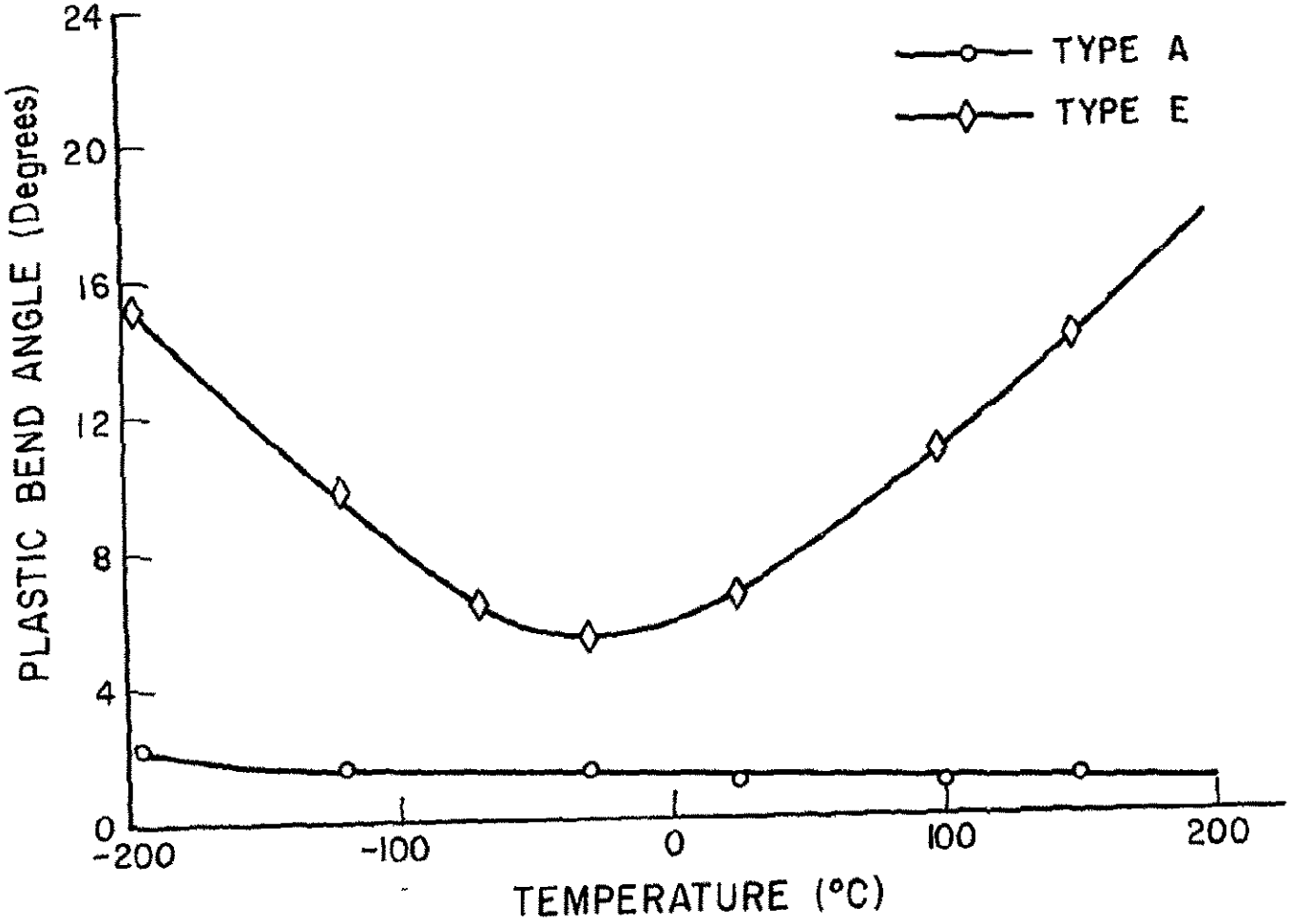

Figure 5 9 VARIATION OF THE BEND ANGLE REQUIRED FOR FRACTURE INITIATION WITH THE TEST TEMPERATURE

Knowing the relationship between ϵ_{yy} and θ_p (Fig 4.28), the root strain required for fracture initiation was obtained as a function of temperature and is shown in Fig 5 10 together with the failure strain of tensile samples The tensile failure strain of type E specimens in Fig 5 10 is expressed as per cent reduction in area and it is shown to be in agreement with the root strain required for crack initiation However, it is noted that the tensile ductility is higher than the root strains measured at fracture This will be discussed in Section (5 6-2). On the other hand, the per cent elongation on fracture of type A specimens is observed to be lower than the measured root strain for fracture initiation This discrepancy is believed to be due to experimental errors

Likewise, the variation of P_I with the temperature, represented in Fig 5 11 for both A and E type specimens, results from the variation of θ_I with temperature.

When a small crack initiates at the notch root in a type A specimen, the geometry of the notch is suddenly altered Cracks formed in this type of specimen tend to locally turn and run laterally Such lateral diversion would tend to blunt out the notch and at the same time would have a little effect in reducing the unnotched cross section of the specimen Because of the strain gradient existing below the notch, the material ahead of the crack will have a capacity for further deformation and the applied load will continue to rise Plastic flow in the matrix material below the stably advancing crack would effectively load the fibers, thus contributing to the increase in the applied load. When the net propagation of the crack in the transverse direction significantly reduces the unnotched cross section of the Charpy specimen, the applied load starts to drop and continues to do so in a stable manner

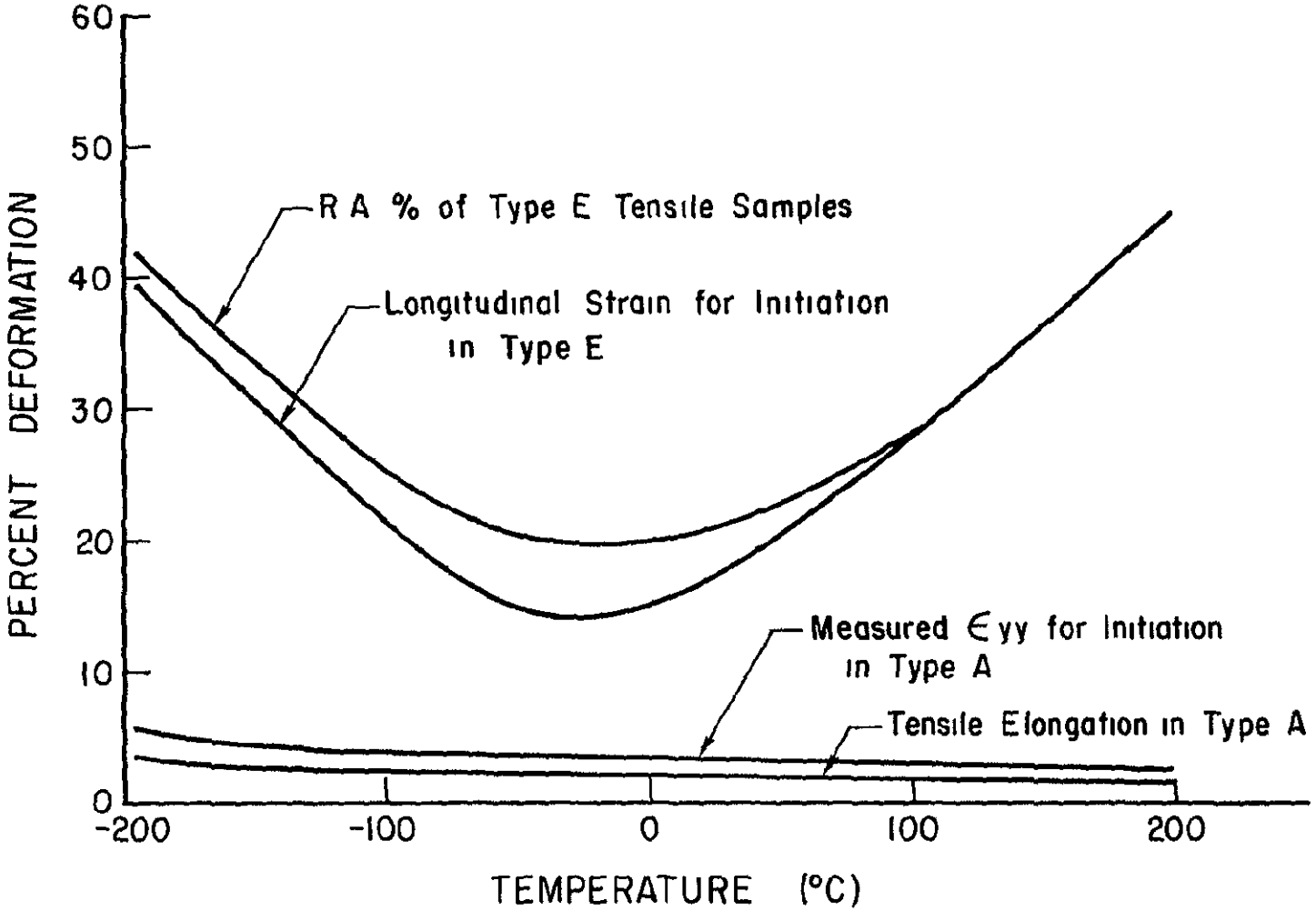

Figure 5 10 VARIATION OF THE STRAIN REQUIRED FOR FRACTURE INITIATION WITH TEMPERATURE

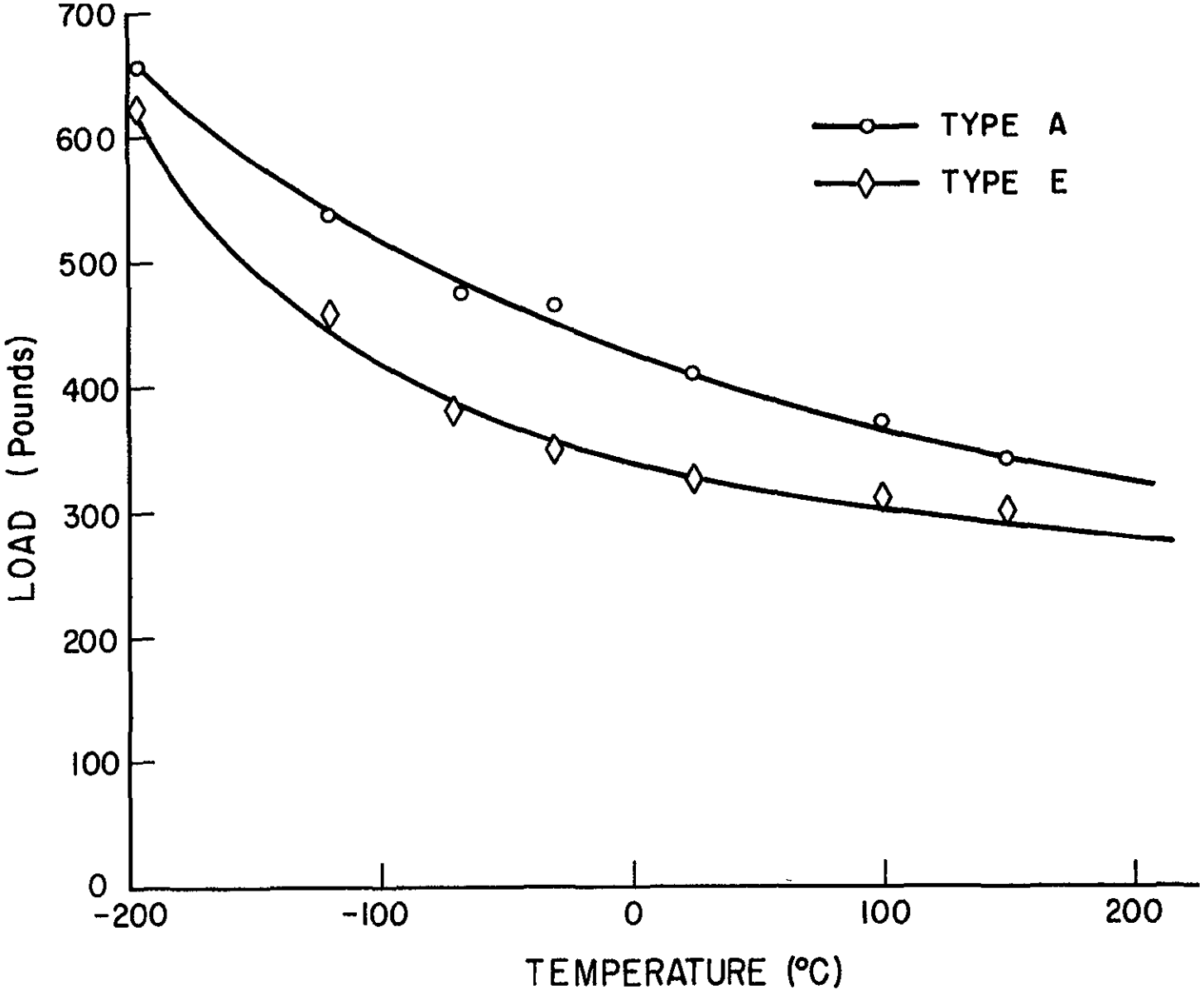

Figure 5.11 VARIATION OF THE LOAD REQUIRED FOR FRACTURE INITIATION WITH THE TEST TEMPERATURE

With the initiation of a small ductile tear at the notch root in a type E specimen, the stress distribution will become localized around the tip of the crack However ahead of the notch the strain has a steep gradient and the material which is inherently ductile in the y - direction will have a capacity for furthter straining before it starts to rupture Strain hardening in the material will cause the applied load to increase beyond P_I, the ultimate load is reached when the propagation of the crack has sufficiently reduced the unnotched cross section of the specimen The difference between the ultimate and initiation load decreases with the test temperature and at about 200°C and above, P_u and P_I will be equivalent The decrease in the difference between P_I and P_u with the test temperature may be due to a decrease in the strain hardening rate of the material

5 5 Criteria for Fracture Initiation

5 5-1 Fracture Initiation in Type A Specimens

An appropriate criterion for fracture initiation should be consistent with the experimental observations In type A specimens there are two observations which should be noted

(1) Cracks initiate at notch tip along the entire length of the leading edge of the notch

(2) The plastic bend angle required for fracture initiation θ_I varies with temperature in almost the same way as does the tensile failure strain θ_I and, therefore, the root strain would be higher at lower test temperature (Fig 5 10)

Consistent with these observations is a criterion for fracture initiation which is based on the attainment of a critical strain at the notch tip Fracture is thus initiated in the following way:

As deformation proceeds beyond P_{LY}, plastic flow in the matrix takes place resulting in effective load transfer to the fibers. Upon further deformation, fiber strain will gradually increase Since strain is maximum at the notch root, the fibers closest to the root will be the first to crack when the strain there reaches a value which is equal to their failure strain Fiber failure strain is of the order of 2→3%, therefore the transverse strain corresponding to such a small longitudinal strain will also be small. Thus the transverse stress will not build up to a sufficiently high value that could affect root strain in the vicinity of the notch and consequently root strain will not vary along the entire length of the leading edge of the notch As deformation proceeds, the fiber failure strain will be reached and fibers will crack all along the notch edge Further deformation will cause more fibers, below the notch tip, to crack The newly formed cracks join with the already existing ones at the root, leading to the formation of a macroscopic crack Fig 5 12 shows a crack developed at the notch root Ahead of the main crack, one of the fibers has a crack that has already grown into a pore which would eventually join the main crack.

5 5-2 Fracture Initiation in Type E Specimens

An appropriate criterion for fracture initiation in this type of specimen should be consistent with the following experimental observations

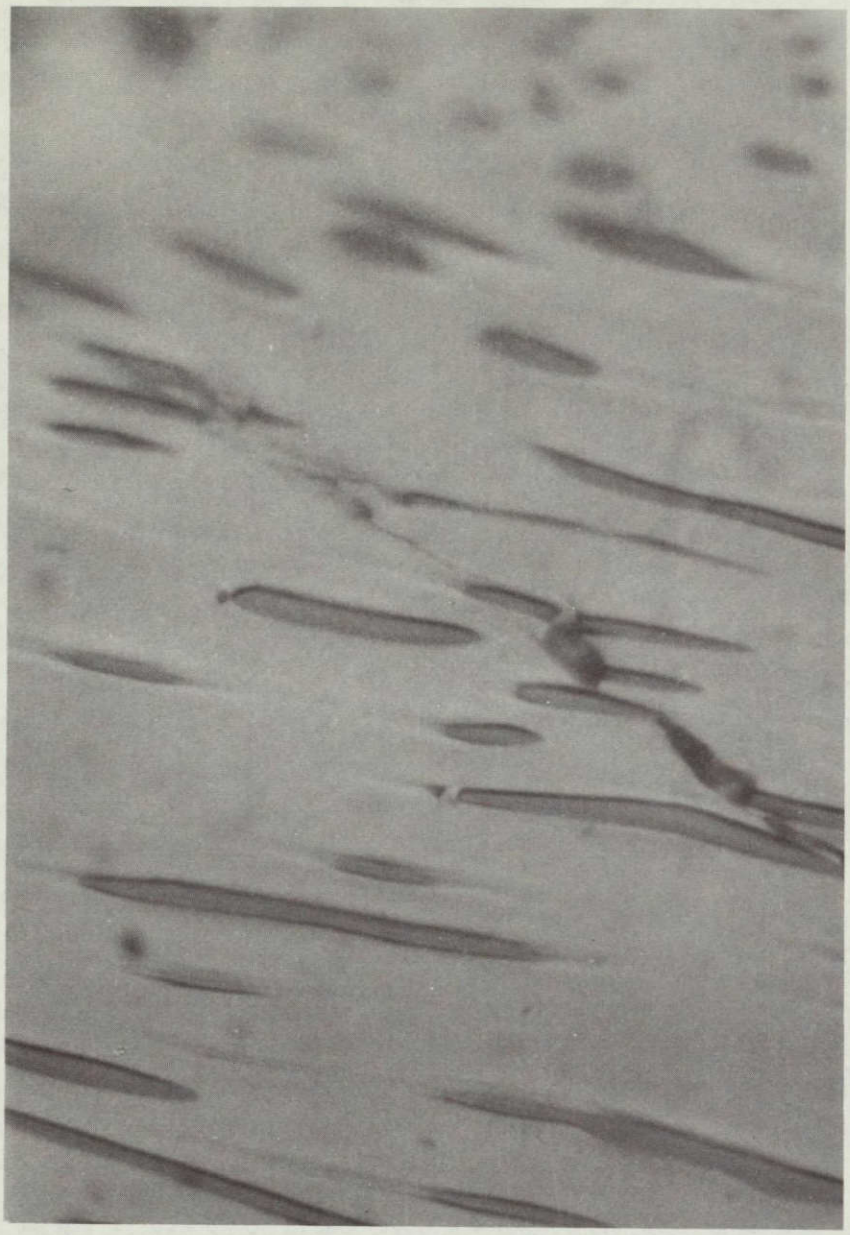

Figure 5.12 CRACK DEVELOPMENT IN A TYPE A SPECIMEN, MAGNIFICATION = 2500X.

(1) Cracks start to develop at the notch root in the longitudinal midsection of the Charpy specimen.

(2) The plastic bend angle required for fracture initiation varies with test temperature in almost the same manner as does the strain required for failure.

Consistent with these observations is a criterion for fracture initiation which is based on the attainment of a critical strain value at the notch root in the specimen midsection.

Transverse strain set up as deformation proceeds is considerable since the composite has the ability to undergo plastic deformation in a direction normal to the fibers. As a result, the transverse stress will build up reaching its maximum in the specimen midplane. This constraint set up will reduce the matrix ductility and cracks will start to develop at the notch root in the specimen midsection. Fig. 5.10 indicates that the root strain at the moment of failure initiation is less than the tensile ductility of the material. Salkind and George[36] noticed Al_3Ni fibers in replicas of the fracture surface of impact specimens. These Al_3Ni fibers were exposed either by decohesion at the fiber-matrix interface or by cleavage of the whiskers by the advancing crack. The failure of a type E specimen is essentially one of a ductile material.

5.5-3 Type F Specimens

The fibers prevent the matrix from undergoing considerable deformation in the z-direction. Therefore, even with large scale deformation in the longitudinal direction, the transverse strain in a type F specimen will be still very small. When a crack develops in this particular type of specimen, it starts at the notch root and along the entire length of the leading edge of the notch.

6

5.6 Energy of Crack Initiation

(a) Specimens with the Type A Fiber Orientation

As was shown previously, the bend angle at the moment of fracture initiation θ_I is larger at lower temperatures because the longitudinal strain ahead of the notch at the moment of crack initiation increases as the temperature decreases. The initiation energy is related to the area under the composite stress-strain curve and since both the strength and failure strain of the composite go up as the temperature decreases, the initiation energy would do likewise.

(b) Specimens with the Type E Fiber Orientation

At low temperatures both the strength and ductility of the material drop with the increase in temperature and so will the initiation energy. However, after the point of minimum (on the ductility-temperature curve) is reached (Figs. 3.5 and 3.22), the rate of decrease in the initiation energy would drop as a result of the increase in ductility with further increase in test temperature.

5.7 Crack Propagation

5.7-1 Notch Sensitivity

Notch sensitivity tests were performed on type A tensile specimens of the shape and dimensions shown in Fig. 2.5. A notch insensitive material is defined[7] as one which breaks when the stress on the net cross section (measured at the notch) attains a value equal to the breaking strength of the same material without a notch. The stress on the net cross section (measured at the notch) required to cause failure of specimens containing notches of varying depth was determined at 25°C and -196°C. The notch width was approximately 300μ, with a semicircular

root. Figure 5.13 indicates that the presence of a notch results in a decrease in the value of the stress (on the net cross section measured at the notch) required to achieve failure in the composite and that the effect is more pronounced at -196°C as compared to 25°C. This indicates that the material is less notch sensitive at higher temperatures, which is in agreement with the observation that crack diversion is more frequent at higher test temperatures (Fig. 5.3).

In type E specimens, a propagating crack is prevented from being diverted laterally by the presence of the fibers and the fracture surfaces will accordingly be quite flat. One would therefore expect that in this particular type of specimen the notch sensitivity of the material is temperature independent and that was shown to be the case (Fig. 5.14).

5.7-2 Energy of Propagation

(a) Type A Specimens

As a crack propagates through a composite, energy is extracted from the crack by plastic deformation in the material ahead of the crack tip. The work done per unit area at the crack tip during crack extension is[1]

$$2\gamma_p \simeq 2\sigma^*_{yy}\, V^*(c)$$

where σ^*_{yy} is the stress that exists in the volume element (ahead of the crack) when the crack advances. That is

$$\sigma^*_{yy} \cong \sigma_c$$

$$V^*(c) \simeq \rho\epsilon_c$$

where ρ is the root radius of the advancing crack.

Therefore

$$2\gamma_p \simeq 2\sigma_c \rho\epsilon_c \quad .$$

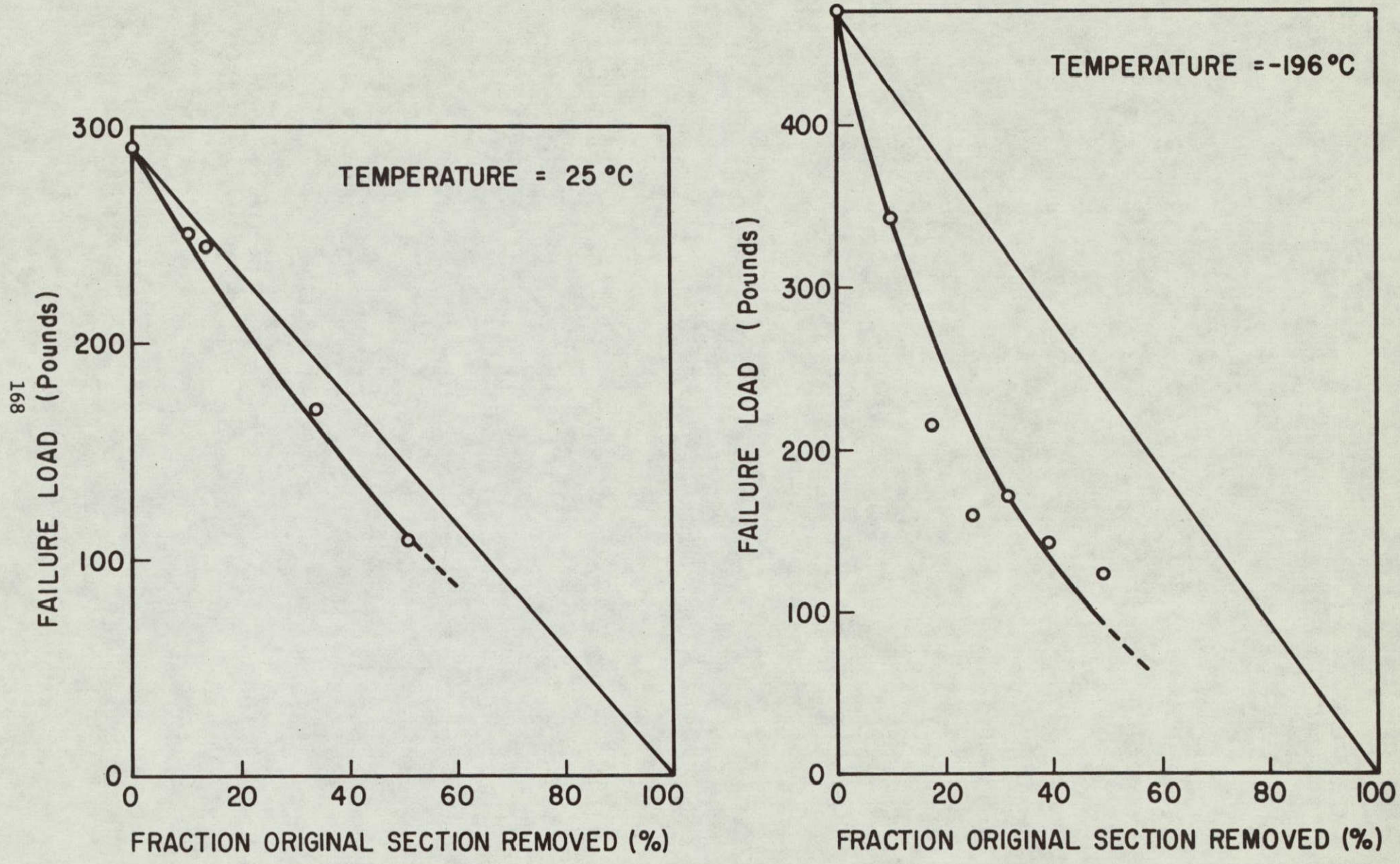

Figure 5.13a THE ULTIMATE LOAD OF TYPE A TENSILE SPECIMENS CONTAINING CRACKS OF VARYING LENGTH

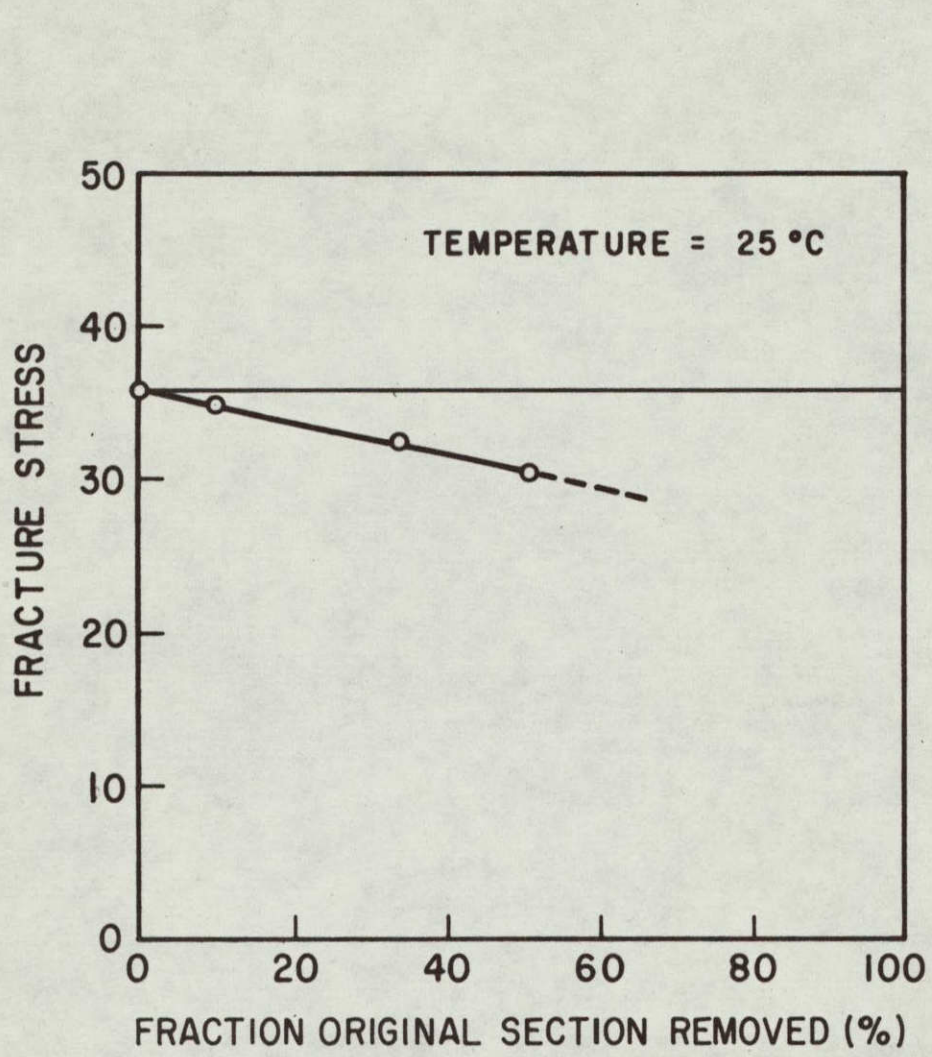

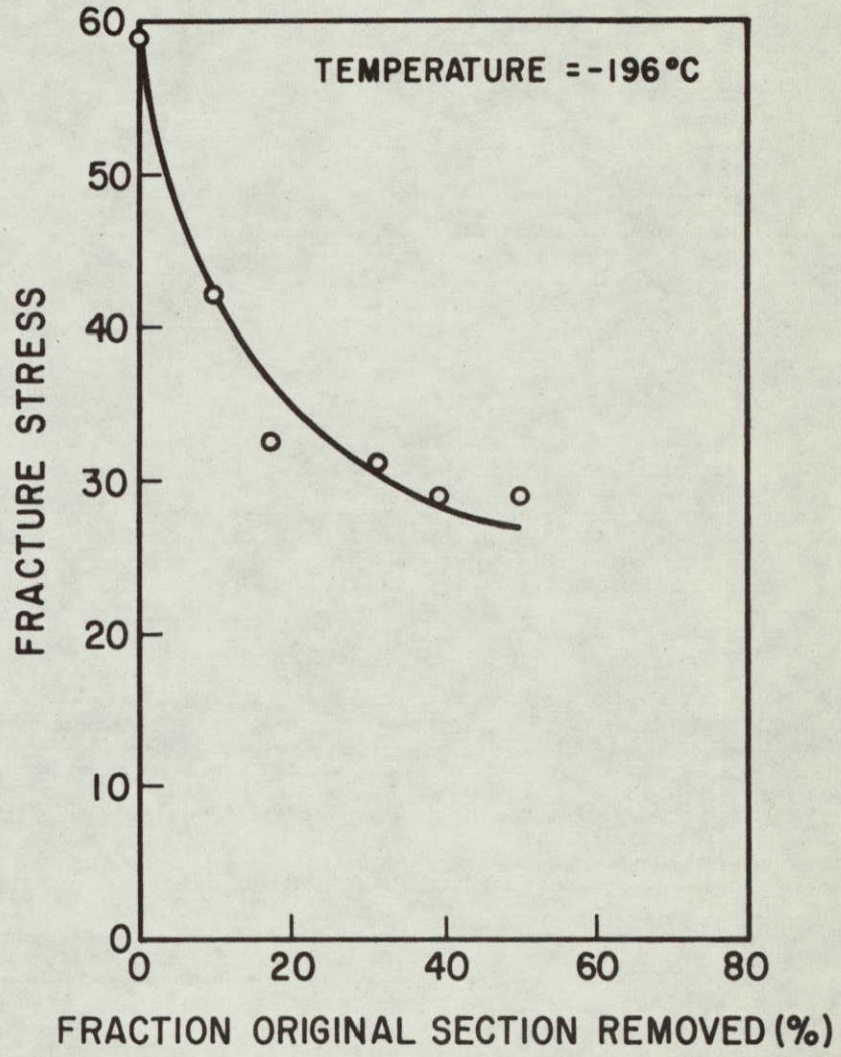

Figure 5.13b THE FRACTURE STRESS OF TYPE A TENSILE SPECIMENS CONTAINING CRACKS OF VARYING LENGTH

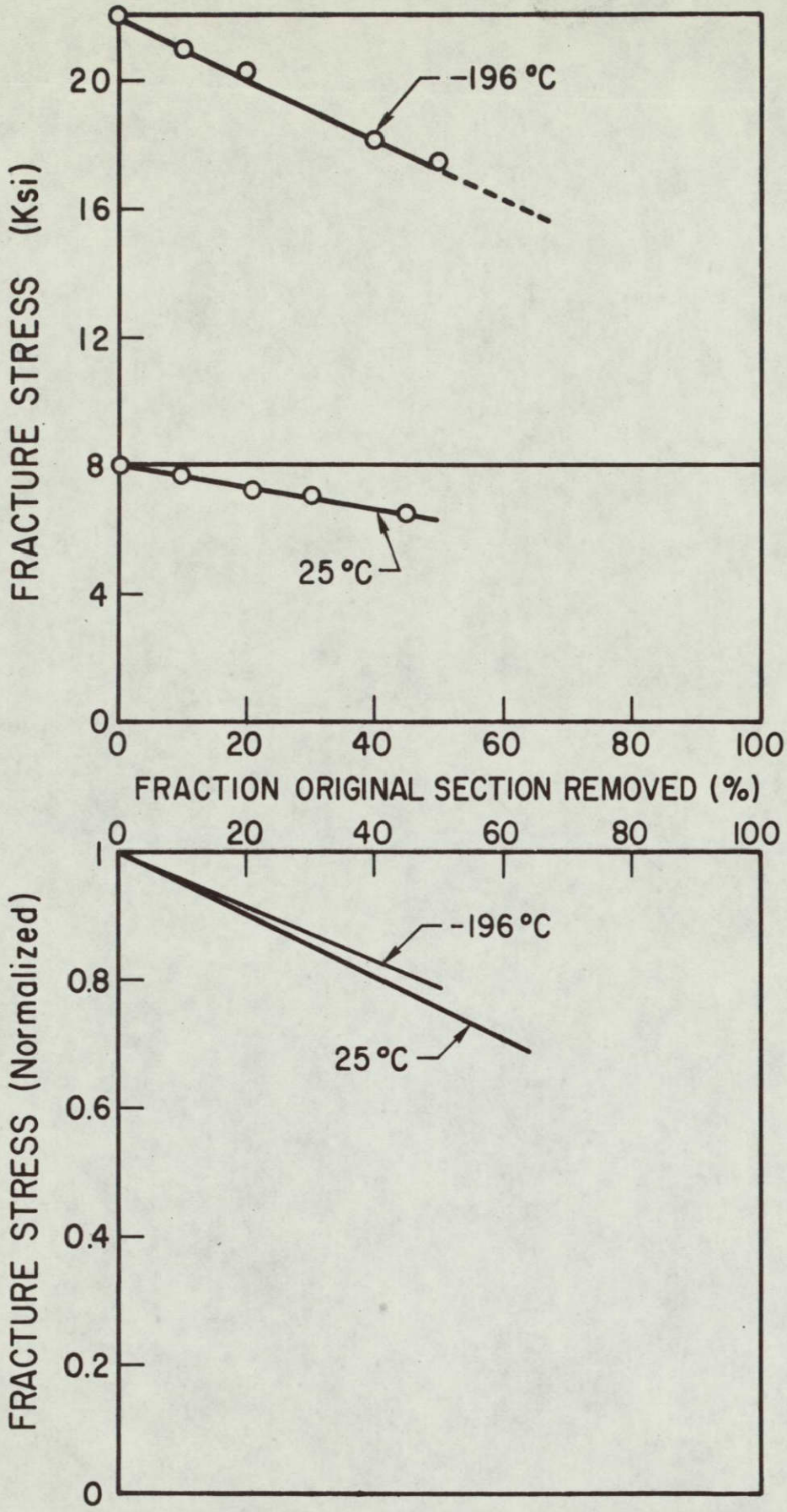

Figure 5.14 THE ULTIMATE STRESS OF TYPE E SPECIMENS CONTAINING CRACKS OF VARYING LENGTH

The notch sensitivity tests indicated that the material is less notch sensitive at higher temperatures which means that a propagating crack gets blunted more effectively at higher temperatures. The value of ρ is therefore expected to increase with increasing the test temperature and this tends to increase the energy of propagation.

Surface Energy. The mechanism of local diversion of the crack imparts a measure of toughness to the composite as it requires more energy to create the greater surface area.[8] Since the fracture surface becomes more irregular at higher temperatures, the contribution of the surface energy to the propagation energy term will be higher as the temperature increases.

The total effect of a temperature change on the energy of fracture may be summarized as follows:

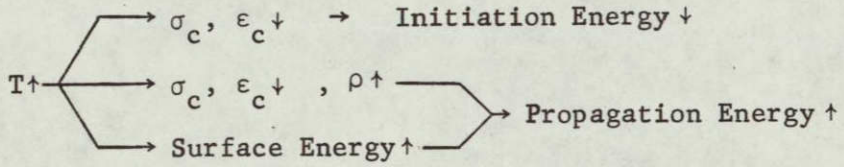

where ↑ indicates an increase in the particular variable or parameter, → means the word "produces," and ↓ stands for "decreases."

Salkind and George[36] reported no change in the impact energy of type A specimens (solidification rate = 2 cm/hour) tested at -196°C, 20°C, 200°C, and 400°C. Their impact results, which are shown in Fig. 5.15, would indicate that when the different fracture energy terms are added, their sum comes out to be independent of temperature.

(b) Type E Specimens

Since the notch sensitivity of type E specimens does not change with temperature and since their fracture surfaces were shown to be quite flat, the fracture energy of such specimens would be

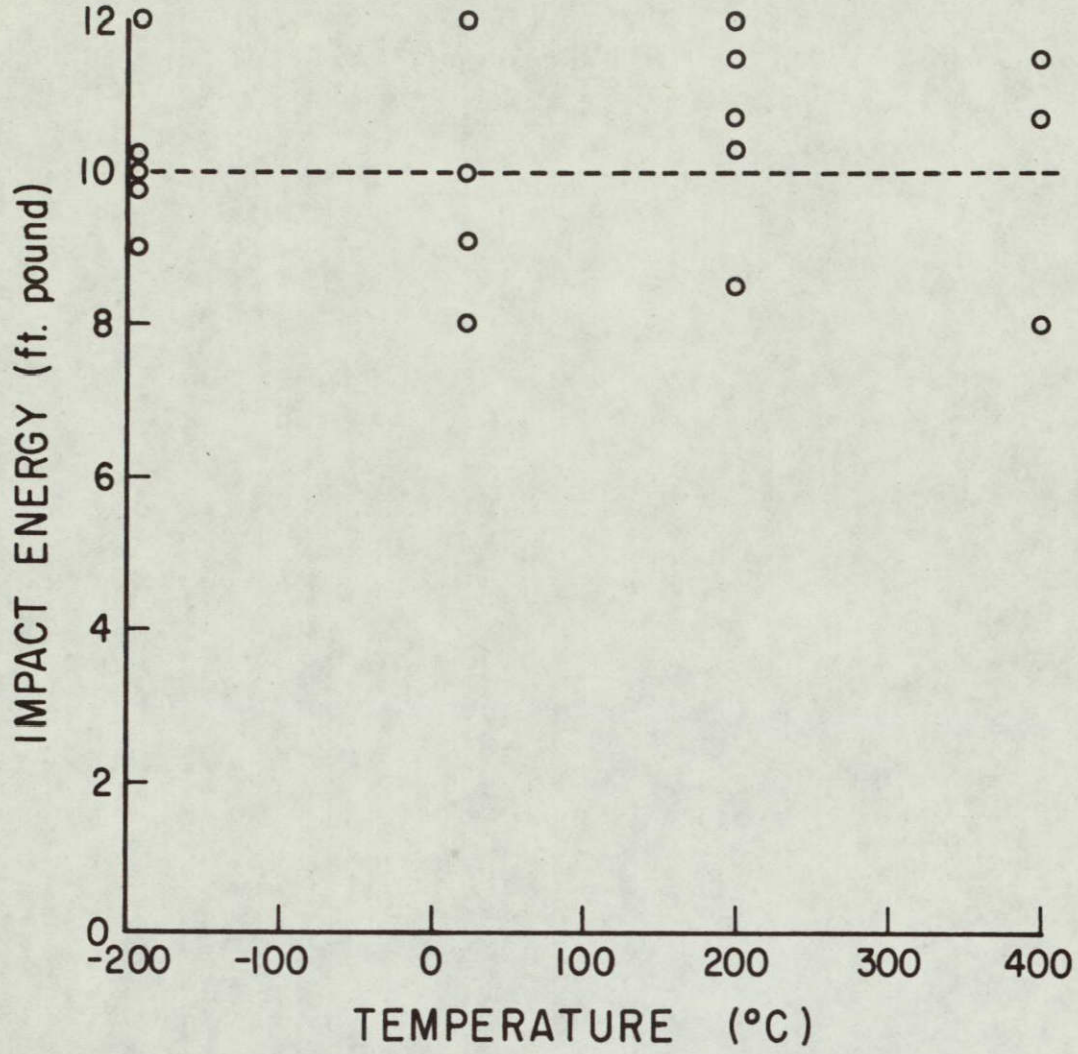

Figure 5.15 THE EFFECT OF TEMPERATURE ON THE IMPACT ENERGY VALUES OF TYPE A SPECIMENS (SALKIND AND GEORGE[36])

expected to change with temperature in a fashion similar to that of the initiation energy. Type E specimens exhibited partial fracture when impact loaded, and therefore the energy loss of the pendulum is not a reliable measure of impact energy. Type E specimens fractured at -196°C exhibited impact energy values in the neighborhood of 38 ft·lb as compared to an average of about 35 ft·lb[36] for specimens tested at room temperature (solidification rate = 2 cm/hour).

CHAPTER VI

SUMMARY AND CONCLUSIONS

1. The density of cracked fibers was shown to increase under increasing applied stress. However, the rate at which premature fiber cracking proceeds does not increase with the increase in applied stress. Premature fiber fracture does not, therefore, lead to instability, and the composite strength is determined primarily by the average fiber strength.
2. Linearizing the matrix stress-strain curve, the longitudinal strength of the composite was predicted from the properties of its individual constituents and was shown to be in good agreement with the experimentally measured values. The greater part of the change in the longitudinal strength is brought about by a similar change in fiber strength with temperature.
3. The transverse properties of the composite are primarily determined by those of the matrix. Tensile ductility of the composite, when loaded in the transverse direction, has been found to vary with temperature in a fasion similar to that of the matrix ductility.
4. The deformation pattern observed on the surface of type F deformed Charpy specimens is characterized by the formation of two hinges that extend from the corners of the notch and which broaden and penetrate deeper into the ligament as deformation proceeds. In type A specimens, the plastic zone was found to penetrate a little deeper into the specimen ligament and to extend laterally as deformation proceeds. The limited extension of the zone in the plane of the notch in type A specimens as compared to type F is ascribed to a higher value of σ_Y (stress required to initiate plastic flow in the matrix) in type A

specimens and to the fact that plastic flow in the matrix results in effective loading of the fibers.

5. The transverse strains ϵ_{zz}, determined for specimens with different fiber orientations, clearly demonstrated the anisotropic plastic behavior of the composite. It has been found that a linear relationship exists between the transverse and longitudinal strain. This relationship depends on the orientation of the fibers with respect to the specimen axis and notch leading edge and is expressed as follows:

$$\epsilon_{zz} = \alpha\epsilon_{yy}$$

where α has a value of 1/4 for both type A and E specimens and is equal to 1/40 for type F.

6. This inherent plastic anisotropy of the composite has been shown to have a considerable effect on fracture initiation. The location of the first crack to develop in the vicinity of the notch depends on the fiber orientation. In type A specimens, cracks were found to initiate at the notch tip along the entire length of the leading edge of the notch. On the other hand, cracks started to develop at the notch root in the longitudinal midsection of type E specimens.

7. The attainment of a critical strain at the notch tip was introduced as the criterion for crack initiation in type A specimens whereas in type E fracture initiates when a critical strain value is attained at the notch root in the specimen midsection.

8. Although the energy absorbed in initiating a crack in a type A specimen was found to increase as temperature decreased, the impact energy remained unchanged with the change in temperature. This was shown to be due to an increase in the propagation energy with the increase in test temperature.

REFERENCES

1. A. S. Tetelman and A. J. McEvily, Jr., Fracture of Structural Materials, Wiley, New York (1967).

2. W. R. Hibbard, Jr., ASM, Fiber Composite Materials (American Society for Metals, Metals Park, Ohio, 1965), Chapter I.

3. C. Herring and J. K. Galt, Phys. Rev., 85 (1952), 1060.

4. S. S. Brenner, ASM, Fiber Composite Materials (1965), Chapter II.

5. D. L. McDanels, R. W. Jech, and J. W. Weeton, Metal Progress, 78 (1960), 118.

6. R. W. Jech, E. P. Weber, and A. D. Schwope, Met. Soc. Conf., Vol. II, "Reactive Metals," Interscience Publishers, New York (1959), 109.

7. G. A. Cooper and A. Kelly, J. Mech. Phys. Solids, 15 (1967), 279.

8. J. Cook and J. E. Gordon, Proc. Roy. Soc., A282 (1964), 508.

9. D. Petrasek and J. Weeton, Trans. Met. Soc. AIME, 230 (1964), 977.

10. B. J. Bayles, J. A. Ford and M. J. Salkind, Trans. Met. Soc. AIME, 239 (1967).

11. M. J. Salkind, F. D. George, F. D. Lemkey and B. J. Bayles, "Investigation of the Creep, Fatigue, and Transverse Properties of Al_3Ni Whisker and $CuAl_2$ Platelet Reinforced Aluminum," United Aircraft Research Laboratories Final Report E910344-4 (May 11, 1966).

12. G. A. Chadwick, Progress in Materials Science, 12, 2 (1963).

13. G. A. Chadwick, J. Inst. Metals, 91 (1963), 169.

14. A. S. Yue, Trans. Met. Soc. AIME, 224 (1962), 1010.

15. W. A. Tiller and R. W. Mrdjenovich, J. Appl. Phys., 34 (1963), 3639.

16. M. J. Salkind and F. D. Lemkey, International Science and Technology, March 1967, 52.

17. M. J. Salkind, presented at UC Berkeley Course on Composite Materials, June 1968.

18. F. D. Lemkey and R. W. Kraft, Rev. Sci. Instr., 33, 8 (1962), 846.

19. R. W. Kraft, Trans. Met. Soc. AIME, 224 (1962), 65.

20. M. J. Salkind, F. D. George, W. K. Tice and B. J. Bayles, "Matrix Strengthening Mechanisms in Al_3Ni Whisker Reinforced Aluminum," United Aircraft Research Laboratories Report F910462-4 (June 12, 1967).

21. A. Kelly and G. J. Davies, Met. Rev., 10, 37 (1965), 1.

22. D. Cratchley, Met. Rev., 10, 37 (1965), 79.

23. ASM, Fiber Composite Materials (1965).

24. G. S. Holister and C. Thomas, Fibre Reinforced Materials, Elsevier (1966).

25. H. L. Cox, Brit. J. Appl. Phys., 3 (1952), 72.

26. N. F. Dow, "Study of Stresses near a Discontinuity in a Filament-Reinforced Composite Metal," General Electric Report R63SD61 (August, 1963).

27. D. M. Schuster and E. Scala, Trans. Met. Soc. AIME, 230 (1964), 1635.

28. D. M. Schuster, Ph.D. Thesis, Cornell (1967).

29. W. R. Tyson and G. J. Davies, Brit. J. Appl. Phys., 16 (1965), 199.

30. A. Kelly and W. R. Tyson, J. Mech. Phys. Solids, 13 (1965), 329.

31. B. Walter Rosen, AIAA Journal, 2, 11 (1964), 1985.

32. B. Walter Rosen, ASM, Fiber Composite Materials (1965), Chapter III.

33. W. Weibull, J. Appl. Mech., 18 (1951), 293.

34. A. S. Tetelman, "Fracture Processes in Fiber Composite Materials," presented at the ASTM National Conference on Composite Materials, New Orleans, February 1969.

35. G. A. Cooper and A. Kelly, "The Contribution to the Work of Fracture of a Composite Material of "Pull out" of Fibers," Dept. of Metallurgy, Cambridge.

36. M. J. Salkind and F. D. George, Trans. Met. Soc. AIME, July 1969.

37. M. Hansen, Constitution of Binary Alloys, Al-Ni System, 119, McGraw-Hill, New York (1958).

38. F. D. Lemkey, R. W. Hertzberg and J. A. Ford, Trans. Met. Soc. AIME, 233 (1965), 334.

39. P. Lacombe and L. Beaujard, J. Inst. Metals, 24 (1948), 1.

40. M. Lauriente and R. B. Pond, J. Appl. Phys., 27 (1956), 950.

41. D. J. Barber, Phil. Mag., 7, 8 (1962), 1925.

42. G. L. Montgomery and G. B. Craig, Trans. Met. Soc. AIME, 230 (1964), 1479.

43. W. Shockley, Dislocations and Mechanical Properties of Crystals, Discussion, 114, Wiley, New York (1956).

44. R. W. Hertzberg, F. D. Lemkey and J. A. Ford, Trans. Met. Soc. AIME, 233 (1965), 342.

45. D. L. McDanels, R. W. Jech and J. W. Weeton, Trans. Met. Soc. AIME, 233 (1965), 636.

46. H. L. Dunegan and C. A. Tatro, Techniques of Metals Research, 5 (1967).

47. H. Dunegan and D. Harris, "Acoustic Emission--a New Nondestructive Testing Tool," Lawrence Radiation Laboratory Report UCRL-70750 (January 16, 1968).

48. H. L. Dunegan, D. O. Harris and C. A. Tatro, Eng. Fract. Mech., 1 (1968), 105.

49. R. W. Hertzberg, ASM, Fiber Composite Materials (1965), Chapter IV.

50. M. J. Salkind, F. D. George, F. D. Lemkey, B. J. Bayles and J. A. Ford, Chemical Engineering Progress, 62, 3 (1966), 52.

51. H. Neuber, "Theory of Notched Stress; Principles for Exact Calculation of Strength with Reference to Structural Form and Material," AEC TR (1958), 45.

52. C. A. Rau, Jr. and A. S. Tetelman, International Fracture Conference, Brighton, England (1969).

53. C. A. Rau, Jr., Ph.D. Thesis, Stanford (1967).

54. V. Weiss, ASME, Paper No. 62-WA-270 (1962).

55. T. R. Wilshaw, C. A. Rau and A. S. Tetelman, Eng. Fract., 1 (1968), 191.

56. T. R. Wilshaw, Ph.D. Thesis, London (1965).

57. J. E. Srawley and W. F. Brown, "Fracture Toughness Testing," ASTM, Philadelphia, STP #381, 133.

58. A. P. Gross, unpublished work referenced by Srawley and Brown, in reference 57.

59. M. Creager and P. C. Paris, Inter. J. Fract. Mech., 3, 4 (1967), 247.

60. R. Hill, Mathematical Theory of Plasticity, Oxford (1950).

61. J. F. Knott, Ph.D. Thesis, Cambridge (1962).

62. T. R. Wilshaw, "The Deformation and Fracture of Mild Steel Charpy Specimens," Stanford University--DMS Report No. 66-6 (January, 1966).

63. A. S. Tetelman and T. R. Wilshaw, "A Criterion for Plasticity Induced Cleavage after General Yield in Notched Bend Specimens," Stanford University--DMS Report No. 69-T7 (October, 1968).

APPENDIX A

The parameters γ_1, δ_1, γ_2, δ_2, ϕ_2, ψ_2, γ_3 and δ_3 are defined as follows:

$$\gamma_1 = \frac{A_m (E_f - E_{m_1})}{A_f E_f + A_m E_{m_1}}$$

$$\delta_1 = \frac{A_f (E_f - E_{m_1})}{A_f E_f + A_m E_{m_1}}$$

$$\gamma_2 = \frac{A_m E_f}{A_f E_f + A_m E_{m_2}}$$

$$\delta_2 = \frac{A_m E_{m_2}}{A_f E_f + A_m E_{m_2}}$$

$$\phi_2 = \frac{A_f E_f}{A_f E_f + A_m E_{m_2}}$$

$$\psi_2 = \frac{A_f E_{m_2}}{A_f E_f + A_m E_{m_2}}$$

$$\gamma_3 = \frac{A_m E_f}{A_f E_f + A_m E_{m_3}}$$

$$\delta_3 = \frac{A_m E_{m_3}}{A_f E_f + A_m E_{m_3}} .$$

The arguments of the hyperbolic functions in equations (3.4-3.8) are >> 1 and therefore the functions can be replaced by the corresponding exponential functions. The solution of the five simultaneous equations will be

$$\sigma_c[\gamma_3\nu(\phi\mu - \psi\Delta) + (\mu - \nu)(\gamma_2\mu - \delta_2\Delta) + \Delta(\phi\mu - \psi\Delta)$$

$$- \delta_3(\mu - \nu)(\gamma_2\mu - \delta_2\Delta) - \delta_3\Delta(\phi\mu - \psi\Delta)] = \sigma_{fb}(\phi\mu - \psi\Delta)$$

where

$$\Delta = 1 + \gamma_1 [1 - e^{a_1(n - \ell)}].$$

μ and ν are given in Table 3.1.

n, m, $\sigma_f(n)$ and $\sigma_f(m)$ will be given by

$$n = \ell - \frac{1}{a_1} \ell n \frac{\delta_1}{\delta_1 + \mu - 1}$$

$$m = n - \frac{1}{a_2} \ell n \frac{(\mu - \nu)\sigma_c - \phi\mu\,\sigma_c + \psi\sigma_f(n)}{\psi\sigma_f(n) - \phi\mu\sigma_c}$$

$$\sigma_f(n) = \sigma_c\Delta$$

and

$$\sigma_f(m) = \sigma_f(n) + \frac{(\mu - \nu)[\gamma_2\mu\,\sigma_c - \delta_2\sigma_f(n)]\sigma_c}{\phi\mu\sigma_c - \psi\sigma_f(n)}$$

The shear stress distribution along the fiber-matrix interface at the moment of fiber failure is given by

$$\frac{1}{4}\lambda_1\delta_1\sigma_c e^{a_1(z-\ell)} \qquad n < z < \ell$$

$$\tau_j = \frac{1}{4}\lambda_2[\gamma_2\mu\sigma_c - \delta_2\sigma_f(n)]e^{a_2(z-n)} \qquad m < z < n$$

$$\frac{1}{4}\lambda_3[\gamma_3\nu\sigma_c - \delta_3\sigma_f(m)]e^{a_3(z-m)} \qquad 0 < z < m$$

$\tau_j(z)$ is shown in Fig. A-1.

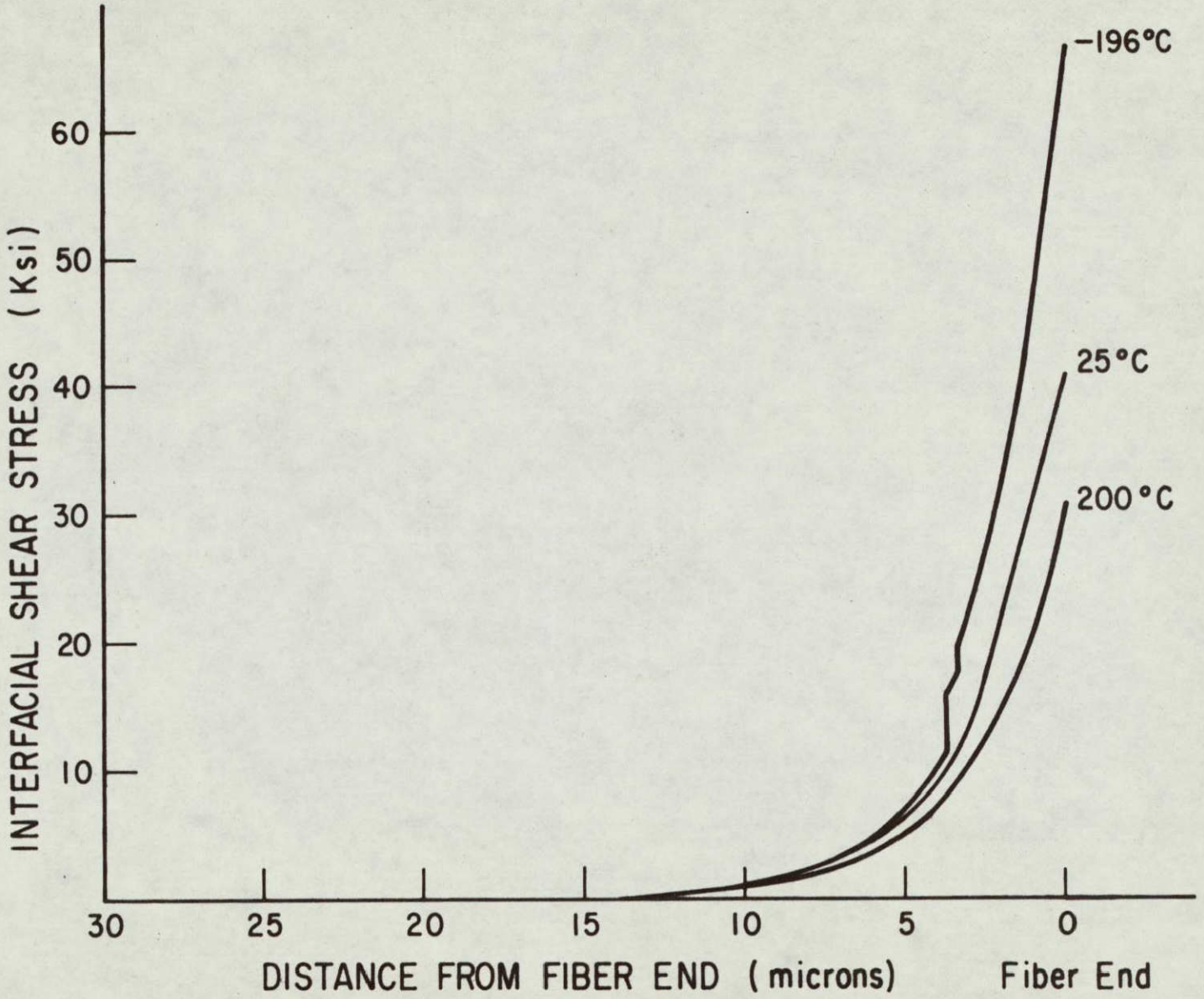

Figure A-1 SHEAR STRESS DISTRIBUTION ALONG THE FIBER-MATRIX INTERFACE AT THE MOMENT OF FIBER FAILURE